ABSTRACT

Title of dissertation: ENERGY EFFICIENCY OPTIMIZATION IN GREEN WIRELESS COMMUNICATIONS

Feng Han, Doctor of Philosophy, 2013

Dissertation directed by: Professor K. J. Ray Liu
Department of Electrical and Computer Engineering

The rising energy concern and the ubiquity of energy-consuming wireless applications have sparked a keen interest in the development and deployment of energy-efficient and eco-friendly wireless communication technology. Green Wireless Communications aims to find innovative solutions to improve energy efficiency, and to relieve/reduce the carbon footprint of wireless industry, while maintaining/improving performance metrics.

Looking back at the wireless communications of the past decades, the air-interface design and network deployment had mainly focused on the spectral efficiency, instead of energy efficiency. From the cellular network to the personal area network, no matter what size the wireless network is, the milestones along the evolutions of wireless networks had always been higher-and-higher data rates throughout these years. Most of these throughput-oriented optimizations lead to a full-power operation to support a higher throughput or spectral efficiency, which is typically not energy-efficient.

To qualify as green wireless communications, we believe that a candidate tech-

nology needs to be of high energy efficiency, reduced electromagnetic pollution, and low-complexity. In this dissertation research, towards the evolution of the green wireless communications, we have extended our efforts in two important aspects of the wireless communications system: air-interface and networking.

In the first aspect of this work, we study a promising green communications technology, the time reversal system, as a novel air-interface of the future green wireless communications. We propose a concept of time reversal division multiple access (TRDMA) as a novel wireless media access scheme for wireless broadband networks, and investigate its fundamental theoretical limits. Motivated by the great energy-harvesting potential of the TRDMA, we develop an asymmetric architecture for the TRDMA based multiuser networks. The unique asymmetric architecture shifts the most complexity to the BS in both downlink and uplink schemes, facilitating very low-cost terminal users in the networks. To further enhance the system performance, a 2D parallel interference cancellation scheme is presented to explore the inherent structure of the interference signals, and therefore efficiently improve the resulting SINR and system performance.

In the second aspect of this work, we explore the energy-saving potential of the cooperative networking for cellular systems. We propose a dynamic base-station switching strategy and incorporate the cooperative base-station operation to improve the energy-efficiency of the cellular networks without sacrificing the quality of service of the users. It is shown that significant energy saving potential can be achieved by the proposed scheme.

ENERGY EFFICIENCY OPTIMIZATION IN GREEN WIRELESS COMMUNICATIONS

by

Feng Han

Dissertation submitted to the Faculty of the Graduate School of the
University of Maryland, College Park in partial fulfillment
of the requirements for the degree of
Doctor of Philosophy
2013

Advisory Committee:
Professor K. J. Ray Liu, Chair/Advisor
Professor Min Wu
Professor Gang Qu
Dr. Zoltan Safar
Professor Lawrence C. Washington

Dedication

To my wife and parents.

Acknowledgments

I would like to express my deepest gratitude to my advisor, Professor K. J. Ray Liu, without whose guidance and support this dissertation would not have been possible. With his enthusiasm, vision, and dedication to students, Dr. Liu exemplifies to me what it means to be a great scholar, author, leader, teacher, and most importantly a wonderful mentor for my research, my career advancement and personal development. During my Ph.D. studies, his insightful guidance and unwavering support have always been inspiring me for conducting cutting-edge research and lead me through the difficult times. My four years with him has been the most rewarding and unforgettable experience.

I would like to thank other members in my dissertation committee. Special thanks are due to Dr. Zoltan Safar for his collaboration and enormous help and support that led to fruitful research results. I would also like to thank Professor Min Wu not only for serving on the committee but also for her continuous support with various recommendations and applications and her valuable advices on my career and life. I am also grateful to Professor Gang Qu and Professor Lawrence C. Washington for their precious time and effort serving on my committee.

I would like to thank all the members (and some former members whom I interacted with) in our Signals and Information Group for collaboration, friendship, encouragement, and help. Special thanks go to Dr. Beibei Wang, Dr. Yongle Wu, Mr. Yu-Han Yang, and Dr. Yan Chen for our inspiring research discussions, through which I learned a lot from them.

I would like to thank Professor André L. Tits, Professor Sennur Ulukus, Professor Nuno Martins, and other faculty members in University of Maryland. I learned a lot from their lectures and benefited even more from their kind help and wise advice. I also want to thank ECE staff Ms. Melanie Prange for her very kind help and advice regarding the departmental graduate study affairs.

Finally, I would like to thank my parents and my wife, for their unconditional love, and endless support. I dedicate this dissertation to them.

Table of Contents

List of Tables

List of Figures

Chapter 1: Introduction

1.1 Motivation

The wireless communications industry has experienced an explosive growth during the past few decades, and it continues to grow rapidly. The rising energy concern and the ubiquity of energy-consuming wireless applications has sparked a keen interest in the development and deployment of energy-efficient eco-friendly wireless communication technology. *Green Wireless Communications* aims to find innovative solutions to improve energy efficiency, and to relieve/reduce the energy consumption and carbon footprint of wireless industry, while maintaining/improving system performance and/or users' quality of service.

Looking back at the past decades, the system design and network deployment had mainly focused on the spectral efficiency, instead of energy efficiency. From the cellular network to the personal area network, no matter what size the wireless network is, the milestones along the evolutions of wireless networks had always been higher-and-higher data rates throughout these years. Most throughput-oriented optimizations lead to a full-power operation to support a higher throughput or spectral efficiency, which is typically not energy-efficient. With today's pervasive and vast-scale deployment, the energy consumed by wireless communications is no

longer as small as many people thought. Consuming about 60 billion kWh each year, the cellular communications networks alone are responsible for approximately 0.33% of global electricity consumption and 30 million tons of CO_2 emission per year, and keep growing by 16%-20% per year[1] [1]. Therefore, energy-efficient wireless communications technology is desirable more than ever before, and becomes an urgent challenge for the design of future wireless communications systems.

The evolution of green wireless communications calls for a paradigm shift of system design across all the layers. In this dissertation research, we extend our efforts in two important aspects of the wireless communications system: the air-interface[2] and the networking[3].

1.1.1 The Time Reversal Based Green Air Interface

In wireless communications, messages are delivered through information modulated radio-frequency (RF) waves, which propagates through a lossy environment and dissipate within certain distances. Therefore, one of the most straightforward efforts is to study how to efficiently deliver information from senders to receivers. The advancement in this endeavor reduces the energy consumed in the air and the unintended electromagnetic interference/pollution. One of today's most popular air interfaces is the Orthogonal Frequency-Division Multiplexing (OFDM), which has become the dominant air interface for a broad range of wireless communications

[1] which means that the energy consumption and CO_2 emission will be doubled in every 4-5 years

[2] In the OSI model, the air interface comprises layers 1 and 2 of the mobile communications system.

[3] In the OSI model, layer 3 is the network layer.

systems such as the 3GPP[4] Long Term Evolution (LTE) system, the IEEE802.16 WiMAX system, the IEEE 802.11a/g/n/ac (WiFi) wireless LAN system, and so on. One of the features that makes OFDM stands out is its high spectral efficiency, however, it is also well known for its high peak-to-average-power ratio (PAPR), which suffers from poor power efficiency.

In seeking of new green wireless air-interface technologies, our group discovered that the time reversal (TR) technique can be an ideal paradigm for green wireless communications, because of its inherent capability of efficiently harvesting signal energy from the surrounding environment [2]. Compared to the conventional direct transmission that uses Rake receivers, the TR transmission technique reveals significant transmission power reduction, achieves a high interference alleviation ratio, and exhibits a large multi-path diversity gain. Theoretical analysis shows a potential for *an order of magnitude improvement* in the above factors due to the temporal and spatial focusing effects [2, 3]. Real-life experimental measurements in a typical indoor environment also demonstrated that TR-based transmission can only cost as low as 20% of the transmission power needed in a direct transmission; further, the average interference can be alleviated by up to 6 dB even in the area that is just several wavelengths away from the focusing location [2]. Compared with the OFDM, the time reversal technique offers a promising single-carrier alternative air interface for the future high-speed broadband wireless communications with much improved energy efficiency.

Motivated by the great potential of time reversal, in this dissertation research,

[4]3GPP: 3rd Generation Partnership Project

we extend the basic time reversal structure to a multiuser system and propose a concept of time reversal division multiple access (TRDMA) as a novel wireless media access scheme for wireless broadband networks, and investigate its fundamental theoretical limits. Based on the concept of TRDMA, we develop an asymmetric architecture for the TRDMA based multiuser networks. The unique asymmetric architecture shifts the most complexity to the BS in both downlink and uplink schemes, facilitating very low-cost terminal users in the networks. To further enhance the system performance, a 2D parallel interference cancellation scheme is presented to explore the inherent structure of the interference signals, and therefore efficiently improve the resulting signal quality and system performance.

1.1.2 Energy-Aware Networking and Operations

In the second aspect of this dissertation research, we explore the energy-saving potential of the cooperative networking and dynamic operation of the cellular systems. This is motivated by the fact that most of today's large-scale wireless communications systems are still facilitated by the widely deployed infrastructures, which usually consume an order of magnitude more energy than the energy of RF signals actually consumed over the air. Among today's various wireless communications systems, the cellular network system is a leading contributor of energy consumption, due to its pervasive deployment and vast volume of users around the globe. In cellular networks, the base stations (BSs) contribute 60%-80% of the total energy consumption [4]. Therefore, improving the energy-efficiency of the BSs is the key of

achieving a more efficient wireless cellular network.

Until the few recent works [4–12], the deployment and network operation of BSs have mainly focused on optimizing capacity and data rates instead of energy consumption. The networking planning has been designed to accommodate the traffic load during the peak hours, which makes its energy-efficiency very low during the off-peak hours. On the one hand, this is because the energy consumption of a cellular base station is dominated by components simply keeping a BS active, which depends very little on the traffic load. As an example, a typical BS consumes 800-1500 W, while its power amplifier output is only 40-80 W during the high-traffic hours [5]. This means that a BS consumes more than 90% of its peak consumption even in periods of idle operation. On the other hand, the sinusoid-like BS traffic profile exhibits large peak-to-peak variations during a typical daily cycle [6]. Therefore, strategically turning off some of the base stations during the off-peak hours promises a great potential to improve the system's energy efficiency.

In this dissertation research, we propose a dynamic base-station switching strategy and incorporate the cooperative base-station operation to improve the energy-efficiency of the cellular networks without sacrificing the quality of service (QoS) of the users. Four progressive BS switch-off patterns are considered and dynamically switched according to the traffic load to maximize the energy saving. We study the QoS of the resulting cellular system in terms of the call-blocking probability and the channel outage probability, both analytically and numerically. We guarantee the channel outage probability by identifying the UEs situated at the worst-case locations and use BS cooperation to ensure their minimum QoS require-

ments. It is shown that significant energy saving potential can be achieved by the proposed scheme.

1.2 Organization of Dissertation

From the discussion above, green wireless communications is a new communications paradigm, which requires a new way of thinking and design philosophy in all layers of the communications system. This dissertation contributes to the lower three layers (Physical Layer, data-link Layer, and Network Layer), by developing a TRDMA based multi-user network as a green wireless air interface, and exploring the energy-saving potential of the cooperative networking of the cellular base stations. The rest of the dissertation is organized as follows.

1.2.1 An Overview of Related Works

In this chapter, we present an overview of the research history of time reversal and the related works in the energy-efficient base-station operation. We first review the basic concepts and principles of the time reversal technology, with an emphasis on its unique temporal and spatial focusing effects. The energy focusing effects of time reversal facilitate some unique features of TR-based communications systems and unparalleled energy-harvesting capability. Then, we introduce the problem of energy-efficient base-station operation, and summarize the related works.

1.2.2 The Concept of TRDMA and Its Fundamental Theoretical Limits

In this chapter, we propose the concept of TRDMA as a novel wireless media access scheme in rich-scattering environments, and developed a theoretical analysis framework for the proposed scheme. A number of system performance metrics are analyzed and evaluated, including the effective SINR at each user, achievable sum rate, and achievable rate with $\epsilon-$outage. We further investigate the achievable rate region for a simplified two-user case, from which one can see the advantages of TRDMA over its counterpart techniques, due to the spatial focusing effect of the time reversal. We incorporate and examine quantitatively the impact of spatial correlation of users to system performances for the SISO case to gain more comprehensive understanding of TRDMA.

1.2.3 TRDMA Based Multiuser Network-An Asymmetric Architecture

In this chapter, we first introduce a TRDMA uplink scheme and show its duality with the TRDMA downlink scheme presented in Chapter 3. The proposed TRDMA uplink and downlink schemes facilitate a unique asymmetric architecture of the TRDMA based multi-user network, in which the higher processing capability and channel knowledge available at the BS can be reused, resulting in a minimal complexity and cost at the terminals in both uplink and downlink. Such an

asymmetric complexity distribution is very desirable for many infrastructure-based wireless applications, which helps reduce the overall system cost and improve scalability. Another unique feature of the TRDMA system is that in essence the time reversal technique treats each path in the environment as a virtual antenna, which collectively contributes to the energy focusing capability and explores the spatial degrees of freedom. In the second half of this chapter, we investigate this feature by conducting a comparative study of the TRDMA system and massive multiple-input-multiple-output (MIMO) system.

1.2.4 2D Parallel Interference Cancellation Scheme for TRDMA

To further enhance the system performance, in this chapter, we propose a 2D parallel interference cancellation technique for the TRDMA uplink system. The proposed 2D parallel interference cancellation scheme utilizes the tentative decisions of detected symbols to effectively cancel both the ISI and IUI at the BS. To further improve the BER performance, a multi-stage processing can be performed by cascading multiple stages of the cancellation, with a total delay that increases linearly with the number of stages, but independently with the number of users. The BER performance of the single-stage cancellation is analyzed, and the approximated theoretical result is well consistent with simulation results. Simulations for up-to 3 stages of interference cancellation are provided and compared with the basic TRDMA system without interference cancellation.

1.2.5 Energy-Efficient Base-Station Cooperative Operation

In this chapter, we explore the energy-saving potential of the cooperative networking for cellular systems. We propose a dynamic base-station switching strategy and incorporate the cooperative base-station operation to improve the energy-efficiency of the cellular networks without sacrificing the quality of service of the users. We consider four progressive BS switch-off patterns and dynamically switch among them according to the traffic load to maximize energy saving. We study the quality of service (QoS) of the resulting cellular system in terms of the call-blocking probability and the channel outage probability, respectively. We derive and analyze the closed-form expressions for the QoS metrics based on the hexagonal cell model. We guarantee the channel outage probability by identifying the users situated at the worst-case locations and use BS cooperation to ensure their minimum QoS requirements. We evaluate the achievable energy saving performance of the proposed scheme and compare them with the conventional network operation.

Chapter 2: Background

2.1 A History of Time Reversal

2.1.1 The Basic Principles of Time Reversal

The time reversal (TR) signal processing is a technology to focus the power of signal waves in both time and space domains. The research of time reversal can date back to early 1970's, when phase conjugation was first observed and studied by Zel'dovich et al [13]. Unlike the phase conjugation that uses an holographic or parametric pumping [14], the time reversal uses transducers to record the signal waves and enables signal processing on the recorded waveforms.

The time reversal signal processing was applied by Fink et al. in 1989 [15], followed by a series of theoretical and experimental works [16–22] in acoustic communications. As found in acoustic physics [15–19] and then further validated in practical underwater propagation environments [20–22], the energy of the TR acoustic waves from transmitters could be refocused only at the intended location with very high spatial resolution. Since TR can make full use of multi-path propagation and also requires no complicated channel processing and equalization, it was later verified and tested in wireless radio communication systems in early 2000's,

especially in Ultra-wideband (UWB) systems [3, 23–26].

Until recent years, the applications of time reversal have been mainly considered as a specialty use for extreme multi-path environment. Therefore, not much development and interest could be seen beyond defense applications at that time. In fact, the principle of time reversal transmission is very simple, as demonstrated in Fig. 2.1. In Fig. 2.1, when transceiver A wants to transmit information to transceiver B, transceiver B first has to send an impulse-like pilot signal that propagates through a scattering and multi-path environment and the resulting waveforms are received and recorded by transceiver A. This is called channel probing phase. After that, transceiver A simply time-reverses (and conjugated, if the signal is complex valued) the received waveform and then transmits it back through the same channel to transceiver B. This is called TR-transmission phase.

There are two basic assumptions for the time reversal communication system to work:

- channel reciprocity: For certain wireless media, modeling the multi-path wireless channel as a linear system, the impulse responses of the forward link channel and the backward link channel are assumed to be identical.

- channel stationarity: The channel impulse responses are assumed to be stationary for at least one probing-and-transmitting cycle.

By utilizing channel reciprocity, the re-emitted TR waves can retrace the incoming paths, ending up with a constructive sum of signals of all the paths at the intended location and a "spiky" signal-power distribution over the space, as com-

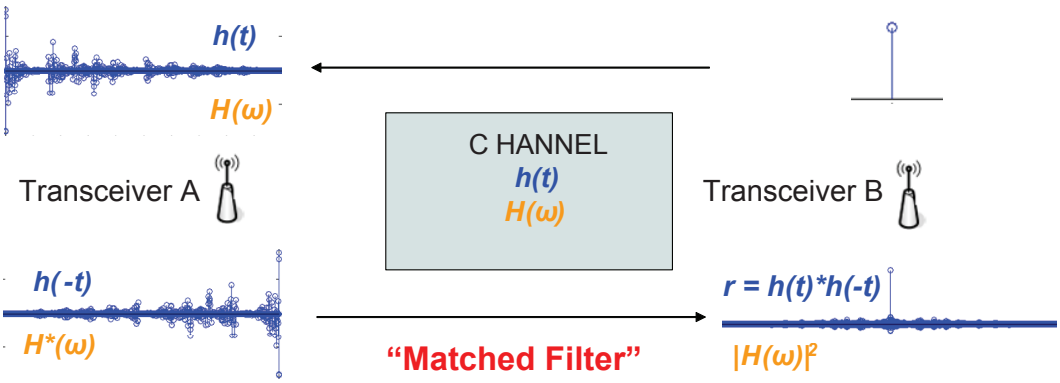

Figure 2.1: The time reversal signal processing principle

monly referred to as *spatial focusing effect*. Also from the signal processing point of view, in the point-to-point communications, TR essentially leverages the multi-path channel as a matched filter, i.e., treats the environment as a facilitating matched filter computing machine for the intended receiver, and focuses the wave in the time domain as well, as commonly referred as *temporal focusing effect*.

2.1.2 Temporal Focusing and Spatial Focusing of Time Reversal

In principle, the mechanisms of reflection, diffraction and scattering in wireless medium give rise to the uniqueness and independence of the channel impulse response of each multi-path communication link [27]. When the re-emitted TR waves from transceiver A propagate in the wireless medium, it is very likely that the location of transceiver B is the only location that is associated with the reciprocal channel impulse response. That is to say that given the re-emitted TR waveform from transceiver A that is specific to the channel impulse response between transceiver A and B, the environment will serve as a natural matched-filter

only for the intended transceiver B. As a result, the temporal focusing effect of the specific re-emitted TR waveform can be observed only at the location of transceiver B. It means that at the time instance of time focusing, the signal power not only exhibits a strong peak in the time domain at transceiver B, but also concentrates spatially only at the location of transceiver B in the rich multi-path environments.

Experimental results in both acoustic/ultrasound domain and radio frequency (RF) domain further verified the temporal focusing and spatial focusing effects of the time reversal transmission, as predicted by theory. Authors of [15–19] found that acoustic energy can be refocused on the source with very high resolution (wavelength level). In [20–22], acoustics experiments in the ocean were conducted to validate the focusing effects of time reversal in real underwater propagation environments. In the RF domain, experiments in [26, 28, 29] demonstrated the spatial and temporal focusing properties of electromagnetic signal transmission with time reversal by taking measurements in RF communications. Furthermore, a TR-based interference canceler to mitigate the effect of clutter was presented in [30], and target detection in a highly cluttered environment using TR was investigated in [31,32]. In [2], real-life RF experiment results were obtained in typical indoor environments, which shows the great potential of TR as a new paradigm of the Green wireless communications.

In the context of communication systems, the temporal focusing effect concentrates a large portion of the useful signal energy of each symbol within a short time interval, which effectively suppresses the inter-symbol interference (ISI) for high speed broadband communications. The spatial focusing effect allows the signal energy to be harvested at the intended location and reduces leakage to other

locations, leading to a reduced required transmit power consumption and lower co-channel interference to other locations. The benefits and unique advantages of time-reversal based communication systems due to the temporal and spatial focusing effects promise a great potential for wireless broadband communications, as will be discussed in this dissertation.

2.2 Energy-Efficient Base-Station Operation

The Information and Communications Technology (ICT) industry has experienced an explosive growth during the past few decades, and it continues to grow rapidly. Consuming roughly 900 billion KWh per year, the ICT infrastructure is responsible for about 10% of the world's electric energy consumption [1]. Within the ICT sector, the mobile telecommunication industry is one of the major contributors to energy consumption.

In addition to the environmental impact, electric energy consumption is also an important economic issue. Reports show that nearly half of the total operating expenses for a mobile telecommunication operator is the energy cost [33]. Therefore, an energy-efficient cellular network operation is needed more than ever before to reduce both the operational expenses and the carbon footprint of this industry.

In a typical cellular system, base stations (BSs) contribute 60%-80% of the energy consumption of the whole network [4]. Thus, improving the energy-efficiency of the BSs can significantly reduce both the operational cost and carbon footprint. However, the deployment and network operation of BSs have mainly focused on

optimizing capacity, coverage, and data rates, instead of energy consumption until recently [4–12]. One way to achieve this is to reduce the power consumption of an active BS by, for example, designing more efficient power amplifiers or decreasing the distance between the BS hardware and the antennas. However, these approaches have only a limited impact on the overall power-efficiency of the BS since its energy consumption is dominated by components that simply keep a BS active, which do not depend on the traffic load. As an example, a typical active BS consumes 800-1500 W, while its power amplifier output is only 40-80 W during the high-traffic hours [5]. This means that a BS consumes more than 90% of its peak consumption under the conventional operation even in periods of idle operation. On the other hand, as shown in [6], the sinusoid-like BS traffic profile exhibits large peak-to-peak variations during a typical daily cycle. Therefore, to achieve better energy efficiency, one can take a more efficient operation in which some BSs are turned off in the network in a coordinated manner, and the corresponding traffic load is distributed among the remaining active BSs when the overall network traffic load is low (e.g. during nights, weekends, and holidays).

After switching off some BSs, the service areas of the remaining active BSs increase, reducing the signal to noise ratio (SNR) at the receiver side considerably due to increased distances between the active BSs and the user equipments (UEs). For typical outdoor wireless environments, the path loss exponent can be between 3 and 4. This means that when the distance doubles, the required transmit power will increase at least eight-fold to maintain the same received SNR by simply increasing the transmit power (i.e. cell breathing [4]). As a result, the usability of simple

cell breathing is very limited due to the path-loss effect for the purpose of coverage extension to the cells with a switched-off BS. On the one hand, the power amplifier of each BS (as well as each UE) has a limited output capability, which limit the maximum range of coverage; on the other hand, even if one can assume that the PA is ideal, it is not energy-efficient to use cell breathing for extending the network service to a large distance.

Fortunately, the last decade witnessed a lot of progress in cooperative communications [34]. Cooperative communications has been proven to be able to effectively extend the network coverage with reduced total transmit power [35]. Specifically, in the context of switching off some BSs, not only does the BS cooperation reduce the required total transmit power (compared with the coverage extension using cell breathing), but also allows each of the cooperating BS to share just a fraction of the total transmit power, which eases the requirement of the PA. Since coverage issue has to be addressed when switching off some BSs (or putting them into Sleep), the cooperative communications serves as an enabling technology.

Among previous works on energy saving by BS operation management mechanisms, the authors of [7] proposed turning off half of the BSs in a regular pattern and analyzed the call blocking probability and the average number of active calls as functions of the call generation rate. In [4] and [6], the amount of saved energy was characterized for different temporal traffic patterns and switching strategies. A centralized and a decentralized BS switching algorithm in [8] assigned "active" or "sleep" states to BSs and users to "active" BSs based on the transmission rate requirements of the users and the capacity of the BSs. To lower the energy con-

sumption, a hierarchical cellular architecture was proposed in [9], where additional microcells provided increased capacity during peak hours, but these microcells were turned off during periods with low traffic demand, resulting in a more energy-efficient cellular system. Algorithms for the deployment and operation of such a hierarchical network were proposed in [10] based on the notion of area spectral efficiency. In [36], the cellular network greening effect was studied under four combinations of spatial-temporal power sharing policies, facilitated by short-term (per each time slot) BS transmit power control with global BS total power budget. The authors of [12] looked at the energy-saving potential and investigated the impacts of traffic intensity and BS density to the energy saving performance within the context of the LTE-Advanced cellular standard with coordinated multi-point (CoMP) transmission and wireless relaying. The authors of [11] considered the scenario where two operators share the same BS during low traffic periods and analyzed the achievable energy savings.

However, most previous works did not consider the quality of service (QoS) degradation due to this path-loss effect [37–39]. In this work, we take into account both path-loss and fading of wireless channels, and guarantee the QoS of UEs while achieving energy saving.

Chapter 3: The Concept of Time Reversal Division Multiple Access

In the single-user case, the temporal and spatial focusing effects have been shown to greatly simplify the receiver [3, 23–26, 40, 41], and reduce power consumption and interference while maintaining the quality of service (QoS) [2]. In this chapter, we consider a multi-user system over multi-path channels, and propose a concept of time-reversal division multiple access (TRDMA) as a wireless media access method by taking advantage of the high-resolution spatial focusing effect of time-reversal structure.

In principle, the mechanisms of reflection, diffraction and scattering in wireless medium give rise to the uniqueness and independence of the multi-path propagation profile of each communication link [27], which are exploited to provide spatial selectivity in spatial division multiple access (SDMA) schemes. Compared with conventional antenna-array based beamforming SDMA schemes, time-reversal technique makes full use of a large number of multi-paths and in essence treats each path as a virtual antenna that naturally exists and is widely distributed in environments.

Therefore, with even just one single transmit antenna, time reversal can potentially achieve a very high diversity gain and high-resolution "pin-point" spatial focusing. The high-resolution spatial focusing effect maps the natural multi-path

propagation profile into a unique *location-specific signature* for each link, as an analogy to the artificial "orthogonal random code" in a code-division system. The proposed TRDMA scheme exploits the uniqueness and independence of location-specific signatures in multi-path environment, providing a novel low-cost energy-efficient solution for SDMA. Better yet, the TRDMA scheme accomplishes much higher spatial-resolution focusing/selectivity and time-domain signal-energy compression at once, without requiring further equalization at the receiver as the antenna-array based beamforming does.

The potential and feasibility of applying time reversal to multi-user UWB communications were validated by some real-life antenna-and-propagation experiments in [2, 42–44], in which the signal transmit power reduction and inter-user interference alleviation as a result of spatial focusing effect were tested and justified for one simplified *one-shot* transmission over deterministic multi-path ultra-wideband channels. The idea of TRDMA proposed in this chapter was further supported by several important recent works [40, 41, 45]. [40] introduced a TR-based single-user spatial multiplexing scheme for SIMO UWB system, in which multiple data streams are transmitted through one transmit antenna and received by a multi-antenna receiver. Solid simulation results regarding bit-error-ratio (BER) demonstrate the feasibility of applying TR to spatially multiplex data streams. Following [40], [41] took into account the spatial correlation between antennas of the single receiver and numerically investigated through computer simulation its impact to BER performance. Based on [40] and [41], [45] tackled a multiuser UWB scenario with a focus on the impact of channel correlation to the BER performance through simulation.

However, there is not much theoretical characterization or proof about system performances found in any of these papers. Furthermore, most of these literatures focus only on BER performances, without looking at the spectral efficiency which is one of the main design purposes for any spatial multiplexing scheme. There is still a lack of system-level theoretical investigation and comprehensive performance analysis of a TR-based multi-user communications system in the literature. Motivated by the high-resolution spatial focusing potential of the time-reversal structure, existing experimental measurements and supporting literatures, several major developments have been proposed and considered in this chapter. Specifically:

- We propose the concept of TRDMA as a novel wireless media access scheme in rich-scattering environments, and developed a theoretical analysis framework for the proposed scheme.

- We consider a multi-user broadband communication system over multi-path *Rayleigh fading* channels, in which the signals of multiple users are separated solely by TRDMA.

- We define and evaluate a number of system performance metrics, including the effective SINR at each user, achievable sum rate, and achievable rate with $\epsilon-$outage.

- We further investigate the achievable rate region for a simplified two-user case, from which one can see the advantages of TRDMA over its counterpart techniques, due to TR's spatial focusing effect.

- We incorporate and examine quantitatively the impact of spatial correlation of users to system performances for the SISO case to gain more comprehensive understanding of TRDMA.

3.1 System Model

In this section, we introduce the channel and system model and the proposed TRDMA schemes. We begin with the assumptions and formulations of the channel model. Then, we describe the two phases of the basic TRDMA scheme with a single transmit antenna. Finally, we extend the basic single-input-single-output (SISO) scheme to an enhanced multiple-input-single-output (MISO) TRDMA scheme with multiple transmit antennas at the base station (BS).

3.1.1 Channel Model

In this chapter, we consider a multi-user downlink network over multi-path Rayleigh fading channels. We first look at a SISO case where the base station (BS) and all users are equipped with a single antenna. The channel response of the communication link between the BS and the i-th user is modeled as $\{h_i[k]\}$, for $k = 0, 1, 2, \cdots, L-1$. For each link, we assume that $h_i[k]$'s are independent circular symmetric complex Gaussian (CSCG) random variables with zero mean and variance

$$E[|h_i[k]|^2] = e^{-\frac{kT_S}{\sigma_T}}, \quad 0 \leqslant k \leqslant L-1 \tag{3.1}$$

where T_S is the sampling period of this system such that $1/T_S$ equals the system bandwidth B, and σ_T is the root mean square (rms) delay spread [46] of the channel. Due to the two-phase nature of TR structure, we assume that channels are reciprocal, ergodic and blockwise-constant with their tap values remaining fixed during at least one duty cycle. Each duty cycle consists of the recording phase and the transmission phase, which occupy the proportions of $(1-\eta)$ and η of the cycle period, with $\eta \in (0,1)$ depending on how fast channels vary over time.

We first assume that the channel responses associated with different users are uncorrelated. While realistic channel responses might not be perfectly uncorrelated, this assumption greatly simplifies the analysis while capturing the essential idea of TRDMA. Moreover, real-life experimental results in [2, 3] show that in a rich-scattering environment the correlation between channel responses associated with different locations decreases to a negligible level when two locations are even just several wave-lengths apart. A further discussion on the impact of the channel correlation between users to the system performance will be addressed in Section 3.4.

3.1.2 Phase 1: Recording Phase

The block diagram of a SISO TRDMA downlink system is shown in Fig. 4.2, in which there are N users receiving statistically independent messages

$$\{X_1(k), X_2(k), \cdots, X_N(k)\}$$

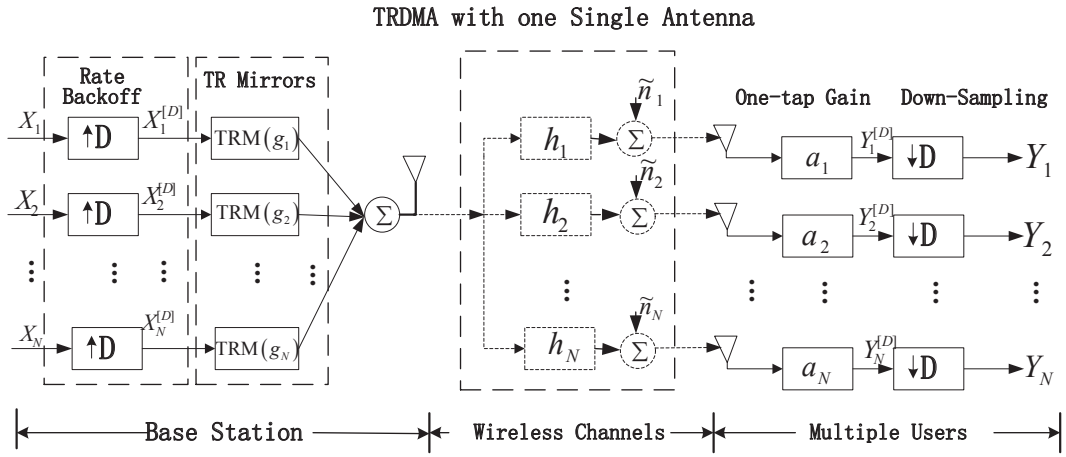

Figure 3.1: The diagram of SISO TRDMA multiuser downlink system

from the BS, respectively. The time-reversal mirror (TRM) shown in the diagram is a device that can record and time-reverse (and conjugate if complex-valued) the received waveform, which will be used to modulate the time-reversed waveform with input signal by convolving them together in the following transmission phase.

During the recoding phase, the N intended users first take turns to transmit an impulse signal to the BS (ideally it can be a Dirac $\delta-$function, but in practice a modified raise-cosine signal can be a good candidate for limited bandwidth for this purpose [2]). Meanwhile, the TRMs at the BS record the channel response of each link and store the time-reversed and conjugated version of each channel response for the transmission phase. For simplicity of analytical derivation, we assume in our analysis that the waveform recorded by TRM reflects the true CIR, ignoring the small corruption caused by thermal noise and quantization noise. Such a simplification was justified and based on the following facts shown in literatures of time reversal:

- The thermal noise (typically modeled as additive white Gaussian noise (AWGN)) can be effectively reduced to a desired level by averaging multiple recorded noisy samples of the same CIR's, provided that channels are slow-varying, as shown in the real-life experiments [2]. This would increase the portion $(1-\eta)$ of the recording phase in the entire duty cycle, leading to a increased channel probing overhead; but the structure of the analysis for the proposed system is not altered.

- The effect of quantization was studied by [47]. It was shown that a nine-bit quantization can be treated as nearly perfect for most applications; and even with one-bit quantization, the TR system can work reasonably well, demonstrating the robustness of the TR-based transmission technique.

3.1.3 Phase 2: Transmission Phase

After the channel recording phase, the system starts its transmission phase. At the BS, each of $\{X_1, X_2, \cdots, X_N\}$ represents a sequence of information symbols that are independent complex random variables with zero mean and variance of θ. In other words, we assume that for each i from 1 to N, $X_i[k]$ and $X_i[l]$ are independent when $k \neq l$. As we mentioned earlier, any two sequences of $\{X_1, X_2, \cdots, X_N\}$ are also independent in our model. We introduce the rate back-off factor D as the ratio of the sampling rate to the baud rate, by performing up-sampling and down-sampling with a factor D at the BS and receivers as shown in Fig. 3.1. Such a notion of back-off factor facilitates simple rate conversion in the analysis of a TR

system.

These sequences are first up-sampled by a factor of D at the BS, and the i-th up-sampled sequence can be expressed as

$$X_i^{[D]}[k] = \begin{cases} X_i[k/D], & \text{if } k \ mod \ D \ = \ 0, \\ 0, & \text{if } k \ mod \ D \ \neq \ 0. \end{cases} \tag{3.2}$$

Then the up-sampled sequences are fed into the bank of TRMs $\{g_1, g_2, \cdots, g_N\}$, where the output of the i-th TRM g_i is the convolution of the i-th up-sampled sequence $\left\{X_i^{[D]}[k]\right\}$ and the TR waveform $\{g_i[k]\}$ as shown in Fig. 3.1, with

$$g_i[k] = h_i^*[L-1-k] \Bigg/ \sqrt{E\left[\sum_{l=0}^{L-1} |h_i[l]|^2\right]}, \tag{3.3}$$

which is the normalized (by the average channel gain) complex conjugate of time-reversed $\{h_i[k]\}$. After that, all the outputs of TRM bank are added together, and then the combined signal $\{S[k]\}$ is transmitted into wireless channels with

$$S[k] = \sum_{i=1}^{N} \left(X_i^{[D]} * g_i\right)[k]. \tag{3.4}$$

In essence, by convolving the information symbol sequences with TR waveforms, TRM provides a mechanism of embedding the unique location-specific signature associated with each communication link into the transmitted signal for the intended user.

The signal received at user i is represented as follows

$$Y_i^{[D]}[k] = \sum_{j=1}^{N} \left(X_j^{[D]} * g_j * h_i\right)[k] + \tilde{n}_i[k], \tag{3.5}$$

which is the convolution of the transmitted signal $\{S[k]\}$ and the channel response

$\{h_i[k]\}$, plus an additive white Gaussian noise sequence $\{\tilde{n}_i[k]\}$ with zero mean and variance σ^2.

Thanks to the temporal focusing effect, the signal energy is concentrated in a single time sample. The i-th receiver (user i) simply performs a one-tap gain adjustment a_i to the received signal to recover the signal and then down-samples it with the same factor D, ending up with $Y_i[k]$ given as follows (for notational simplicity, $L-1$ is assumed to be a multiple of D)

$$Y_i[k] = a_i \sum_{j=1}^{N} \sum_{l=0}^{(2L-2)/D} (h_i * g_j)[Dl] X_j[k-l] + a_i n_i[k], \tag{3.6}$$

where

$$(h_i * g_j)[k] = \sum_{l=0}^{L-1} h_i[l] g_j[k-l] = \frac{\sum_{l=0}^{L-1} h_i[l] h_j^*[L-1-k+l]}{\sqrt{E\left[\sum_{l=0}^{L-1} |h_j[l]|^2\right]}} \tag{3.7}$$

with $k = 0, 1, \cdots, 2L-2$, and $n_i[k] = \tilde{n}_i[Dk]$, which is AWGN with zero mean and variance σ^2.

3.1.4 TRDMA with multiple transmit antennas

In this part, we generalize the basic TRDMA scheme into an enhanced version with multiple transmit antennas. To maintain low complexity at receivers, we consider a MISO case where the transmitting BS is equipped with M_T antennas together with multiple single-antenna users.

Let $h_i^{(m)}[k]$ denote the k-th tap of the channel response for the communication link between user i and the m-th antenna of the BS, and we assume it is a circular

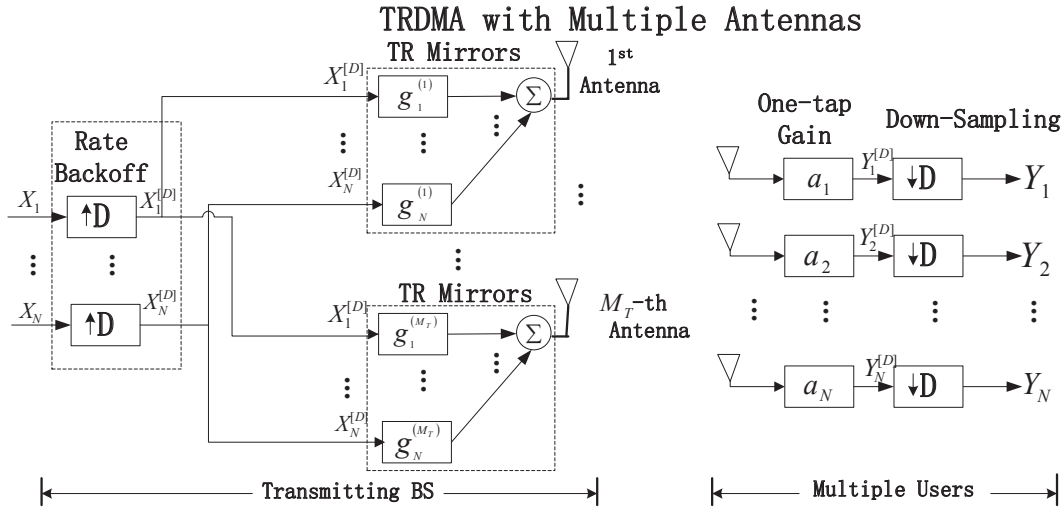

Figure 3.2: The diagram of MISO TRDMA multiuser downlink system

symmetric complex Gaussian random variable with zero mean and a variance

$$E[|h_i^{(m)}[k]|^2] = e^{-\frac{kT_S}{\sigma_T}}. \tag{3.8}$$

In alignment with the basic SISO case, we also assume that paths associated with different antennas are uncorrelated, i.e. $h_i^{(m)}[k]$ and $h_j^{(w)}[l]$ are uncorrelated for $\forall\ i,j \in \{1,2,\cdots,N\}$ and $\forall\ k,l \in \{0,1,\cdots,L-1\}$ when $m \neq w$, where $m,w \in \{1,2,\cdots,M_T\}$ are the indices of the m-th and w-th antennas at the BS.

For the MISO TRDMA scheme, each antenna at the BS plays a role similar to the single-antenna BS in the basic scheme. The block diagram for the MISO TRDMA is shown in Fig. 3.2. The TR waveform $\{g_i^{(m)}[k]\}$ is the normalized (by the average total energy of MISO channels) complex conjugate of time-reversed $\{h_i^{(m)}[k]\}$, i.e.

$$g_i^{(m)}[k] = h_i^{(m)*}[L-1-k] \Bigg/ \sqrt{E\left[M_T \sum_{l=0}^{L-1} |h_i^{(m)}[l]|^2\right]}. \tag{3.9}$$

As a result, the average total transmit power at the BS is

$$P = \frac{N \times \theta}{D}, \tag{3.10}$$

which does not depend on the number of the transmit antennas M_T.

The resulting received signal at user i can be similarly represented as

$$Y_i[k] = \sum_{j=1}^{N} \sum_{m=1}^{M_T} \sum_{l=0}^{\frac{2L-2}{D}} \left(h_i^{(m)} * g_j^{(m)} \right) [Dl] X_j[k-l] + n[k], \tag{3.11}$$

where $n[k]$ is additive white Gaussian noise with zero mean and variance σ^2.

Hereafter, we define a modified received signal-to-noise ratio (SNR) ρ for the

$$\rho = \frac{P}{\sigma^2} E \left[\sum_{l=0}^{L-1} |h_i^{(m)}[l]|^2 \right] = \frac{P}{\sigma^2} \frac{1 - e^{-\frac{LT_S}{\sigma_T}}}{1 - e^{-\frac{T_S}{\sigma_T}}}, \tag{3.12}$$

to rule out the potential multi-path gain in the system model in the following performance evaluations.

In the following sections, we evaluate the system performance of the proposed system in terms of the effective SINR, the achievable sum rate, and the achievable rates with $\epsilon-$outage.

3.2 Effective SINR

In this section, we evaluate the effective SINR of the proposed system. Since the basic SISO scheme is just a special case with $M_T = 1$, we analyze the general MISO case with M_T as a parameter in this section.

Note that for $\left\{ (h_i^{(m)} * g_j^{(m)})[k] \right\}$ in (3.11), when $k = L - 1$ and $j = i$, it corresponds to the maximum-power central peak of the autocorrelation function,

i.e.

$$(h_i^{(m)} * g_i^{(m)})[L-1] = \sum_{l=0}^{L-1} |h_i^{(m)}[l]|^2 \Big/ \sqrt{E\left[M_T \sum_{l=0}^{L-1} |h_i^{(m)}[l]|^2\right]}. \tag{3.13}$$

Subject to the constraint of one-tap receivers, the i-th receiver is designed to estimate $X_i[k - \frac{L-1}{D}]$ solely based on the observation of $Y_i[k]$. Then, the remaining components of Y_i can be further categorized into inter-symbol interference (ISI), inter-user interference (IUI) and noise, as shown below:

$$\begin{aligned} Y_i[k] = {} & a_i \sum_{m=1}^{M_T} (h_i^{(m)} * g_i^{(m)})[L-1] X_i[k - \frac{L-1}{D}] \quad (Signal) \\ & + a_i \sum_{\substack{l=0 \\ l \neq (L-1)/D}}^{(2L-2)/D} \sum_{m=1}^{M_T} (h_i^{(m)} * g_i^{(m)})[Dl] X_i[k-l] \quad (ISI) \\ & + a_i \sum_{\substack{j=1 \\ j \neq i}}^{N} \sum_{l=0}^{(2L-2)/D} \sum_{m=1}^{M_T} (h_i^{(m)} * g_j^{(m)})[Dl] X_j[k-l] \ (IUI) \\ & + a_i n_i[k]. \qquad (Noise) \end{aligned} \tag{3.14}$$

Note that the one-tap gain a_i does not affect the effective SINR, we consider it as $a_i = 1$ in the subsequent analysis, without loss of generality.

Given a specific realization of the random channel responses, from (3.14), one can calculate the signal power $P_{Sig}(i)$ as

$$\begin{aligned} P_{Sig}(i) &= E_X\left[\left|\sum_{m=1}^{M_T} (h_i * g_i)[L-1] X_i[k - \frac{L-1}{D}]\right|^2\right] \\ &= \theta \left|\sum_{m=1}^{M_T} \left(h_i^{(m)} * g_i^{(m)}\right)[L-1]\right|^2, \end{aligned} \tag{3.15}$$

where $E_X[\cdot]$ represents the expectation over X. Accordingly, the powers associated

with ISI and IUI can be derived as

$$P_{ISI}(i) = \theta \sum_{\substack{l=0 \\ l \neq \frac{L-1}{D}}}^{\frac{2L-2}{D}} \left| \sum_{m=1}^{M_T} \left(h_i^{(m)} * g_i^{(m)} \right) [Dl] \right|^2, \tag{3.16}$$

$$P_{IUI}(i) = \theta \sum_{\substack{j=1 \\ j \neq i}}^{N} \sum_{l=0}^{\frac{2L-2}{D}} \left| \sum_{m=1}^{M_T} \left(h_i^{(m)} * g_j^{(m)} \right) [Dl] \right|^2. \tag{3.17}$$

When there exists interference, the SINR is almost always a crucial performance metric used to measure the extent to which a signal is corrupted. It is especially the case for a media-access scheme, where interference management is one of the main design objectives. In this part, we investigate the *effective SINR* at each user in this multi-user network.

We define the average *effective SINR* at user i $SINR_{avg}(i)$ as the ratio of the average signal power to the average interference-and-noise power, i.e.,

$$SINR_{avg}(i) = \frac{E\left[P_{Sig}(i)\right]}{E\left[P_{ISI}(i)\right] + E\left[P_{IUI}(i)\right] + \sigma^2}, \tag{3.18}$$

where each term has been specified in (3.15), (3.16) and (3.17). Note that such defined *effective SINR* in (3.18) bears difference with the quantity $E\left[\frac{P_{Sig}(i)}{P_{ISI}(i)+P_{IUI}(i)+\sigma^2}\right]$ in general. The former can be treated as an approximation of the latter quantity. Such an approximation is especially useful when the calculation of the average SINR using multiple integration is too complex, as is the case in this chapter and literatures such as [26, 48, 49]. The performance of this approximation will be demonstrated in the numerical results shown in Figures 3.3, 3.4 and 3.5.

Theorem 1. *For the independent multi-path Rayleigh fading channels given in Section 3.1, the expected value of each term for the average effective SINR (3.18) at*

user i can be obtained as shown in (3.19), (3.20), and (3.21).

$$E\left[P_{Sig}(i)\right] = \theta\frac{1+e^{-\frac{LT_S}{\sigma_T}}}{1+e^{-\frac{T_S}{\sigma_T}}} + \theta M_T\frac{1-e^{-\frac{LT_S}{\sigma_T}}}{1-e^{-\frac{T_S}{\sigma_T}}}; \tag{3.19}$$

$$E\left[P_{ISI}(i)\right] = 2\theta\frac{e^{-\frac{T_S}{\sigma_T}}\left(1-e^{-\frac{(L-2+D)T_S}{\sigma_T}}\right)}{\left(1-e^{-\frac{DT_S}{\sigma_T}}\right)\left(1+e^{-\frac{T_S}{\sigma_T}}\right)}; \tag{3.20}$$

$$E\left[P_{IUI}(i)\right] = \theta(N-1)\frac{\left(1+e^{-\frac{DT_S}{\sigma_T}}\right)\left(1+e^{-\frac{2LT_S}{\sigma_T}}\right) - 2e^{-\frac{(L+1)T_S}{\sigma_T}}\left(1+e^{-\frac{(D-2)T_S}{\sigma_T}}\right)}{\left(1-e^{-\frac{DT_S}{\sigma_T}}\right)\left(1+e^{-\frac{T_S}{\sigma_T}}\right)\left(1-e^{-\frac{LT_S}{\sigma_T}}\right)}. \tag{3.21}$$

Proof. Based on the channel model presented in Section 3.1, the second and fourth moments of $h_i^{(m)}[k]$ are given by [50]

$$E\left[\left|h_i^{(m)}[k]\right|^2\right] = e^{-\frac{kT_S}{\sigma_T}}, \tag{3.22}$$

$$E\left[\left|h_i^{(m)}[k]\right|^4\right] = 2\left(E\left[\left|h_i^{(m)}[k]\right|^2\right)\right)^2 = 2e^{-\frac{2kT_S}{\sigma_T}}. \tag{3.23}$$

Based on (3.22) and (3.23), after some basic mathematical derivations, we obtain the following expected values for $\forall i \in \{1, 2, \cdots, N\}$ in (3.24), (3.25), and (3.26).

$$E\left[\left|\sum_{m=1}^{M_T}\left(h_i^{(m)} * g_i^{(m)}\right)[L-1]\right|^2\right] = \frac{1+e^{-\frac{LT_S}{\sigma_T}}}{1+e^{-\frac{T_S}{\sigma_T}}} + M_T\frac{1-e^{-\frac{LT_S}{\sigma_T}}}{1-e^{-\frac{T_S}{\sigma_T}}}; \tag{3.24}$$

$$E\left[\sum_{\substack{l=0\\ l\neq\frac{L-1}{D}}}^{\frac{2L-2}{D}}\left|\sum_{m=1}^{M_T}\left(h_i^{(m)} * g_i^{(m)}\right)[Dl]\right|^2\right] = 2\frac{e^{-\frac{T_S}{\sigma_T}}\left(1-e^{-\frac{(L-2+D)T_S}{\sigma_T}}\right)}{\left(1-e^{-\frac{DT_S}{\sigma_T}}\right)\left(1+e^{-\frac{T_S}{\sigma_T}}\right)}, \tag{3.25}$$

and

$$E\left[\sum_{\substack{j=1\\ j\neq i}}^{N}\sum_{l=0}^{\frac{2L-2}{D}}\left|\sum_{m=1}^{M_T}\left(h_j^{(m)} * g_i^{(m)}\right)[Dl]\right|^2\right] = (N-1) \tag{3.26}$$
$$\times\frac{1+e^{-\frac{DT_S}{\sigma_T}}+e^{-\frac{2LT_S}{\sigma_T}}-2e^{-\frac{(L+1)T_S}{\sigma_T}}-2e^{-\frac{(D+L-1)T_S}{\sigma_T}}+e^{-\frac{(D+2L)T_S}{\sigma_T}}}{\left(1-e^{-\frac{DT_S}{\sigma_T}}\right)\left(1+e^{-\frac{T_S}{\sigma_T}}\right)\left(1-e^{-\frac{LT_S}{\sigma_T}}\right)}.$$

Therefore, according to (3.15-3.17), (3.19-3.21) are obtained as shown in Theorem 1. □

From Theorem 1, one can see that the average interference powers (i.e. ISI and IUI) in (3.25) and (3.26) do not depend on M_T, while the signal power level in (3.24) increases linearly with the number of antennas, which is due to an enhanced focusing capability with multiple transmit antennas leveraging the multi-paths in the environment. The enhanced focusing effects monotonically improve the effective SINR. Another interesting observation is that a larger back-off factor D yields higher reception quality of each symbol, which is especially effective in the high SINR regime where interference power dominates the noise power. The asymptotic behavior of the SINR in the high SNR regime with varying D is given by the following theorem.

Theorem 2. *In the high SNR regime, when D is small such that $D \ll L$ and $D \ll \sigma_T/T_S$, doubling D leads to approximately a 3dB gain in the average effective SINR.*

Proof. First note that the signal power does not depend on D and that the noise is negligible in the high SINR regime. Thus, we can focus on the interference powers.

- **For Inter-Symbol Interference (ISI)**:

$$\frac{E\left[P_{ISI}(i, D=d)\right]}{E\left[P_{ISI}(i, D=2d)\right]} = \left(1 + e^{-\frac{dT_S}{\sigma_T}}\right) \frac{\left(1 - e^{-\frac{(L-2+d)T_S}{\sigma_T}}\right)}{\left(1 - e^{-\frac{(L-2+2d)T_S}{\sigma_T}}\right)} \tag{3.27}$$

Since $D \ll L$, then $\frac{\left(1-e^{-\frac{(L-2+d)T_S}{\sigma_T}}\right)}{\left(1-e^{-\frac{(L-2+2d)T_S}{\sigma_T}}\right)} \approx 1$; and since $D \ll \frac{\sigma_T}{T_S}$, then $e^{-\frac{dT_S}{\sigma_T}} \approx 1$.

Therefore,

$$\frac{E\left[P_{ISI}(i, D=d)\right]}{E\left[P_{ISI}(i, D=2d)\right]} \approx 2.$$

- **For Inter-User Interference (IUI)**:

$$\frac{E\left[P_{IUI}(i, D=d)\right]}{E\left[P_{IUI}(i, D=2d)\right]} = \left(1+e^{-\frac{dT_S}{\sigma_T}}\right) \times \frac{\left(1+e^{-\frac{dT_S}{\sigma_T}}\right)\left(1+e^{-\frac{2LT_S}{\sigma_T}}\right) - 2e^{-\frac{(L+1)T_S}{\sigma_T}}\left(1+e^{-\frac{(d-2)T_S}{\sigma_T}}\right)}{\left(1+e^{-\frac{2dT_S}{\sigma_T}}\right)\left(1+e^{-\frac{2LT_S}{\sigma_T}}\right) - 2e^{-\frac{(L+1)T_S}{\sigma_T}}\left(1+e^{-\frac{(2d-2)T_S}{\sigma_T}}\right)}. \tag{3.28}$$

For similar reasons,

$$\frac{E\left[P_{IUI}(i, D=d)\right]}{E\left[P_{IUI}(i, D=2d)\right]} \approx 2.$$

□

Next, we present some numerical evaluation of the average effective SINR. In this chapter, we mainly consider the broadband systems with frequency bandwidth that typically ranges from hundreds MHz to several GHz, which is much wider that those narrow-band systems specified in 3GPP/3GPP2. In the rich scattering environment, the underlying paths are so many that the number of perceived multiple paths increases quickly with the system bandwidth. For a system with bandwidth B, the minimum resolvable time-difference between two paths is $T_S = 1/B$ [51]. Keeping this in mind, we first choose $L = 257$ and $\sigma_T = 128T_S$ from a typical range, and evaluate the average effective SINR versus ρ under various system configurations in terms of N (the number of users), M_T (the number of antennas) and D (the rate back-off factor). In Fig. 3.3, Fig. 3.4 and Fig. 3.5, with $L = 257$ and $\sigma_T = 128T_S$, the solid curves are obtained according to the analytical results given

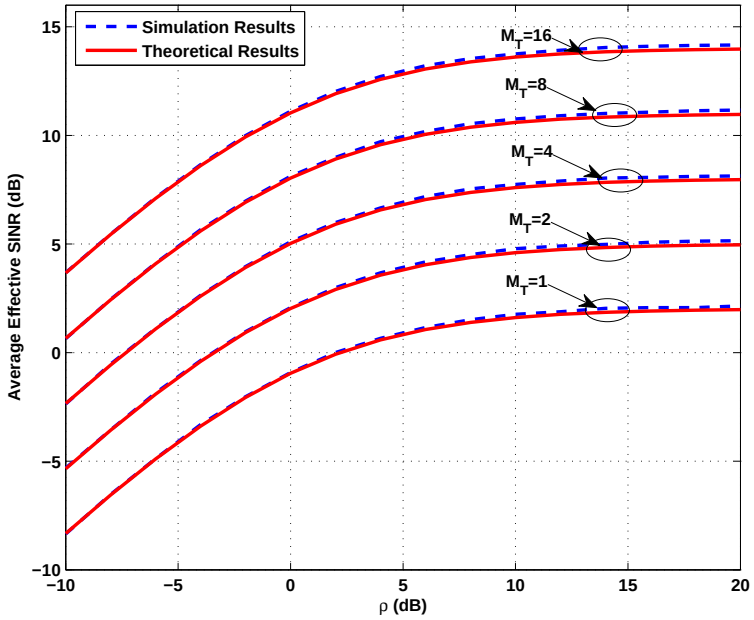

Figure 3.3: The impact of the number of antennas when $D = 8,\ N = 5$

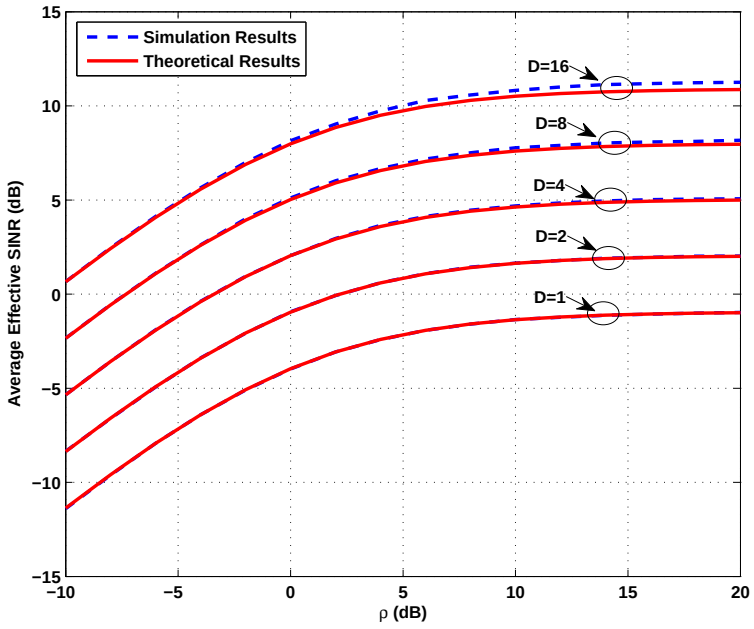

Figure 3.4: The impact of the rate back-off factor when $N = 5,\ M_T = 4$

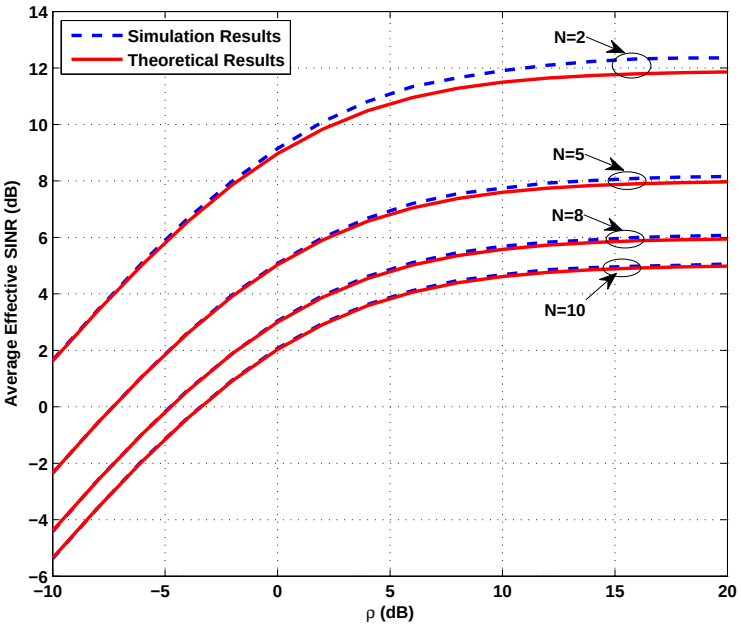

Figure 3.5: The impact of the number of users when $D = 8,\ M_T = 4$

by Theorem 1, and the dashed curves are collected from simulation which numerically computes $E\left[\frac{P_{Sig}(i)}{P_{ISI}(i)+P_{IUI}(i)+\sigma^2}\right]$. One can see that the results shown in Theorem 1 approximate well the empirical means obtained by simulation, which demonstrates the effectiveness of the definition of effective SINR in the system of interest in this chapter.

Fig. 3.3 is plotted with $D = 8$ and $N = 5$, demonstrating the impact of the number of antennas M_T to the effective SINR. From Fig. 3.3, one can see that approximately a 3dB gain is attained as M_T is doubled within a reasonable range. The impact of the rate back-off to the effective SINR is shown with $N = 5,\ M_T = 4$ in Fig. 3.4. Both analytical formulas and simulation results show that a lager D can reduce ISI and IUI while maintaining the signal power. In the high SNR regime

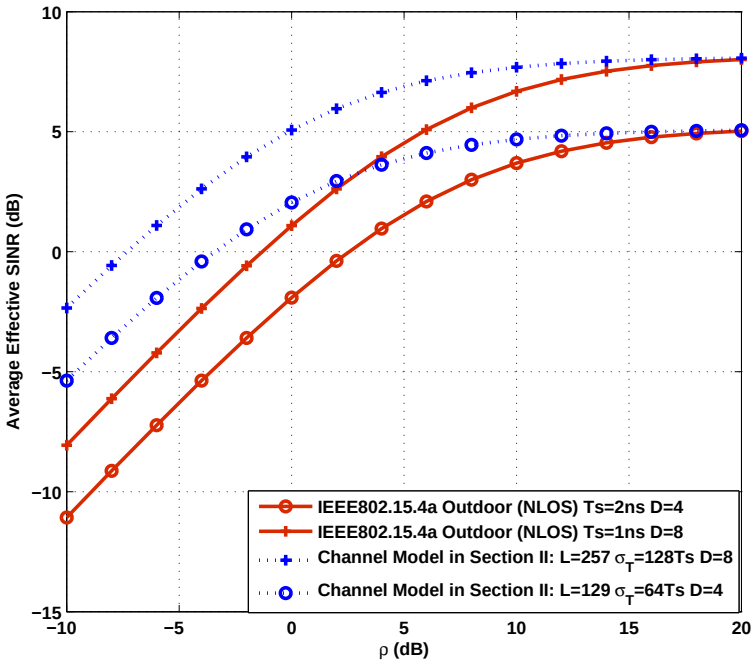

Figure 3.6: Average Effective SINR for IEEE 802.15.4a Outdoor NLOS Channel Models

where interference powers dominates the noise power, approximately a 3dB gain in effective SINR can be seen when D is doubled in Fig. 3.4, as predicted in Theorem 2. In Fig. 3.5, we investigate the impact of the number of users with $D = 8,\ M_T = 4$. Due to the existence of IUI, increasing the number of co-existing users will result in higher interference between users. That implies a tradeoff between the network capacity (in terms of number of serviced users) and signal reception quality at each user, as indicated in Fig. 3.5.

Furthermore, to demonstrate the usefulness and practical importance of TRD-MA, we apply the proposed scheme to more practical channel models, the IEEE 802.15.4a outdoor non-line-of-sight (NLOS) channels, operating over bandwidth of

$B = 500$ MHz ($T_S = 2$ ns and the typical channel length $L \sim 80$ to 150 taps) and $B = 1$ GHz ($T_S = 1$ ns and the typical channel length $L \sim 200$ to 300 taps) , respectively. Fig. 3.6 shows the performances of the proposed TRDMA scheme over the two aforementioned more practical channel models with $M_T = 4$. Such two practical channel models have comparable system bandwidth and channel lengths with the systems which TRDMA is designed for. From Fig. 3.6, one can see that the performances for the practical channel models well preserve the system performances obtained for our theoretical model, especially in high SNR regime. Note that in Fig. 3.6, we set $D = 4$ and 8 for the channels with $T_S = 2$ ns and $T_S = 1$ ns, respectively, to ensure that their baud rates (i.e. B/D) are the same for a fair comparison of the two. As seen from this comparison, a channel's multi-path richness (or higher resolution of perceiving multiple paths) due to the broader system bandwidth, gives rise to better user-separation in the proposed TRDMA scheme, which in essence increases the degree of freedom of the location-specific signatures.

3.3 Achievable Rates

In this section, we evaluate the proposed TRDMA in terms of achievable rates. We first look at its achievable sum rate. Then, two types of achievable rates with ϵ-outage are defined and analyzed. Finally, we derive the two-user achievable rate region of the TR structure and compare it with its rake-receiver counterparts.

3.3.1 Achievable sum rate

The achievable sum rate can be used as an important metric of the efficiency of a wireless downlink scheme, which measures the total amount of information that can be effectively delivered given the total transmit power constraint P.

When the total transmit power is P, the variance of each symbol is limited to $\theta = PD/N$, according to the simple conversion shown in (3.10). For any instantaneous realization of the random channels that we modeled in Section 3.1, one could obtain its corresponding instantaneous effective SINR of user i with symbol variance θ using the following equation

$$SINR(i,\theta) \triangleq \frac{P_{Sig}(i)}{P_{ISI}(i) + P_{IUI}(i) + \sigma^2}, \tag{3.29}$$

where each term is specified in (3.15), (3.16) and (3.17).

Then, under the total power constraint P, the instantaneous achievable rate of user i can be calculated as

$$\begin{aligned} R(i) &= \tfrac{\eta}{T_S \times B \times D} \log_2 \left(1 + SINR(i, PD/N)\right) \\ &= \tfrac{\eta}{D} \log_2 \left(1 + SINR(i, PD/N)\right) \quad (bps/Hz), \end{aligned} \tag{3.30}$$

where η serves as a discount factor that describe the proportion of the transmission phase in the entire duty cycle. We normalize the sum rate with bandwidth $B = 1/T_S$, presenting the information rate achieved per unit bandwidth (often referred to as *spectral efficiency*). It is also worth noting that in (3.30), the quantity is divided by D, because of the consequence of rate back-off.

Accordingly, the instantaneous achievable sum rate can be obtained as

$$R = \sum_{i=1}^{N} R(i) = \frac{\eta}{D} \sum_{i=1}^{N} \log_2 \left(1 + SINR(i, PD/N)\right). \tag{3.31}$$

Averaging (3.31) over all realizations of the random ergodic channels, the expected value of the instantaneous achievable sum rate is a good reference of the long-term performance and can be calculated by

$$R_{avg} = E\left[\frac{\eta}{D} \sum_{i=1}^{N} \log_2 \left(1 + SINR(i, PD/N)\right)\right]. \tag{3.32}$$

In the following part of this section, without loss of generality, we use $\eta \approx 1$, ignoring the overhead caused by the recording phase in each duty cycle, which is valid when the fading channels are not varying very fast.

The numerical evaluation of the average achievable sum rate is shown with the channel response length $L = 257$ and delay spread $\sigma_T = 128T_S$ in the system model. We plot this average achievable sum rate (setting $\eta = 1$) in Fig. 3.7 with different system configurations. To show how well the scheme performs in more realistic environments, we also include a comparison of the achievable-sum-rate performances for the channel model (with $L = 257$, $\sigma_T = 128T_S$, and $M_T = 4$) introduced in Section II and the IEEE802.15.4a Outdoor NLOS channel model (with $B = 1$ GHz, $T_S = 1$ ns, $M_T = 4$) in Fig. 3.8.

From Fig. 3.7, one can see that the sum rate increases monotonically with M_T, as a result of improved SINRs achieved by enhanced spatial focusing. From Fig. 3.8, one can see that the IEEE802.15.4a channel model with comparable channel length ($L \sim 200$ to 300 taps) well preserves the achievable sum rates of the theoretical channel model introduced in Section II, especially in high SNR regime. This

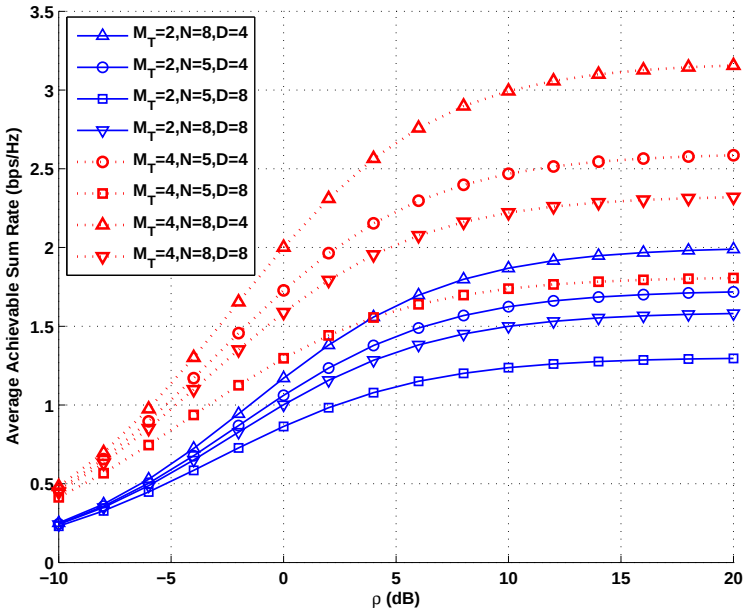

Figure 3.7: The normalized achievable sum rate versus ρ

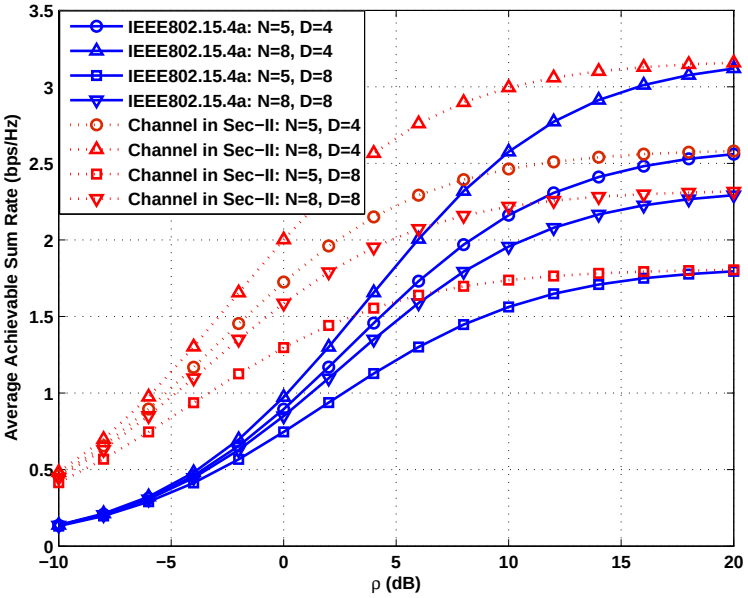

Figure 3.8: The normalized achievable sum rate for IEEE 802.15.4a Outdoor NLOS Channel Models

demonstrates the effectiveness of TRDMA when applied to more practical channels. From both Fig. 3.7 and Fig. 3.8, one can see that a larger N gives rise to a larger achievable sum rate, and a larger D discounts the achievable sum rate. The mechanisms of how D and N affect the sum rate are summarized as follows:

- A larger N increases the concurrent data streams (or multiplexing order), while degrades the individual achievable rate of each user due to stronger interference among users. The SINR degradation is inside the logarithm function in (3.31), but the multiplexing order multiplies logarithm function, yielding a higher sum rate when N is larger.

- On the other hand, a larger D improves the reception quality of each symbol as a result of reduced ISI, but it lowers the symbol rate of the transmitter. For similar reasons, the improvement of SINR inside the logarithm function cannot compensate the loss of lowering symbol rate.

Thus, a choice of the pair (D, N) can reveal a fundamental engineering tradeoff between the signal quality at each user and the sum rate of this network.

3.3.2 Achievable Rate with ϵ-outage

In this part, we look at the achievable rate with ϵ-outage of the TRDMA-based multi-user network. The concept of *ϵ-outage rate* [51,52] allows bits sent over random channels to be decoded with some probability of errors no larger than ϵ, namely the *outage probability*. Such a concept well applies to slow-varying channels, where the instantaneous achievable rate remains constant over a large number of

transmissions, as is typically the case when the TR-structure is applied.

We first define two types of outage events in the TRDMA-based downlink network, and then characterize the outage probability of each type.

Definition 1. (Outage of type I (individual rate outage)) *We say* outage of type I *occurs at user i if the achievable rate of user i, as a random variable, is less than a given transmission rate R, i.e. the outage event of type I can be formulated as* $\left\{\frac{1}{D}\log_2(1+SINR(i,\theta)) < R\right\}$, *and the corresponding outage probability of user i for rate R is*

$$P_{out\_I}(i) = Pr\left\{\frac{1}{D}\log_2(1+SINR(i,\theta)) < R\right\}, \tag{3.33}$$

where $SINR(i,\theta)$ is given by (3.29) with the variance of each information symbol $\theta = PD/N$.

Definition 2. (Outage of type II (average rate outage)) *We say* outage of type II *occurs if the rate achieved per user (averaged over all the users) in the network, as a random variable, is less than a given transmission rate R, i.e. the outage event of type II can be formulated as* $\left\{\frac{1}{N}\sum_{i=1}^{N}\frac{1}{D}\log_2\left(1+SINR(i,\theta)\right) < R\right\}$, *and the corresponding outage probability for rate R is*

$$P_{out\_II} = Pr\left\{\frac{1}{D\cdot N}\sum_{i=1}^{N}\log_2\left(1+SINR(i,\theta)\right) < R\right\}, \tag{3.34}$$

where $SINR(i,\theta)$ is given by (3.29) with the variance of each information symbol $\theta = PD/N$.

We present the two types of outage probabilities as functions of the transmission rate R in Fig. 3.9. Without loss of generality (due to symmetry), we select

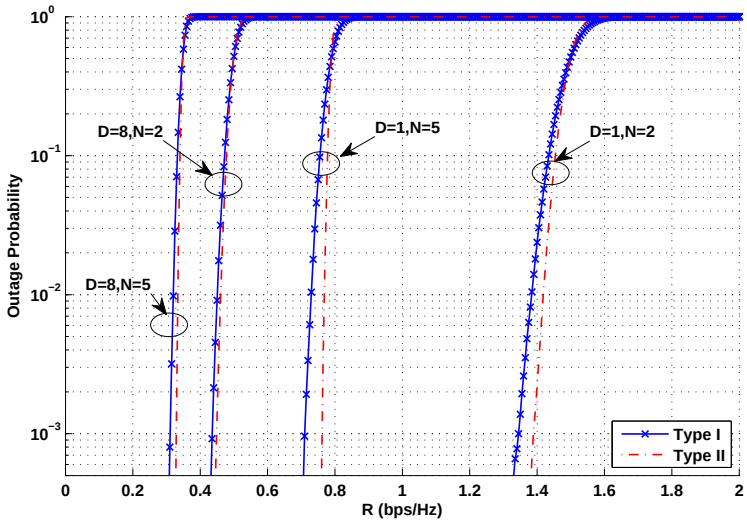

Figure 3.9: The normalized achievable rate with outage

user 1's type-I outage probability P_{out_I} as a representative of others. In Fig. 3.9, simulation is made with $L = 257$ and $\sigma_T = 128T_S$ under the normalized SNR level $\rho = 10dB$. As one can see, the slopes of curves in Fig. 3.9 are all very steep before the outage probabilities approach to 1. This indicates that the TR transmission technology could effectively combat the multi-path fading and makes the system behave in a more deterministic manner due to the *strong law of large numbers*. Such a property is highly desirable in a broad range of wireless communications, where link stability and reliability are prior concerns. Also, similar discounting effect on the achievable rate of rate back-off D is observed, and a larger N (number of users) would also reduce the individual achievable rate with the same outage probability due to its resulting larger IUI.

3.3.3 Achievable Rate Region Improvement over Rake receivers

In this part, we present TRDMA's improvement of achievable rate region over its counterpart, the rake receivers. Note that in the single-user case, by shifting the equalization from the receiver to the transmitter, time reversal bears some mathematical similarity to the rake receivers whose number of fingers is equal or close to the length of channel response. However, as shown in [2], for some broadband communications with typically tens to hundreds of paths, the complexity of rake receiver with such a large number of fingers is not practical. We demonstrate the advantage of TR structure over rake receivers in a multi-user scenario where spatial focusing effect of TR structure plays an important role, with the derivation of the two-user achievable rate region (the case of more users can be extended by defining a region in higher dimensional space). Specifically, we look at the TRDMA scheme and rake-receiver-based schemes in terms of the amount of information delivered (mutual information between input and output) within one single transmission, measured by bits per use of the multi-path channel.

Consider a two-user downlink scenario, where the transmitter has two independent information symbols X_1 and X_2 for two different receivers, respectively. The links between the transmitter and each receiver are modeled as a discrete multi-path channel with impulse responses h_1 and h_2 as in Section 3.1. Fig. 3.10 (a) shows a two-user single-antenna TRDMA scheme as introduced in this chapter; and Fig. 3.10 (b) shows a two-user rake-receiver based downlink solution. As we will show later, the proposed TRDMA scheme outperforms the rake-receiver based schemes

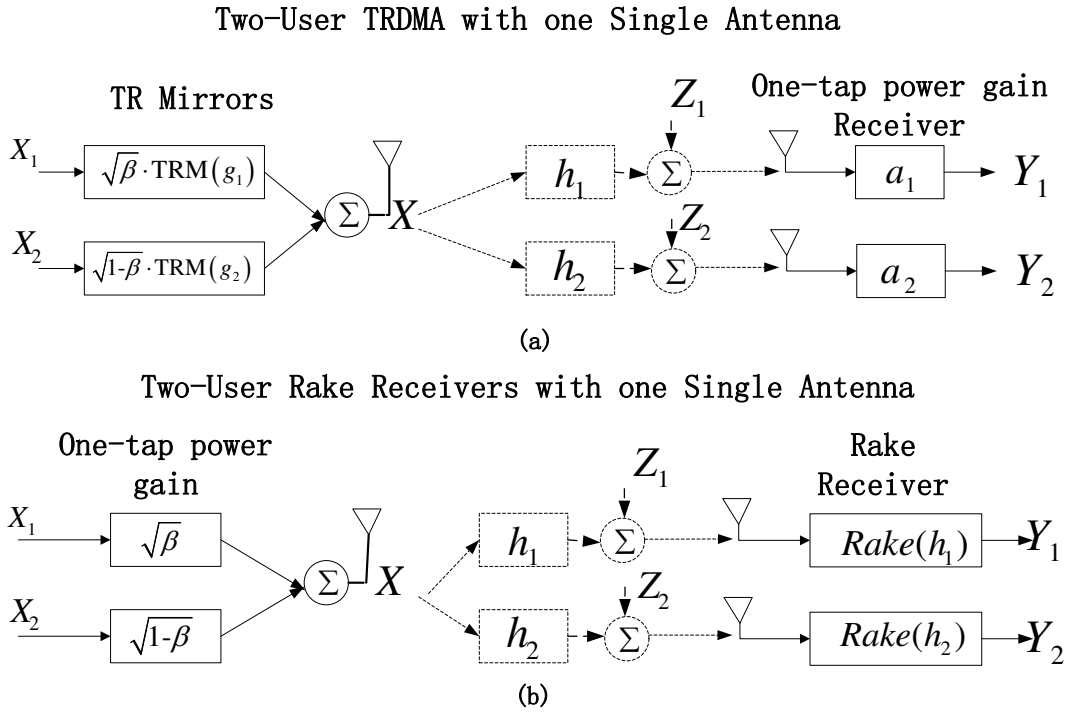

Figure 3.10: Two downlink systems

even when we assume that the number of fingers can be equal to the length of channel response and that the delay, amplitude and phase of each path can be perfectly tracked by the rake receiver.

3.3.3.1 Rake Receivers

For the ideal rake receivers in Fig. 3.10 (b), the equalized signals can be written as

$$Y_1 = ||h_1||_2 X + Z_1; \quad Y_2 = ||h_2||_2 X + Z_2, \tag{3.35}$$

where $||h_i||_2 = \sqrt{\sum_{l=0}^{L-1} |h_i(l)|^2}$ is the Euclidean norm of the channel response h_i, and Z_i is additive white Gaussian noise with zero-mean and variance σ_i^2. X is the transmitted signal, which is the combination of the two information symbols X_1 and

X_2.

One of the most intuitive way of combining X_1 and X_2 is to use orthogonal bases that allocate each user a fraction of the total available degrees of freedom [53]. In the two-user case, suppose that $X(t) = \sqrt{\beta}X_1c_1(t) + \sqrt{1-\beta}X_2c_2(t)$ where $c_1(t)$ and $c_2(t)$ are two orthonormal basis functions that assign a fraction $\alpha \in (0,1)$ of the total available degrees of freedom to user 1 and $(1-\alpha)$ to user 2. We consider the two-user achievable rate region with a total transmit power constraint. Specifically, let us assume that X_1 and X_2 are independent and identically distributed (i.i.d.) random variables with variance Φ, with the power allocation factor β such that the variance of X $var(X) = \left(\sqrt{\beta}\right)^2\Phi + \left(\sqrt{1-\beta}\right)^2\Phi = \Phi$.

Then, for the ideal rake receivers using orthogonal bases, the maximum achievable rate pair (R_1, R_2) in *bits per channel use* is given by [52]

$$\begin{aligned} R_1 &\leq \alpha \log_2\left(1 + \tfrac{\beta||h_1||_2^2\Phi}{\alpha\sigma_1^2}\right) \\ R_2 &\leq (1-\alpha)\log_2\left(1 + \tfrac{(1-\beta)||h_2||_2^2\Phi}{(1-\alpha)\sigma_2^2}\right), \end{aligned} \tag{3.36}$$

with all possible values $\alpha \in (0,1)$ and $\beta \in [0,1]$ defining the achievable rate region.

It has been shown that for the input-output correspondence shown in (3.35), the optimal frontier of the concurrently achievable rate pair is characterized by using superposition coding [54–57]. Without loss of generality, we assume that $\frac{\sigma_1^2}{||h_1||_2^2} \leq \frac{\sigma_2^2}{||h_2||_2^2}$, i.e. User 1's channel is advantageous to User 2's. Then the achievable rate region of the superposition coding is given by [52]

$$\begin{aligned} R_1 &\leq \log_2\left(1 + \tfrac{\beta||h_1||_2^2\Phi}{\sigma_1^2}\right) \\ R_2 &\leq \log_2\left(1 + \tfrac{(1-\beta)||h_2||_2^2\Phi}{\beta||h_2||_2^2\Phi + \sigma_2^2}\right) \end{aligned} \tag{3.37}$$

where $\beta \in [0,1]$ is the power allocation factor that defines the achievable rate region.

3.3.3.2 TRDMA Scheme and Genie-aided Outer-bound

For the TRDMA scheme with a single-tap receiver, when just one single transmission is considered, the input-and-output correspondence is reduced to

$$\begin{aligned} Y_1 =& \sqrt{\beta}||h_1||_2 X_1 + \sqrt{1-\beta}\,(h_1 * g_2)\,(L-1)\,X_2 + Z_1; \\ Y_2 =& \sqrt{1-\beta}||h_2||_2 X_2 + \sqrt{\beta}\,(h_2 * g_1)\,(L-1)\,X_1 + Z_2, \end{aligned} \tag{3.38}$$

where $g_i(l) = h_i^*(L-1-l)/||h_i||_2$ implemented by TRMs, and $(h_j * g_i)$ denotes the convolution of h_j and g_i.

Then, the resulting mutual information is obtained as follows

$$\begin{aligned} R_1 &\leq \log_2\left(1 + \tfrac{||h_1||_2^2\beta\Phi}{|(h_1*g_2)(L-1)|^2(1-\beta)\Phi+\sigma_1^2}\right) \\ R_2 &\leq \log_2\left(1 + \tfrac{||h_2||_2^2(1-\beta)\Phi}{|(h_2*g_1)(L-1)|^2\beta\Phi+\sigma_2^2}\right) \end{aligned} \tag{3.39}$$

where $\beta \in [0,1]$ is the power allocation factor that defines the achievable rate region.

Lastly, we derive a genie-aided outer-bound for the two-user capacity region, in which case all the interference is assumed to be known and thus can be completely removed. Such a genie-aided outer-bound can be obtained with $\beta \in [0,1]$ as follows

$$\begin{aligned} R_1 &\leq \log_2\left(1 + \tfrac{||h_1||_2^2\beta\Phi}{\sigma_1^2}\right) \\ R_2 &\leq \log_2\left(1 + \tfrac{||h_2||_2^2(1-\beta)\Phi}{\sigma_2^2}\right) \end{aligned} \tag{3.40}$$

3.3.3.3 Numerical Comparison

We present a numerical comparison of the capacity regions obtained in (3.36) (3.37) (3.39) and (3.40). In particular, we set $\frac{\Phi\ E\left[||h_1||_2^2\right]}{\sigma_1^2} = 10dB$ for User 1 and $\frac{\Phi\ E\left[||h_2||_2^2\right]}{\sigma_2^2} = 5dB$ for User 2. In Fig. 3.11, results are obtained by averaging over 1000 trials of multi-path Rayleigh fading channels. Each time, channel responses h_1

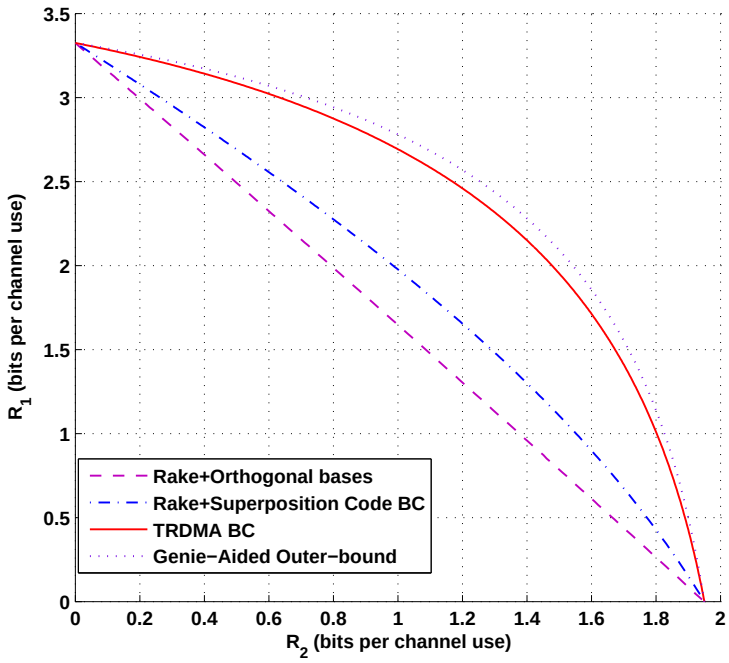

Figure 3.11: Achievable rate region for two-user case

and h_2 are randomly generated with parameters $L = 257$ and $\sigma_T = 128T_S$ according to the channel model in Section 3.1.

First, in Fig. 3.11, all the schemes achieve the same performances in the degraded single-user case, which corresponds to the two overlapping intersection points on the axes. This is due to the mathematical similarity between TR and Rake receivers in the single-user case and the commutative property of linear time-invariant (LTI) system. On the other hand, in most cases when both users are active, the proposed TRDMA scheme outperforms all the rake-receiver based schemes as shown in Fig. 3.11. Moreover, the frontier achieved by TRDMA is close to the Genie-aided outer-bound. All these demonstrate TRDMA's unique advantage of spatial focusing brought by the pre-processing of embedding location-specific signatures

before sending signals into the air. The high-resolution spatial focusing, as the key mechanism of the TRDMA, alleviates interference between users and provides a novel wireless medium access solution for multi-user communications.

3.4 Channel Correlation Effect

In the preceding sections, we assume a model of independent channels, because for rich-scattering multi-path profiles associated with reasonably far-apart (typically, several wavelengths) locations, they are often highly uncorrelated [27]. However, channels may become correlated when the environment is less scattering and users are very close to each other. To gain a more comprehensive understanding of TRDMA, it is also interesting and important to develop a quantitative assessment of its performance degradation due to spatial correlation between users.

3.4.1 Spatial Channel Correlation

Although there are many ways to model correlated channel responses, we herein choose to obtain correlated channel responses $\widehat{X}$ and $\widehat{Y}$ by performing element-wise linear combinations of independent channels X and Y as follows [50, 58, 59]

$$\begin{bmatrix} \widehat{X}(i) \\ \widehat{Y}(i) \end{bmatrix} = \begin{bmatrix} \sqrt{\xi} & \sqrt{1-\xi} \\ \sqrt{1-\xi} & \sqrt{\xi} \end{bmatrix} \begin{bmatrix} X(i) \\ Y(i) \end{bmatrix}, \tag{3.41}$$

where the coefficient $\xi \in [0, 1]$.

Before we proceed, we give a definition to *spatial correlation* of two multi-path channel responses.

Definition 3. *For two multi-path channel responses $\widehat{X}$ and $\widehat{Y}$, the spatial correlation of $\widehat{X}$ and $\widehat{Y}$ is defined as*

$$S_{\widehat{X}\widehat{Y}} = \frac{\sum_{i=0}^{L-1} \left| E\left[\widehat{X}(i)\widehat{Y}(i)^*\right] \right|}{\sqrt{\sum_{i=0}^{L-1} E\left[|\widehat{X}(i)|^2\right] \cdot \sum_{j=0}^{L-1} E\left[|\widehat{Y}(j)|^2\right]}}. \tag{3.42}$$

Note that this definition assumes zero-mean channel responses without loss of generality, and $S_{\widehat{X}\widehat{Y}}$ takes values between 0 and 1. Particularly, when $\widehat{X}$ and $\widehat{Y}$ are identical or additive inverse to each other, $S_{\widehat{X}\widehat{Y}} = 1$; when $\widehat{X}$ and $\widehat{Y}$ are uncorrelated, $S_{\widehat{X}\widehat{Y}} = 0$.

3.4.2 Channel correlation among users

For simplicity, we look at a two-user SISO case with correlated channel responses. We observe the impact of users' spatial correlation to the system performances.

Let us consider two correlated channel responses $\widehat{h}_1$ and $\widehat{h}_2$ obtained from the linear combination of two independent channel responses h_1 and h_2, as shown in (3.41), where $h_i[k]$'s are assumed as in Section 3.1 to be independent circular symmetric complex Gaussian random variables with zero mean and variance $E[|h_i[k]|^2] = e^{-\frac{kT_S}{\sigma_T}}$, for $0 \leq k \leq L-1$.

Then, the spatial correlation defined in (3.42) for $\widehat{h}_1$ and $\widehat{h}_2$ can be calculated by the simple form

$$S_{\widehat{h}_1\widehat{h}_2} = 2\sqrt{\xi(1-\xi)}. \tag{3.43}$$

Since the spatial correlation only affects the inter-user interference power, here we focus on the change of the average power of IUI as a result of channel correlations.

Similar to (3.17), the expected value of the new IUI power $\widehat{P}_{IUI}(i)$ at User i in such a two-user SISO case (i.e. $N = 2$ and $M_T = 1$) with the correlated channel responses $\widehat{h}_1$ and $\widehat{h}_2$ can be written as

$$E\left[\widehat{P}_{IUI}(i)\right] = \theta E\left[\sum_{l=0}^{\frac{2L-2}{D}} \left|\left(\widehat{h}_i * \widehat{g}_j\right)[Dl]\right|^2\right], \tag{3.44}$$

where $j \neq i$ $(i, j \in \{1, 2\})$, and the TRM

$$\widehat{g}_j[k] = \widehat{h}_j^*[L-1-k] \Big/ \sqrt{E\left[\sum_{l=0}^{L-1}\left|\widehat{h}_j[l]\right|^2\right]}$$

corresponds to User j with the channel response $\widehat{h}_j$.

A direct calculation of (3.44) can be tedious. However, by substituting uncorrelated h_1 and h_2 into (3.44) according to the linear transform (3.41), we can utilize the existing results in Section 3.2 and represent the expected value of $\widehat{P}_{IUI}(i)$ in terms of $E\left[P_{Sig}(i)\right]$, $E\left[P_{ISI}(i)\right]$, and $E\left[P_{IUI}(i)\right]$ in (3.19-3.21) calculated with respect to uncorrelated h_1 and h_2, as presented in (3.45).

$$E\left[\widehat{P}_{IUI}(i)\right] = E\left[P_{IUI}(i)\right] + \frac{S^2_{\widehat{h}_1\widehat{h}_2}}{2} E\left[P_{Sig}(i) + P_{ISI}(i) - P_{IUI}(i) + \theta\sum_{l=0}^{L-1}|h_i[l]|^2\right], \tag{3.45}$$

Note that in (3.45), the second term

$$E\left[P_{Sig}(i) + P_{ISI}(i) - P_{IUI}(i) + \theta\sum_{l=0}^{L-1}|h_i[l]|^2\right]$$

is always positive, which is a penalty to the system performance due to the two users' spatial correlation. When $S_{\widehat{h}_1\widehat{h}_2} = 0$ (i.e. $\xi = 0$ or $\xi = 1$), $\widehat{h}_1$ and $\widehat{h}_2$ are uncorrelated, and thus $E\left[\widehat{P}_{IUI}(i)\right] = E\left[P_{IUI}(i)\right]$. In the extreme case when $S_{\widehat{h}_1\widehat{h}_2} = 1$ (i.e. $\xi = 0.5$) that maximizes (3.45), $\widehat{h}_1$ and $\widehat{h}_2$ are identical, the IUI

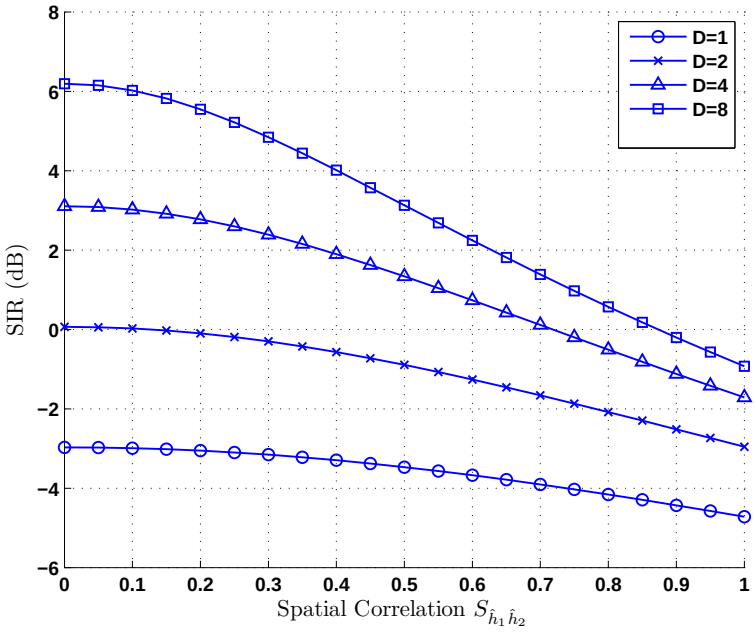

Figure 3.12: SIR vs spatial correlation with $N = 2$ and $M_T = 1$

achieves its upper-bound

$$E\left[\widehat{P}_{IUI}(i)\right] = \frac{E\left[P_{Sig}(i) + P_{ISI}(i) + P_{IUI}(i)\right] + \theta E\left[\sum_{l=0}^{L-1} |h_i[l]|^2\right]}{2}. \tag{3.46}$$

Since $E\left[P_{Sig}(i) + P_{ISI}(i)\right] = E\left[P_{IUI}(i)\right] + \theta E\left[\sum_{l=0}^{L-1} |h_i[l]|^2\right]$ at $D = 1$, (3.46) can be written as $E\left[\widehat{P}_{IUI}(i)\right] = E\left[P_{Sig}(i)\right] + E\left[P_{ISI}(i)\right]$, when there is no rate back-off.

The impact of the increased interference would be most prominent in the high SNR regime, where the interference power dominates the noise power. So we evaluate its impact to the system performance in terms of signal-to-interference ratio (SIR), as a close approximation of the effective SINR in high SNR regime. Fig. 3.12 shows the influence of the spatial correlation to the SIR with correlated channel responses $\widehat{h}_1$ and $\widehat{h}_2$ of length $L = 257$ and delay spread $\sigma_T = 128T_S$. As one can

see in Fig. 3.12, the SIR degradation speed varies with different ranges of $S_{\widehat{h}_1\widehat{h}_2}$. In the lower range of $S_{\widehat{h}_1\widehat{h}_2}$ (e.g. from 0 to 0.2) the SIR degrades very slowly. Also, the larger rate back-off D tends to result in a faster performance loss due to spatial correlation as shown in Fig. 3.12. However, even for $S_{\widehat{h}_1\widehat{h}_2}$ up to 0.5 which is rare in real-life RF communications over scattering environments, the degraded SIR is preserved within $3dB$ away from the performances of uncorrelated channels. This demonstrates the robustness of the proposed TRDMA scheme and provides a more comprehensive understanding of its system performances.

3.5 Summary

In this chapter, we proposed a TRDMA scheme for the multi-user downlink network over multi-path channels. Both single-antenna and multi-antenna schemes were developed to utilize the location-specific signatures that naturally exist in the multi-path environment. We defined and evaluated both analytically and numerically a variety of performance metrics of including the effective SINR, the achievable sum rate, and achievable rates with outage. We then demonstrated the TRDMA's improvement of achievable rate region over the rake receivers and investigated the impact of spatial correlations between users to the system performances. Based on the nice properties shown in the analysis and simulation results of this chapter, the proposed TRDMA can be a promising technique in the future energy-efficient low-complexity broadband wireless communications.

Chapter 4: TRDMA Based Multi-User Broadband Networks

From the analysis of the system performance of TRDMA scheme in Chapter 3, one can see that TRDMA scheme can efficiently exploits the spatial degrees of freedom of the environment and uses the multi-path channel profile associated with each user's location as a location-specific signature for the user. Based on the concept of TRDMA, in this chapter, we present a TRDMA based multi-user broadband network, which facilitates two-way communications between a BS and multiple terminal users. Multiple independent high-speed data streams can be multiplexed with little co-channel interference by embedding the location-specific signature waveforms into these streams. Thanks to the spacial focusing effect, useful signal paths can resonate at the intended location, and significantly lower interference power is observed for the other users.

In this chapter, we first introduce a TRDMA uplink scheme and show its strong duality with the TRDMA downlink scheme presented in Chapter 3. The proposed TRDMA uplink and downlink schemes facilitate a unique asymmetric architecture of the TRDMA based multi-user network, in which the higher processing capability and channel knowledge available at the BS can be reused, resulting in a minimal complexity and cost at the terminals in both uplink and downlink. Such an

asymmetric complexity distribution is very desirable for many infrastructure-based wireless applications, which helps reduce the overall system cost and improve scalability. Another unique feature of the TRDMA system is that in essence the time reversal technique treats each path in the environment as a virtual antenna, which collectively contributes to the energy focusing capability and explores the spatial degrees of freedom. In the second half of this chapter, we investigate this feature by conducting a comparative study of the TRDMA system and massive multiple-input-multiple-output (MIMO) system.

4.1 An Asymmetric Architecture for TRDMA Multi-User Network

Consider a wireless broadband multi-user network that consists of one BS and N terminal users, where each user communicates with BS simultaneously over the same spectrum, as shown in Fig. 4.1. Assuming a rich-scattering environment, each user's location is associated with a unique channel response $\{h_i[k]\}$, $i = 1, 2, \cdots, N$. The downlink and uplink occur at different times, i.e. the system adopts the time-division duplexing (TDD).

4.1.1 TRDMA Uplink Scheme

Fig. 4.2 shows the block diagram of the TRDMA uplink scheme. As shown in Fig. 4.2, N users simultaneously transmit independent messages

$$\{X_1[k], X_2[k], \cdots, X_N[k]\}$$

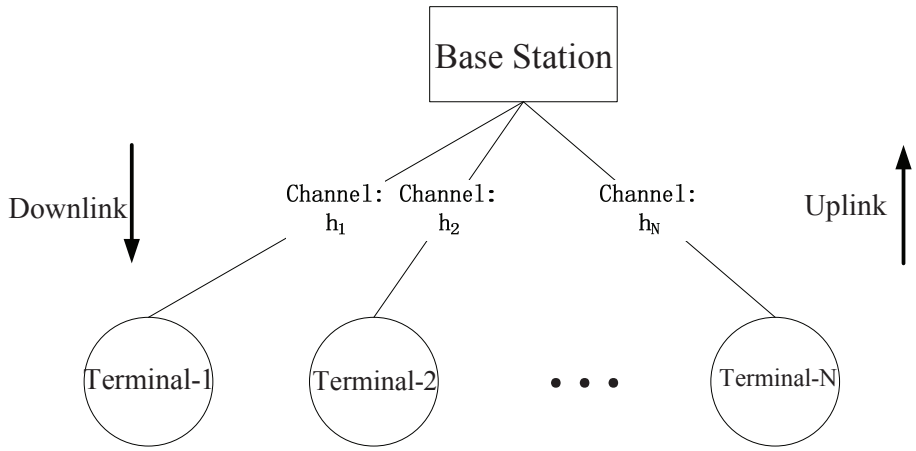

Figure 4.1: The TRDMA based multi-user network

to the BS. For any given User i in the uplink network, the channel h_i between the BS and User i is a multi-path channel characterized by a unique discrete-time[1] channel impulse response (CIR):

$$h_i[k] = \sum_{l=0}^{L-1} h_{i,l}\delta[k-l], \tag{4.1}$$

where $h_{i,l}$ is the l-th tap of the CIR with length L, and $\delta[\cdot]$ is the Dirac delta function. We assume that the channels are quasi-static and reciprocal, which can be acquired at the BS through a channel probing phase [2, 60]. During the channel probing phase, each user takes turns to send impulse signal[2] to the BS so that the channel impulse response (CIR) $\{h_i[k]\}$ of each user's link can be recorded by the TRM at the BS. Upon recording the CIR, the TRM will reverse the recorded waveform in the time-domain and normalize it as the unique signature waveform of User i [60].

[1] as a result of the analog-to-digital convertor (ADC)

[2] Although it is difficult to send an ideal impulse in practice which would require infinite bandwidth, a modified raise-cosine signal can be a good candidate for limited bandwidth for this purpose [2]

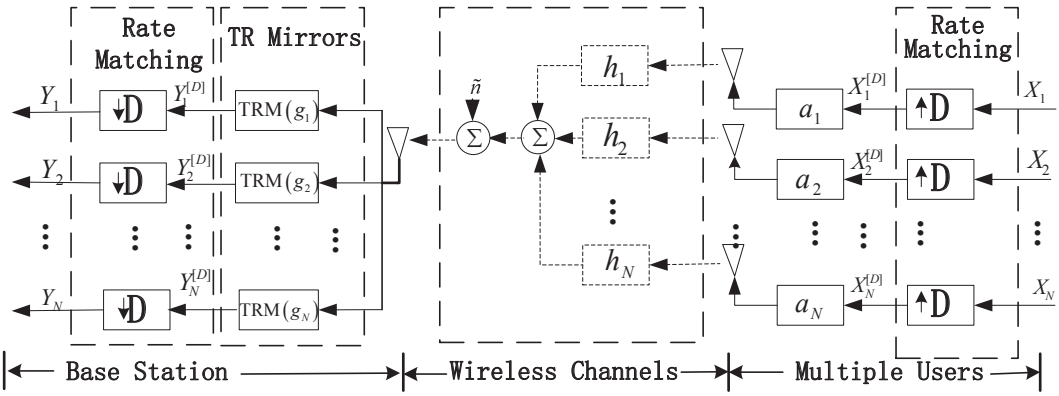

Figure 4.2: The diagram of TRDMA multiuser uplink system

The time-reversed waveform of User i will be used in the data transmission phase to extract the desired signal from a combination of the multiple access signals that are mixed in the air. Specifically, the time-reversed signature waveform of User i can be written as

$$g_i[k] = h_i^*[L-1-k] \Big/ \sqrt{\sum_{l=0}^{L-1} |h_i[l]|^2}\,. \tag{4.2}$$

After the channel probing phase, the users can start to transmit the statistically independent messages $\{X_1[k], X_2[k], \cdots, X_N[k]\}$ to the BS through the multipath channels. A rate back-off factor D is introduced to match the symbol rate (signal bandwidth) with the much higher system's sampling rate (channel bandwidth). For any user U_i, $i \in \{1, 2, \ldots, N\}$, the rate matching process is performed by up-sampling the sequence of modulated symbols $\{X_i[k]\}$ by a factor D, as shown in Fig. 4.2. The up-sampled sequence of modulated symbols for User i can be

expressed as

$$X_i^{[D]}[k] = \begin{cases} X_i[k/D], & \text{if } k \bmod D = 0, \\ 0, & \text{if } k \bmod D \neq 0. \end{cases} \tag{4.3}$$

The scaling factors a_i, for $i \in \{1, 2, \ldots, N\}$ in Fig. 4.2 are used to implement the transmit power control, whose values are assumed to be instructed by the BS through the feedback/control channel. After multiplying with scaling factor, the sequence of $a_i X_i^{[D]}[k]$ for all $i \in \{1, 2, \ldots, N\}$, is transmitted through the corresponding multi-path channel $\{h_i[k]\}$.

When the sequence $\{a_i X_i^{[D]}[k]\}$ propagates through its wireless channel $\{h_i[k]\}$, the convolution between $\{a_i X_i^{[D]}[k]\}$ and the CIR $\{h_i[k]\}$ is automatically taken as the channel output for User i. Then, all of the channel outputs for the N users are mixed together in the air plus the additive white Gaussian noise (AWGN) $\tilde{n}[k]$ at the BS with zero mean and variance σ_N^2, as illustrated in Fig. 4.2. Consequently, the mixed signal received at the BS can be written as

$$S[k] = \sum_{i=1}^{N} a_i \left(h_i * X_i^{[D]} \right)[k] + \tilde{n}[k]. \tag{4.4}$$

Upon receiving the mixed signal as shown in (4.4), the BS passes this mixed signal through a bank of N TRMs, each of which performs the convolution between its input signal $\{S[k]\}$ and the user's signature waveform $\{g_i[k]\}$. Such a convolution using the signature waveform exacts the useful signal component and suppresses the signals of other users. As the output of the i-th TRM, the convolution of $\{S[k]\}$

and the signature of User i $\{g_i[k]\}$ can be represented as

$$\begin{aligned} Y_i^{[D]}[k] &= \sum_{j=1}^{N} a_j \left(g_i * h_j * X_j^{[D]} \right)[k] + (g_i * \tilde{n})[k] \\ &= \sum_{j=1}^{N} \sum_{l=0}^{2L-2} a_j \left(g_i * h_j \right)[l] X_j^{[D]}[k-l] + (g_i * \tilde{n})[k], \end{aligned} \tag{4.5}$$

in which the highest gain for User i's symbol is achieved at the temporal focusing time $l = L-1$, with

$$\left(g_i * h_i \right)[L-1] = \sqrt{\sum_{l=0}^{L-1} |h_i[l]|^2}. \tag{4.6}$$

Then the rate matching is performed by down-sampling (with the same factor D) the TRMs' output signal to recover the original symbol rate of the modulated symbols of each user.

After the rate matching, the down-sampled TRM output $Y_i[k]$ can be obtained as[3]

$$Y_i[k] = \sum_{j=1}^{N} \sum_{l=-\lfloor \frac{L-1}{D} \rfloor}^{\lfloor \frac{L-1}{D} \rfloor} a_j \left(g_i * h_j \right)[L-1+Dl] X_j[k-l] + n_i[k], \tag{4.7}$$

where the colored noise $n_i[k] = \sum_{l=0}^{L-1} g_i[l] \tilde{n}[Dk-l] = \underline{g}_i \underline{\tilde{n}}[k]$ with

$$\underline{g}_i \triangleq \left[g_i[0], g_i[1], \cdots, g_i[L-1] \right]$$

and $\underline{\tilde{n}}[k] \triangleq [\tilde{n}[k], \tilde{n}[k-1], \ldots, \tilde{n}[k-L+1]]^T$. Note that the colored noise $\{n_i[k]\}$ is still a Gaussian random variable with zero mean and the same variance σ_N^2, since $\{g_i\}$ is a normalized waveform as shown in (4.2).

[3]More rigorously, here $Y_i[k] = Y_i^{[D]}[L-1+Dk]$ which aligns the highest temporal focusing gain $(g_i * h_i)[L-1]$ in $Y_i[k]$ with the transmitted symbol $X_i[k]$ in time for ease of simple notation.

Decomposing the signal shown in (4.7), we have the following components as

$$
\begin{aligned}
Y_i[k] = {} & a_i \left(g_i * h_i\right)[L-1] X_i[k] && (Signal) \\
& + a_i \sum_{\substack{l=-\lfloor \frac{L-1}{D} \rfloor \\ l \neq 0}}^{\lfloor \frac{L-1}{D} \rfloor} \left(g_i * h_i\right)[L-1+Dl] X_j[k-l] && (ISI) \\
& + \sum_{\substack{j=1 \\ j \neq i}}^{N} a_j \sum_{l=-\lfloor \frac{L-1}{D} \rfloor}^{\lfloor \frac{L-1}{D} \rfloor} \left(g_i * h_j\right)[L-1+Dl] X_j[k-l] && (IUI) \\
& + n_i[k]. && (Noise)
\end{aligned} \tag{4.8}
$$

Consequently, based on (4.8), the resulting SINR for User i in the TRDMA uplink is given by

$$
SINR_{UL}^{i} = \frac{P_{sig}^{UL}(i)}{P_{ISI}^{UL}(i) + P_{IUI}^{UL}(i) + \sigma_N^2} \tag{4.9}
$$

where

$$
P_{sig}^{UL}(i) = |a_i|^2 \sum_{l=0}^{L-1} |h_i[l]|^2 , \tag{4.10}
$$

$$
P_{ISI}^{UL}(i) = |a_i|^2 \sum_{\substack{l=-\lfloor \frac{L-1}{D} \rfloor \\ l \neq 0}}^{\lfloor \frac{L-1}{D} \rfloor} \left|\left(g_i * h_i\right)[L-1+Dl]\right|^2 , \tag{4.11}
$$

$$
P_{IUI}^{UL}(i) = \sum_{\substack{j=1 \\ j \neq i}}^{N} |a_j|^2 \sum_{l=-\lfloor \frac{L-1}{D} \rfloor}^{\lfloor \frac{L-1}{D} \rfloor} \left|\left(g_i * h_j\right)[L-1+Dl]\right|^2 . \tag{4.12}
$$

4.1.2 A Virtual Spatial Focusing for the TRDMA Uplink

Examining the equation (4.5) and the received signal at the terminal users in the downlink (3.5), the same mathematical structure can be found by switching the roles of the signature waveforms $\{g_i\}$s and the CIRs h_is in the convolution

(and ignoring the scaling factor a_i and noise term.) Therefore, mathematically[4], a virtual spatial focusing effect as observed in the downlink can be seen in the user's signature domain of the proposed uplink scheme. Such a virtual spatial focusing effect enables the BS to use the user's signature waveform to extract the useful component out of the combined received signals, allowing multiple users accessing the BS simultaneously.

4.1.3 Advantages of the Asymmetric Architecture

Comparing the downlink and uplink schemes, one can see that

- In both downlink and uplink, the BS assumes most of the complexity, while keeping the complexity of terminal users at a minimal level. This is a very desirable feature for the solution of Internet of things, which reduces the cost of the terminal devices and thus the entire system as a whole.

- The channel knowledge acquired by BS through channel probing and the corresponding signature waveform are utilized for both downlink and uplink. There is no need to perform channel probing and signature-waveform calculation separately for downlink and uplink.

- Both downlink and uplink can support simultaneous transmissions of multiple users. The downlink has a physical spatial focusing effect; whereas the uplink

[4]Unlike the *physical* spatial focusing effect observed in the downlink in which the useful signal power is concentrated at different physical locations, in the uplink, the signal power concentration in the users' signature waveform space is achieved mathematically at the BS.

has a virtual spatial focusing effect due to the mathematical duality between the TRDMA uplink and downlink.

4.2 TRDMA–An Equivalent Massive MIMO Technology

Lately, an emerging research area of massive MIMO technology attracts a lot of attention and exhibits great potential to achieve significant performance gain [61–68]. It has been well known that the MIMO technique has many advantages in improving the performance of wireless communications, and has been developed into a mature technique adopted by many modern wireless communication systems. Basically, it has been proved that as the number of antennas increase, the potential gain of the MIMO technique will also increase. The concept of massive MIMO system aims to take the advantages of conventional MIMO systems to a higher level by increasing the number of the antennas to an order of magnitude larger number than the conventional MIMO system, so that the system performance gain such as the diversity gain, system throughput, and spatial focusing and interference suppression can be further enhanced, as the number of antennas increase.

As will be shown in this section, the time reversal in essence, forms a virtual massive MIMO technology that leverages the large number of multi-paths in the rich-scattering environment. In the remaining parts of this section, we show a comparative study of the time reversal and the massive MIMO schemes, and investigate the system performance in terms of the diversity gain, the spatial focusing gain, and the spatial multiplexing gain.

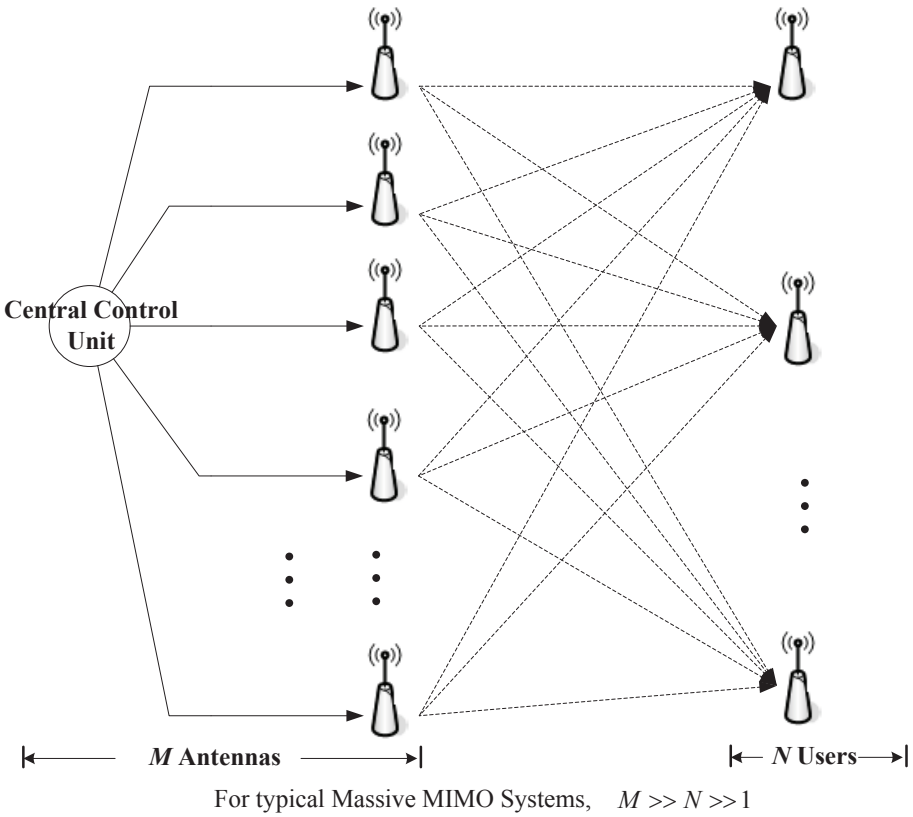

Figure 4.3: The massive MIMO system

Fig. 4.3 shows an example of the massive MIMO system with M antennas connected to a central control unit, and N users each equipped with one single antenna. The central control unit calculates the phase and amplitude of each antenna's transmitted signal, so that the M antennas can collectively perform beamforming for each of the N users.

We look at a narrow-band massive MIMO system. Denote the channel coefficient between the i-th antenna to the j-th user as $\hat{h}_{i,j}$, which is modeled as a circularly symmetric complex Gaussian random variable with zero mean and variance Γ_1, i.e., $\hat{h}_{i,j} \sim \mathcal{CN}(0, \Gamma_1)$. We further assume that for different (i, j), the channel coefficients are independent and identically distributed (i.i.d.), for ease of analysis.

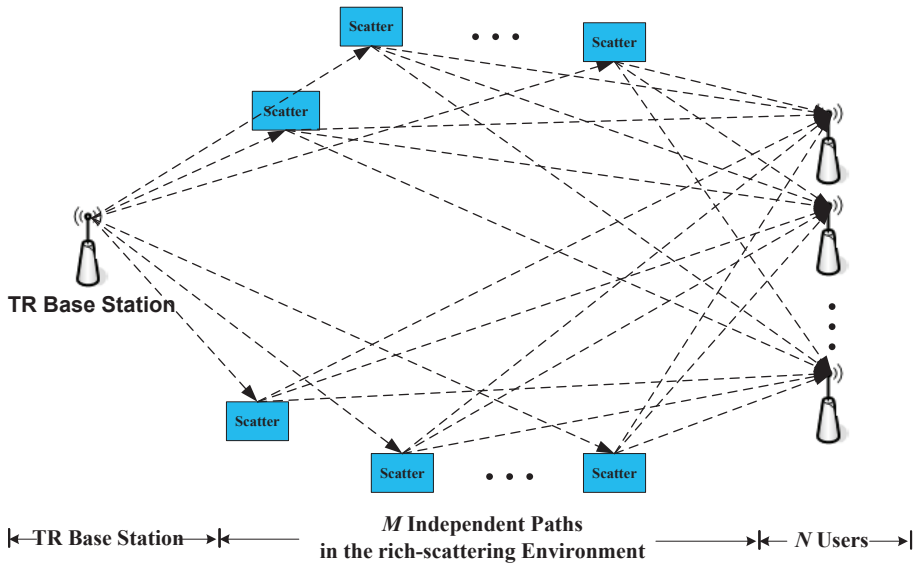

Figure 4.4: The time reversal as a virtual massive MIMO system

For typical massive MIMO systems, it holds that $M \gg N \gg 1$. The very large number of transmit antennas M leads to many signal-paths arriving at each user. When the phase and amplitude are carefully tuned by the central control unit, the useful signal energy can be concentrated at the location of the intended user due to a constructive sum of the signal paths. Therefore, such a massive MIMO effect on the one hand can more efficiently deliver the signal energy to the intended user, on the other hand it suppresses the co-channel interference, facilitating spatial multiplexing.

Now consider a broadband TRDMA network in a rich-scattering environment, where there are N users each equipped with one single antenna, and one single-antenna base station (BS), as shown in Fig. 4.4. The broader bandwidth allows a shorter pulse duration which gives rise to a higher resolution in the time domain to resolve two adjacent paths. For the purpose of comparison, given a certain system

bandwidth, we assume that there are M resolvable independent multi-paths in the channel response between the base station and each user.

Specifically, denote the coefficient of the v-th resolvable path between the BS to the j-th user as $\tilde{h}_{v,j}$, which are similarly assumed as i.i.d. $\tilde{h}_{v,j} \sim \mathcal{CN}(0, \Gamma_2)$. When the TR signature waveform is transmitted, the TR waveform will retrace each of the signal paths towards the intended user, and in essence treats all the paths in the environment as virtual antennas and focus the signal energy only at the intended location, where the signals of many paths are added constructively.

4.2.1 Spatial Diversity Gain

In this part, we investigate the the spatial diversity gain achieved in the two schemes. Consider a single user scenario (with $N = 1$) for both schemes, where the massive MIMO system is a narrow-band system equipped with M transmit antenna and the TRDMA is a single-antenna broadband system with M resolvable multi-paths between the BS to the user.

For the massive MIMO scheme, assuming that the channel state information is available at the BS (as a fair comparison with TR with channel probing), the beamforming coefficients are calculated by the central control unit and sent to each of the M antennas. Given the channel coefficients $\{\hat{h}_{v,1}\}$, the optimal beamforming coefficient for the i-th antenna $\hat{g}_{v,1}$ is given as follows:

$$\hat{g}_{v,1} = \frac{\sqrt{P} \cdot \hat{h}^*_{v,1}}{\sqrt{\sum_{v=1}^{M} \left|\hat{h}_{v,1}\right|^2}}, \tag{4.13}$$

where P is the total transmit power.

As a result, the received SNR at receiver (User 1) is

$$SNR_{\texttt{M-MIMO}} = \frac{P}{\sigma_N^2} \sum_{v=1}^{M} \left| \hat{h}_{v,1} \right|^2, \tag{4.14}$$

where σ_N^2 is the noise power at the receiver.

The channel outage probability for the massive MIMO system shown in Fig. 4.3 can be obtained as

$$\begin{aligned} P_{\texttt{Outage,M-MIMO}} &= \Pr\left[SNR_{\texttt{M-MIMO}} \leqslant \gamma_1\right] \\ &= \Pr\left[\sum_{v=1}^{M} \left| \hat{h}_{v,1} \right|^2 \leqslant \frac{\gamma_1 \sigma_N^2}{P}\right], \end{aligned} \tag{4.15}$$

where γ_1 is a certain QoS threshold.

For the time reversal system, when the rate back-off factor D is large so that the ISI power is negligible to the noise power, the TR waveform will result in a received SNR for the time reversal system as follows:

$$SNR_{\texttt{TR}} = \frac{P}{\sigma_N^2} \sum_{v=1}^{M} \left| \tilde{h}_{v,1} \right|^2. \tag{4.16}$$

The channel outage probability of the time reversal system is given by

$$\begin{aligned} P_{\texttt{Outage,TR}} &= \Pr\left[SNR_{\texttt{TR}} \leqslant \gamma_2\right] \\ &= \Pr\left[\sum_{v=1}^{M} \left| \tilde{h}_{v,1} \right|^2 \leqslant \frac{\gamma_2 \sigma_N^2}{P}\right]. \end{aligned} \tag{4.17}$$

Given the identical structure of (4.15) and (4.17), denoting $(z_1, z_2, \cdots, z_M)$ as i.i.d. circularly symmetric complex Gaussian random variables $\mathcal{CN}(0, \Gamma)$, we could

have a unified calculation as the following

$$\begin{aligned} P_{\texttt{outage}} &= \Pr\left[\sum_{j=1}^{M} |z_j|^2 \leqslant \gamma \frac{\sigma_N^2}{P}\right] \\ &\leqslant \Pr\left[\max_{j\in\{1,2,\cdots,M\}} |z_j|^2 \leqslant \gamma \frac{\sigma_N^2}{P}\right] \\ &= \prod_{j=1}^{M} \Pr\left[|z_j|^2 \leqslant \gamma \frac{\sigma_N^2}{P}\right] \\ &= \left(\Pr\left[|z_j|^2 \leqslant \gamma \frac{\sigma_N^2}{P}\right]\right)^M \\ &= \left(1 - \exp\left(\frac{\gamma\sigma_N^2}{\Gamma P}\right)\right)^M \\ &\approx \left(\frac{\gamma}{\Gamma}\right)^M \left(\frac{P}{\sigma_N^2}\right)^{-M} \end{aligned} \tag{4.18}$$

where $\Gamma = \Gamma_1$ or Γ_2, and $\gamma = \Gamma_1$ or γ_2 for massive MIMO and time reversal, respectively.

From (4.18), one can see that a diversity order of up to M can be achieved by either of the massive MIMO and time reversal scheme. Note that in the calculation of (4.18), a suboptimal scheme of using only the strongest path is used to obtain an upper bound of the outage probability of the time reversal scheme (as well as the massive MIMO scheme). With the energy focusing capability, both time reversal and massive MIMO can optimally combine the energy of all the paths, whose advantage over the suboptimal scheme is demonstrated by the *spatial focusing gain*.

4.2.2 Spatial Focusing Gain

In this part, we study the spatial focusing capability of the massive MIMO system and the time reversal system. We first introduce a performance metric to

measure the energy focusing capability of the two schemes, namely *spatial focusing gain*[5]

Definition 4. (Spatial Focusing Gain) *The spatial focusing gain is defined as the ratio of the average power of the strongest peak of the focused signal (due to the energy focusing schemes) to the average power of the strongest path among all the multiple signal paths of the channel response.*

For a narrow-band[6] massive MIMO system as shown in Fig. 4.3, the optimal transmitted signal $\tilde{g}_{i,1}$ in (4.13) is used to perform a massive beamforming to focus signal energy towards the intended receiver. Accordingly, the peak power of the resulting received signal at receiver (User 1) is

$$Z_{\text{M-MIMO}} = P \sum_{v=1}^{M} \left| \hat{h}_{v,1} \right|^2 . \tag{4.19}$$

When only the antenna associated with the strongest channel gain is used, the received signal power is given by

$$Z_{\text{single-antenna}} = P \cdot \max_{v \in \{1,2,\cdots,M\}} \left\{ \left| \hat{h}_{v,1} \right|^2 \right\}, \tag{4.20}$$

For time reversal system, given the channel response $\tilde{h}_1$, when the TR waveform $\tilde{g}_1$ is transmitted, the energy of all the resolvable multi-paths will be harvested at the location of the receiver, i.e.

$$Z_{\text{TR}} = P \sum_{v=1}^{M} \left| \tilde{h}_{v,1} \right|^2 \tag{4.21}$$

[5]similar definitions can be found for deterministic channels in literature such as [69].

[6]As a result, the channel impulse response between each transmit antenna and each user has only one tap.

As a comparison, the direct transmission (DT) scheme, where the transmitter only transmit a pulse signal $p(t)$, the peak power of the resulting received signal at the receiver is proportional to the gain of the strongest resolvable path, i.e.

$$Z_{\mathrm{DT}} = P \cdot \max_{v\in\{1,2,\cdots,M\}} \left\{ \left| \tilde{h}_{v,1} \right|^2 \right\}. \tag{4.22}$$

Consequently, by Definition 4, the spatial focusing gains for the massive MIMO and the time reversal are given by

$$\Phi_{\text{M-MIMO}}(M) = \frac{E\left[\sum_{v=1}^{M} \left| \hat{h}_{v,1} \right|^2\right]}{E\left[\max_{v} \left\{ \left| \hat{h}_{v,1} \right|^2 \right\}\right]}, \tag{4.23}$$

and

$$\Phi_{\mathrm{TR}}(M) = \frac{E\left[\sum_{v=1}^{M} \left| \tilde{h}_{v,1} \right|^2\right]}{E\left[\max_{v} \left\{ \left| \tilde{h}_{v,1} \right|^2 \right\}\right]}, \tag{4.24}$$

respectively.

Considering $(z_1, z_2, \cdots, z_M)$ i.i.d., $\mathcal{CN}(0,\Gamma)$, (4.23) and (4.24) can be calculated the following equation

$$\Phi(M) = \frac{E\left[\sum_{v=1}^{M} |z_v|^2\right]}{E\left[\max_{v\in\{1,2,\cdots,M\}} \left\{ |z_v|^2 \right\}\right]}. \tag{4.25}$$

In (4.25), it is easy to have that $E\left[\sum_{v=1}^{M} |z_v|^2\right] = M\Gamma$, and thus the problem reduces to the calculation of $E\left[\max_{v\in\{1,2,\cdots,M\}} \left\{ |z_v|^2 \right\}\right]$.

Denoting $Q(M) \triangleq \max_{v\in\{1,2,\cdots,M\}} \left\{ |z_v|^2 \right\}$,

$$E\left[Q(M)\right] = \int_0^{\infty} \left(1 - F_{Q(M)}(q)\right) dq, \tag{4.26}$$

where $F_{Q(M)}(q)$ is the CDF of $Q(M) = \max_{v\in\{1,2,\cdots,M\}} \left\{|z_v|^2\right\}$, which is given as follows:

$$F_{Q(M)}(q) = \left(1 - e^{-\frac{q}{\Gamma}}\right)^M \quad (q \geqslant 0) \tag{4.27}$$

Therefore, for any given $M \geqslant 2$,

$$\begin{aligned} E\left[Q(M)\right] &= \int_0^\infty \left[1 - \left(1 - e^{-\frac{q}{\Gamma}}\right)^M\right] dq \\ &= \int_0^\infty \left[1 - \left(1 - e^{-\frac{q}{\Gamma}}\right)^{M-1} \left(1 - e^{-\frac{q}{\Gamma}}\right)\right] dq \\ &= E\left[Q(M-1)\right] + \int_0^\infty e^{-\frac{q}{\Gamma}} \left(1 - e^{-\frac{q}{\Gamma}}\right)^{M-1} dq \\ &= E\left[Q(M-1)\right] + \frac{\Gamma}{M}, \end{aligned} \tag{4.28}$$

In particular, when $M = 1$,

$$E\left[Q(1)\right] = \int_0^\infty \exp\left(-\frac{q}{\Gamma}\right) = \Gamma. \tag{4.29}$$

Therefore,

$$E\left[Q(M)\right] = \Gamma \sum_{m=1}^{M} \frac{1}{m}. \tag{4.30}$$

The spatial focusing gain is then given by

$$\Phi_{\text{M-MIMO}}(M) = \Phi_{\text{TR}}(M) = \Phi(M) = \left(\frac{1}{M} \sum_{m=1}^{M} \frac{1}{m}\right)^{-1} \tag{4.31}$$

4.2.3 Spatial Multiplexing Gain

It has been long been known that the multi-antenna system can be also used to exploit the spatial degrees of freedom for multiplexing. In this case, the desirable spatial selectivity can be achieved by performing the beamforming of the multiple

antennas to effectively suppress the co-channel interference among multiple concurrent users. Such a scheme has been commonly referred to as spatial division multiple access (SDMA). Compared with conventional antenna-array based beamforming SDMA schemes, the TRDMA technique leverages a large number of multi-paths and in essence treats each path as a virtual antenna that naturally exists and is widely distributed in environments for broadband communication systems.

Thus, with even just one single transmit antenna, time reversal can potentially achieve a very high-resolution "pin-point" spatial focusing. The high-resolution spatial focusing effect maps the natural multi-path propagation profile into a unique *location-specific signature* for each link. The proposed TRDMA scheme exploits the uniqueness and independence of location-specific signatures in multi-path environment, providing a novel low-cost energy-efficient solution for SDMA.

In principle, for MIMO system, denoting a channel coefficient matrix $\hat{H}$ as

$$\hat{H} \triangleq \begin{bmatrix} \hat{h}_{1,1} & \hat{h}_{2,1} & \cdots & \hat{h}_{M,1} \\ \hat{h}_{1,2} & \hat{h}_{2,2} & \cdots & \hat{h}_{M,2} \\ \vdots & \vdots & \ddots & \vdots \\ \hat{h}_{1,N} & \hat{h}_{2,N} & \cdots & \hat{h}_{M,N} \end{bmatrix}, \tag{4.32}$$

the maximum multiplexing order is given by $Rank(\hat{H}) \leqslant \min\{M, N\}$. For typical massive MIMO systems, it holds that $M \gg N$, which gives rise to a high probability that $Rank(\hat{H}) = N$, assuming that the channel coefficients in $\hat{H}$ are independent. In other words, the abundant number of the available antennas can exploit more spatial degrees of freedom, so that it can support more concurrent users with higher probability.

When it comes to TRDMA, although the channel response can be a continuous-time function, its degrees of freedom, however, is limited to the maximum number of multi-paths that the system can resolve[7]. Denote a channel coefficient matrix for the TRDMA system as

$$\tilde{H} \triangleq \begin{bmatrix} \tilde{h}_{1,1} & \tilde{h}_{2,1} & \cdots & \tilde{h}_{M,1} \\ \tilde{h}_{1,2} & \tilde{h}_{2,2} & \cdots & \tilde{h}_{M,2} \\ \vdots & \vdots & \ddots & \vdots \\ \tilde{h}_{1,N} & \tilde{h}_{2,N} & \cdots & \tilde{h}_{M,N} \end{bmatrix}, \tag{4.33}$$

where $\tilde{h}_{m,n}$ is the channel coefficient for the m-th resolvable path of the channel response between the BS and the n-th user. Similarly, the maximum multiplexing order is given by $Rank(\tilde{H} = \min\{M, N\}$. To increase M, instead of adding more antennas (each of which demands a RF chain) in massive MIMO, the TRDMA system invests more bandwidth to leverage the large number of virtual antennas that naturally exist in rich-scattering environments. When spectrum is abundant, like in ultra-wide-band (UWB) system, TRDMA can potentially achieve similar performance gain as the massive MIMO, but with a much lower implementation cost.

4.3 Summary

In this chapter, we propose a TRDMA uplink scheme which efficiently reuses the higher processing power and the channel state information available at the BS,

[7]Roughly, this number is equal to the ratio of the channel delay spread T to the pulse duration T_P.

and keeps the complexity of the terminal users at a minimum level. The proposed TRDMA uplink scheme, together with the TRDMA downlink scheme, complements a unique asymmetric architecture that significantly reduce overall system cost of a TRDMA multi-user broadband network and improves its scalability.

Additionally, a comparative study between the TRDMA system and the massive MIMO system is conduced. It is shown that in essence the TRDMA system treats each path as a virtual antenna that naturally exists in the environment, and therefore is equivalent to a virtual massive MIMO system. Unlike the massive MIMO which demands a large number of RF chain, the proposed TRDMA system invest additional bandwidth to explore the multi-path in the environment with a much lower implementation cost, when the spectrum is abundant like in UWB systems.

Chapter 5: 2D Parallel Interference Cancellation for TRDMA System

From the discussion in Chapter 3 and Chapter 4, we have seen the unique advantages of the TRDMA system. In this chapter, we further enhance the system performance of the TRDMA system by proposing a 2-dimensional (2D) parallel interference cancellation scheme.

The proposed 2D parallel interference cancellation scheme explores the signal structure of both the inter-symbol interference (in time dimension) and the inter-user interference (IUI) (in user dimension). In principle, the proposed 2D parallel interference cancellation scheme can be applied to both the uplink and the downlink. However, considering the asymmetric architecture between the BS and the terminal users in terms of the processing power and available channel knowledge, such a scheme is more suitable to be performed at the BS for the TRDMA uplink[1]. Compared with the existing multi-user detection (MUD) techniques for CDMA systems [71–78], the interference cancellation for the TRDMA system is more challenging and desirable due to the following two facts: First, the multi-path

[1]The performance of the TRDMA downlink can be enhanced by the pre-coding schemes, i.e., by designing more sophisticated waveform than the basic TR-waveform as in [70].

signature waveforms are not naturally orthogonal, thus more severe IUI is expected in TRDMA than in CDMA system; Second, the TRDMA system allows overlap between the transmitted signature waveforms to boost system throughput, which will cause ISI depending on the extent of overlapping.

In this chapter, we propose a 2D parallel interference cancellation technique for the TRDMA uplink system. The proposed 2D parallel interference cancellation scheme utilizes the tentative decisions of detected symbols to effectively cancel both the ISI and IUI at the BS. To further improve the BER performance, a multi-stage processing can be performed by cascading multiple stages of the cancellation, with a total delay that increases linearly with the number of stages, but independent of the number of users. The BER performance of the single-stage cancellation is analyzed, and the approximated theoretical result is well consistent with simulation results. More simulations are provided for up-to 3 stages of interference cancellation and compared with the basic TRDMA system without interference cancellation.

5.1 System Model

Consider a multi-user TRDMA uplink system that consists of a BS and N users in the multi-path environment, as shown in Fig. 5.1. In Fig. 5.1, a new signal processing block that performs the proposed 2D parallel interference cancellation scheme is added to the basic TRDMA uplink system discussed in Chapter 4.

In this work, we assume that the Binary Phase-Shift Keying (BPSK) modulation is used, and thus the polarity of the modulated symbols $\{X_i[k] \in \{-1, +1\}\}$

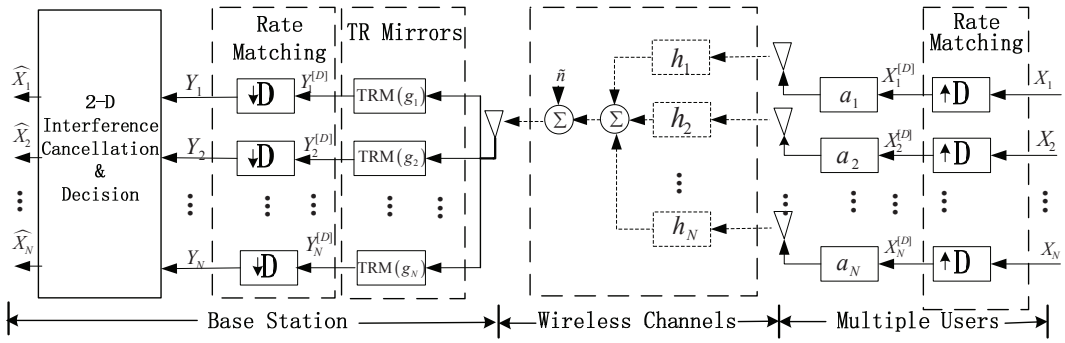

Figure 5.1: The diagram of TRDMA multiuser uplink system

carries the binary information for User i.

The basic TRDMA uplink scheme uses the signal $Y_i[k]$ in (4.7) to estimate the transmitted symbol $X_i[k]$. A very simple decision rule can be derived to implement the maximum-likelihood estimation (MLE) for the BPSK symbols $X_i[k] \in \{+1, -1\}$ for $i = 1, 2, \ldots, N$. By the central limit theorem, we model the total interference term (including the ISI and IUI) as a Gaussian random variable with zero mean[2] and variance

$$\sigma_{I,i}^2 = |a_i|^2 \sum_{\substack{l=-\lfloor \frac{L-1}{D} \rfloor \\ l\neq 0}}^{\lfloor \frac{L-1}{D} \rfloor} |(g_i * h_i)[L-1+Dl]|^2 + \sum_{\substack{j=1 \\ j\neq i}}^{N} |a_j|^2 \sum_{l=-\lfloor \frac{L-1}{D} \rfloor}^{\lfloor \frac{L-1}{D} \rfloor} |(g_i * h_j)[L-1+Dl]|^2 .$$

The likelihood ratio can be derived as

$$\Lambda(Y_i[k]) = \frac{\mathcal{L}(X_i[k]=1 \mid Y_i[k])}{\mathcal{L}(X_i[k]=-1 \mid Y_i[k])} = \frac{f_i[Y_i[k]|X_i[k]=1]}{f_i[Y_i[k]|X_i[k]=-1]} = \exp\left(\frac{2a_i(g_i * h_i)[L-1]}{(\sigma_{I,i}^2 + \sigma_{N,i}^2)} Y_i[k]\right) \tag{5.1}$$

where $f_i(y|x)$ is the conditional probability density function (pdf) of $Y_i[k]$ given that $X_i[k] = x$ is transmitted. The simple form of likelihood ratio shown in (5.1) leads

[2]because the interference term is a linear combination of the zero-mean binary symmetric symbols $X_i[k] \in \{+1, -1\}$.

to a simple decision rule for the MLE, specifically,

$$\hat{X}_i^{(0)}[k] = \mathrm{sgn}(Y_i[k]) = \begin{cases} +1, & \text{if } Y_i[k] \geqslant 0, \\ -1, & \text{if } Y_i[k] < 0. \end{cases} \tag{5.2}$$

In (5.2), the superscript "(0)" of $\hat{X}_i^{(0)}[k]$ indicates the initial stage of the interference cancellation procedure. Such a notation will be useful in the following discussion of multi-stage interference cancellation schemes.

The error probability of the estimator shown in (5.2) can be calculated based on the Gaussian approximations of the interference as follows

$$P_{err}^{(0)}(i) = Q\left(\sqrt{\frac{|a_i|^2 \sum_{l=0}^{L-1} |h_i[l]|^2}{\sigma_{I,i}^2 + \sigma_N^2}}\right) = Q\left(\sqrt{SINR_i^{(0)}}\right), \tag{5.3}$$

where the Q-function $Q(\cdot)$ is the tail probability of the standard normal distribution, and $SINR_i^{(0)}$ is the Signal-to-Interference-plus-Noise Ratio (SINR) for User i at the initial stage. From (5.3), one can see that the error probability decreases with the achieved SINR, i.e. the quality of the signal before the final decision.

In the following sections of this chapter, we discuss the 2D parallel interference cancellation scheme which uses the estimated symbols to effectively cancel both the ISI and IUI, and significantly improves the performance.

5.2 2-Dimensional Parallel Interference Cancellation

In this part, we describe the proposed 2D parallel interference cancellation scheme. We first introduce the single-stage scheme which serves as a building block of the more complicated multi-stage scheme, as will be introduced in the later part of this section.

The TRDMA system is an interference-limited system, especially in the high signal-to-noise ratio (SNR) regime. Fortunately, unlike the random noise, the interference terms shown in (4.8) have their own structure, which can be explored to further improve the bit error rate (BER) performances. Since the channel responses have been obtained at the BS during the channel probing phase[3], the interference terms in (4.8) can be reconstructed if the relevant transmitted symbols are known. In the proposed interference cancellation scheme, the estimated symbols from the previous stage[4] are used to approximate the interference terms in the current stage. Unlike the existing multiuser detection scheme in CDMA systems, the interference cancellation of the TRDMA system is complicated by the fact that the interference consists of two parts belonging to two different dimensions: the ISI is due to the multi-path effect of broadband channels, which is in the time domain; the IUI is caused by the simultaneous transmission of multiple users, which is in the user's signature domain. The proposed 2D parallel interference cancellation scheme for the TRDMA uplink system targets at the interference in both of the two dimensions, by exploiting the structure of interference in both dimensions.

5.2.1 Tentative Decision Vector

Due to the unique structure of TR waveform, each received symbol suffers from the interference caused by those symbols transmitted before and after this

[3]Note that the coefficients $\{a_i\}$ are in fact determined by the BS and sent to users.

[4]The basic TRDMA system is considered as the initial (0-th) stage of the interference cancellation

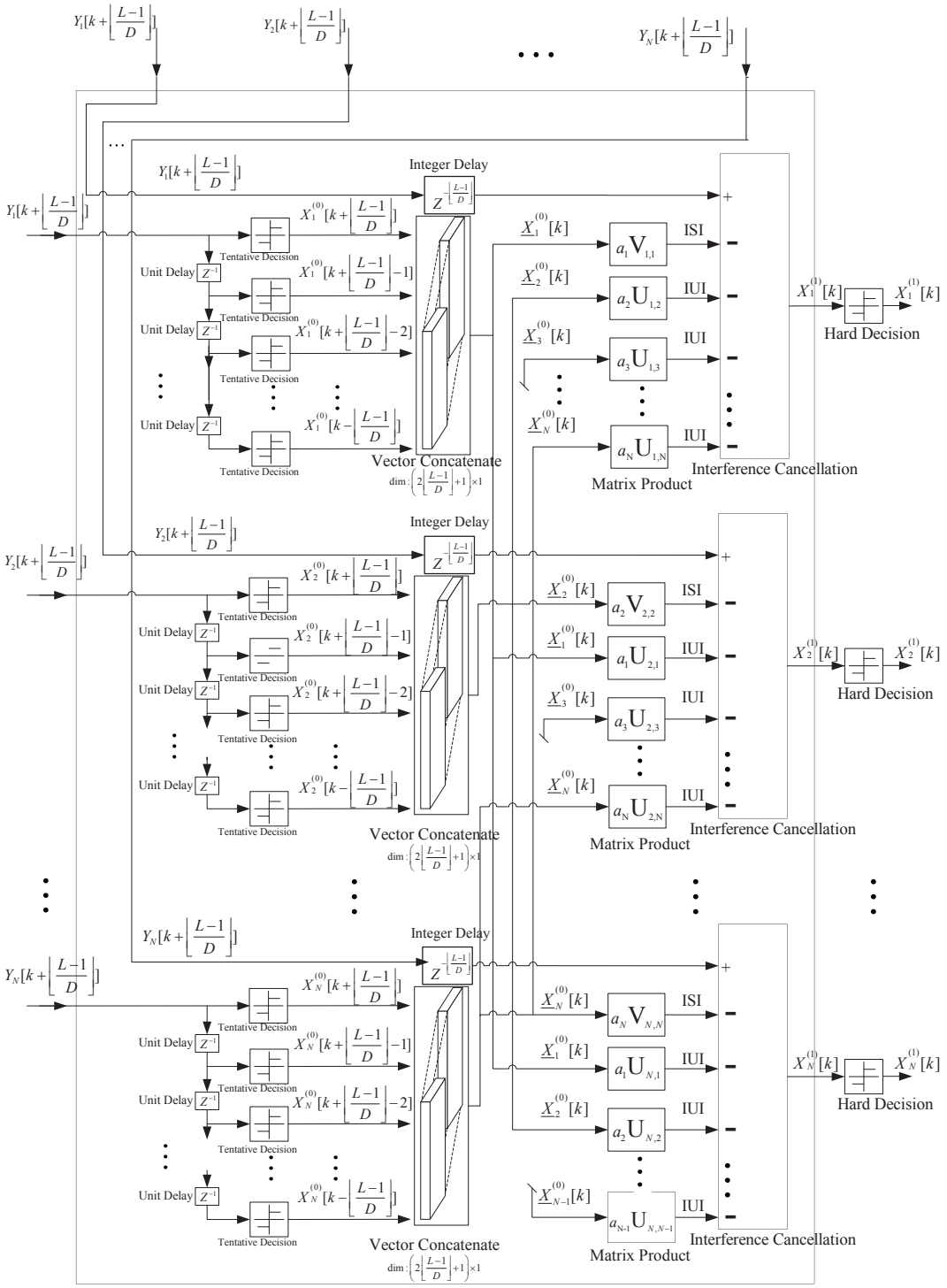

Figure 5.2: The diagram of the Single-Stage 2D Parallel Interference Cancellation.

symbol. According to (4.8), in order to ideally cancel the interference for User i's symbol $X_i[k]$, one has to know all the other users' transmitted symbols from time $\left(k - \lfloor \frac{L-1}{D} \rfloor\right)$ to $\left(k + \lfloor \frac{L-1}{D} \rfloor\right)$ for the IUI, i.e.

$$\left[X_j[k + \lfloor \frac{L-1}{D} \rfloor], X_j[k + \lfloor \frac{L-1}{D} \rfloor - 1], \ \ldots \ , X_j[k - \lfloor \frac{L-1}{D} \rfloor]\right], \text{for } j \neq i;$$

and User i's own transmitted symbols from time $\left(k - \lfloor \frac{L-1}{D} \rfloor\right)$ to $(k-1)$ and from $(k+1)$ to $\left(k + \lfloor \frac{L-1}{D} \rfloor\right)$ for the ISI, i.e.,

$$\left[X_i[k+\lfloor \frac{L-1}{D} \rfloor], X_i[k+\lfloor \frac{L-1}{D} \rfloor - 1], \ \ldots \ , X_i[k-1], X_i[k+1], \ldots, X_i[k-\lfloor \frac{L-1}{D} \rfloor]\right].$$

In reality, tentative decisions are made in attempt to estimate these symbols. To simplify the notation in the sequel, define the vector $\underline{\hat{X}}_j^{(0)}[k]$ for all $j \in \{1, 2, \ldots, N\}$, as the stage-0 tentative decision vector for User j, where

$$\begin{aligned} \underline{\hat{X}}_j^{(0)}[k] &\triangleq \left[\hat{X}_j^{(0)}[k + \lfloor \frac{L-1}{D} \rfloor], \hat{X}_j^{(0)}[k + \lfloor \frac{L-1}{D} \rfloor - 1], \ \ldots \ , \hat{X}_j^{(0)}[k - \lfloor \frac{L-1}{D} \rfloor]\right]^T \\ &= \left[\text{sgn}\left(Y_j[k+\lfloor \frac{L-1}{D} \rfloor]\right), \text{sgn}\left(Y_j[k+\lfloor \frac{L-1}{D} \rfloor - 1]\right), \ldots, \text{sgn}\left(Y_j[k-\lfloor \frac{L-1}{D} \rfloor]\right)\right]^T. \end{aligned} \tag{5.4}$$

Since the stage-0 tentative decisions for User j solely depend on this user's own TRM output, the tentative decision vectors can be obtained in parallel for all the users in the propose 2D parallel interference cancellation scheme.

5.2.2 Approximated Interference Reconstruction

Based on the tentative decisions of the transmitted symbols, the approximated interference terms in (4.8) can be reconstructed by looking at the structure of the

ISI and IUI. In doing so, we first define the row vector $\mathbf{U}_{i,j}$ for $\forall i, j \in \{1, 2, \ldots, N\}$ as

$$\mathbf{U}_{i,j} \triangleq \Big[(g_i * h_j)\big[L-1-D\lfloor\frac{L-1}{D}\rfloor\big], (g_i * h_j)\big[L-1-D\left(\lfloor\frac{L-1}{D}\rfloor-1\right)\big], \cdots, (g_i * h_j)\big[L-1+D\lfloor\frac{L-1}{D}\rfloor\big]\Big], \tag{5.5}$$

so that the ISI canceler vector and the IUI canceler vector can be easily represented as follows:

- ISI Canceler Vector: Considering the ISI to $X_i[k]$ as a linear combination of User i's own symbols, define the ISI canceler vector $\mathbf{V}_{i,i}$ for User i to be

$$\mathbf{V}_{i,i} \triangleq \mathbf{U}_{i,i}\mathcal{D}\left(\underline{\mathbf{1}}, 0, \underline{\mathbf{1}}\right), \tag{5.6}$$

  where $\mathcal{D}(\underline{z})$ is a diagonal matrix whose diagonal elements are listed by $\underline{z}$, and $\underline{\mathbf{1}} \triangleq \{1, 1, \ldots, 1\}$ of length $\lfloor\frac{L-1}{D}\rfloor$. As a result, the approximated ISI term for User i's symbol $X_i[k]$ can be written in a compact form as the product of the ISI canceler vector $\mathbf{V}_{i,i}$ and the tentative decision vector $\underline{\hat{X}}_i^{(0)}[k]$ shown as follows

$$ISI = a_i \sum_{\substack{l=-\lfloor\frac{L-1}{D}\rfloor \\ l\neq 0}}^{\lfloor\frac{L-1}{D}\rfloor} (g_i * h_i)\left[L-1+Dl\right]\hat{X}_j[k-l] = a_i\mathbf{V}_{i,i}\underline{\hat{X}}_i^{(0)}[k]. \tag{5.7}$$

- IUI Canceler Vector: Similarly, we define the IUI canceler vector for the IUI caused by User j to User i as $\mathbf{U}_{i,j}$, so that the estimated IUI term to be canceled for User i's symbol $X_i[k]$ can be obtained as

$$IUI = \sum_{\substack{j=1 \\ j\neq i}}^{N} a_j \sum_{l=-\lfloor\frac{L-1}{D}\rfloor}^{\lfloor\frac{L-1}{D}\rfloor} (g_i * h_j)\left[L-1+Dl\right]\hat{X}_j[k-l] = \sum_{\substack{j=1 \\ j\neq i}}^{N} a_j\mathbf{U}_{i,j}\underline{\hat{X}}_j^{(0)}[k]. \tag{5.8}$$

5.2.3 Single-stage 2D Interference Cancellation

The single-stage 2D parallel interference cancellation scheme is shown in Fig. 5.2. From Fig. 5.2, one can see that the input signals for all the N users are first buffered by delay chains of length $2\lfloor\frac{L-1}{D}\rfloor$. Then tentative hard decisions are made in parallel for each user to obtain the vector $\underline{\hat{X}}_i^{(0)}[k]$ for $\forall i \in \{1, 2, \ldots, N\}$ using the decision rule (5.2). Upon obtaining the tentative decision vectors $\underline{\hat{X}}_i^{(0)}[k]$ for all $i \in \{1, 2, \ldots, N\}$, the interference terms are reconstructed and then subtracted from the signal $Y_i[k]$ with the ISI and IUI canceler vectors.

Similar to the definition in (5.4), denoting

$$\underline{X}_j[k] \triangleq \left[X_j[k + \lfloor\frac{L-1}{D}\rfloor], X_j[k + \lfloor\frac{L-1}{D}\rfloor - 1], \ \ldots \ , X_j[k - \lfloor\frac{L-1}{D}\rfloor]\right]^T, \quad (5.9)$$

we can rewrite (4.8) in a more compact form as

$$Y_i[k] = a_i\sqrt{\sum_{l=0}^{L-1}|h_i[l]|^2}X_i[k] + a_i\mathbf{V}_{i,i}\underline{X}_i[k] + \sum_{\substack{j=1\\j\neq i}}^{N} a_j\mathbf{U}_{i,j}\underline{X}_j[k] + n_i[k]. \quad (5.10)$$

After the interference cancellation, the resulting soft-bit $\tilde{X}_i^{(1)}[k]$ can be written as

$$\tilde{X}_i^{(1)}[k] = a_i\sqrt{\sum_{l=0}^{L-1}|h_i[l]|^2}X_i[k] + a_i\mathbf{V}_{i,i}\left(\underline{X}_i[k] - \underline{\hat{X}}_i^{(0)}[k]\right) + \sum_{\substack{j=1\\j\neq i}}^{N} a_j\mathbf{U}_{i,j}\left(\underline{X}_j[k] - \underline{\hat{X}}_j^{(0)}[k]\right) + n[k]. \quad (5.11)$$

A hard decision $\hat{X}_i^{(1)}[k] = \text{sgn}\left(\tilde{X}_i^{(1)}[k]\right)$ can be made based on $\tilde{X}_i^{(1)}[k]$ to achieve a more refined estimation for the transmitted symbol.

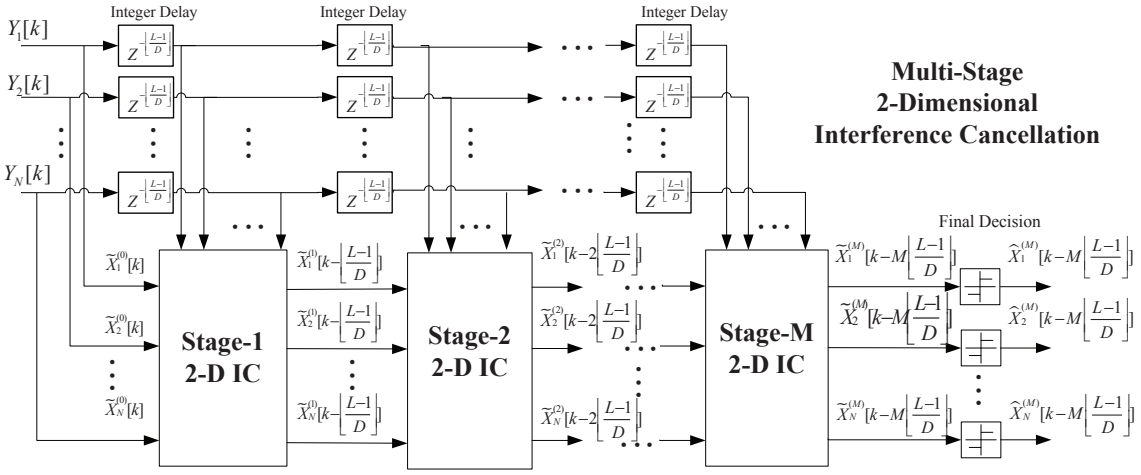

Figure 5.3: The diagram of the M-Stage 2D Parallel Interference Cancellation.

5.2.4 The Multi-stage Iterative Scheme

To further improve the detection performance, a multi-stage processing can be performed by cascading multiple stages of the proposed 2D parallel interference cancellation. In this part, we generalize the basic single-stage scheme into an iterative multi-stage scheme, in which the signal quality is refined after each stage of interference cancellation[5].

Fig. 5.3 shows the diagram of an M-stage interference cancellation scheme. Basically, as the procedures proceed, in each stage, the same 2D parallel interference cancellation is performed in attempt to remove both the ISI and IUI with the updated estimates of the transmitted symbols. Each stage takes the soft-bits from the previous stage as the input, based on which tentative decisions are made to estimate the interference and generate the soft-bits of the current stage as the output.

More specifically, in the context of multiple stages, the m-th stage's operation

[5]when the BER performance of the initial stage is not too high.

can be described as follows:

- Delay and Buffering: The soft-bits from the previous stage (the $(m-1)$-th stage) are delayed and buffered to form a soft-bit vector for each user, such that for all $i \in \{1, 2, \ldots, N\}$,

$$\underline{\tilde{X}}_i^{(m-1)}\Big[k - m\lfloor\frac{L-1}{D}\rfloor\Big] \triangleq \begin{bmatrix} \tilde{X}_i^{(m-1)}\big[k-(m-1)\lfloor\frac{L-1}{D}\rfloor\big] \\ \tilde{X}_i^{(m-1)}\big[k-(m-1)\lfloor\frac{L-1}{D}\rfloor-1\big] \\ \vdots \\ \tilde{X}_i^{(m-1)}\big[k-(m+1)\lfloor\frac{L-1}{D}\rfloor\big] \end{bmatrix} \tag{5.12}$$

- Tentative Decision: The tentative decisions are made based on the soft-bits from the previous stage (the $(m-1)$-th stage) in attempt to estimate the transmitted symbols, i.e., for all $i \in \{1, 2, \ldots, N\}$,

$$\underline{\hat{X}}_i^{(m-1)}[k - m\lfloor\frac{L-1}{D}\rfloor] = \operatorname{sgn}\left(\underline{\tilde{X}}_i^{(m-1)}[k - m\lfloor\frac{L-1}{D}\rfloor]\right). \tag{5.13}$$

- Interference Cancellation: The soft-bits of the current stage (the m-th stage) are generated by subtracting the estimated interference terms from the original signals $\{Y_i\}$. The soft-bit of User i generated by the m-th stage is given by

$$\begin{aligned}\tilde{X}_i^{(m)}[k - m\lfloor\frac{L-1}{D}\rfloor] =& Y_i[k - m\lfloor\frac{L-1}{D}\rfloor] - a_i\mathbf{V}_{i,i}\underline{\hat{X}}_i^{(m-1)}[k - m\lfloor\frac{L-1}{D}\rfloor] \\ &- \sum_{\substack{j=1 \\ j\neq i}}^{N} a_j\mathbf{U}_{i,j}\underline{\hat{X}}_j^{(m-1)}[k - m\lfloor\frac{L-1}{D}\rfloor]\end{aligned} \tag{5.14}$$

In particular, such an M-stage scheme is initialized by setting the soft-bits of the initial stage (the 0-th stage) as

$$\tilde{X}_1^{(0)}[k] = Y_1[k],\ \tilde{X}_2^{(0)}[k] = Y_2[k],\ \ldots,\ \tilde{X}_N^{(0)}[k] = Y_N[k]. \tag{5.15}$$

After the signal flows through all the M stages, the final decision is made for each user based on the output of the Stage-M interference cancellation,

$$\hat{X}_i^{(M)}[k - M\lfloor\frac{L-1}{D}\rfloor] = \text{sgn}\left(\tilde{X}_i^{(M)}[k - M\lfloor\frac{L-1}{D}\rfloor]\right), \ for\ all\ i \in \{1, 2, \ldots, N\}. \tag{5.16}$$

Comparing the timing of the estimated symbols after the final decision $\hat{X}_i^{(M)}[k - M\lfloor\frac{L-1}{D}\rfloor]$ and the original TRM output signal $Y_i[k]$, one can see that each stage incurs a delay of $\lfloor\frac{L-1}{D}\rfloor$. Therefore, the total detection delay grows linearly with the number of stages, but is independent of the number of users. When it comes to the complexity, the complexity of the proposed 2D parallel interference cancellation increases linearly with the number of users, as opposed to many other joint detection schemes whose complexity grows exponentially with the number of users.

5.3 Performance Analysis of The Single-stage Interference Cancellation

In this section, we analyze the estimation performance of the proposed 2-dimensional interference cancellation scheme, assuming that BPSK symbols are transmitted. As one will see, the performance analysis associated with this scheme is complicated by the fact that the tentative decisions are highly correlated in both time domain and user's signature domain, rather than being independent of one another. In the following part, we focus on the single-stage 2D interference cancellation and analyze the resulting BER performance.

The theoretical analysis of the estimation error probability of the multi-stage

2D parallel interference cancellation scheme can be very difficult, due to the nonlinearity of the tentative decision and complicated correlation of the combined signals after multi-stage interference cancellation. We will use simulations to evaluate the BER performance of the multi-stage scheme.

5.3.1 Statistical Model on the BER Performance

In the proposed 2D parallel interference cancellation scheme, tentative decisions $\{\hat{X}_i^{(0)}[k]\}$ based on the TRM output $\{Y_i[k]\}$ are used to cancel the ISI and IUI in the first stage. The resulting soft-bit of User i can be represented as follows:

$$\tilde{X}_i^{(1)}[k] = a_i \sqrt{\sum_{l=0}^{L-1} |h_i[l]|^2} X_i[k] + a_i \mathbf{V}_{i,i} \left(\underline{X}_i[k] - \underline{\hat{X}}_i^{(0)}[k] \right) + \sum_{\substack{j=1 \\ j \neq i}}^{N} a_j \mathbf{U}_{i,j} \left(\underline{X}_j[k] - \underline{\hat{X}}_j^{(0)}[k] \right) + n_i[k]. \tag{5.17}$$

A hard decision (5.2) is made on $\tilde{X}_i^{(1)}[k]$ i.e. $\hat{X}_i^{(1)}[k] = \text{sgn}\left(\tilde{X}_i^{(1)}[k]\right)$. To calculate the error probability $Pr\left[\hat{X}_i^{(1)}[k] \neq X_i[k]\right]$, one needs a statistical model to characterize the total interference in (5.17). Although the BPSK symbols $\{X_i\}$ for all $i \in \{1, 2, \ldots, N\}$ are i.i.d. and follow a very simple Bernoulli distribution, the exact distribution of the interference is much more complicated due to the large numbers of L (the length the multi-path channels) and N (the number of users). On the other hand, however, for sufficiently large L and N, it is reasonable to assume a Gaussian model for the remaining (after the cancellation) ISI and IUI.

Assuming then a Gaussian model for both the (remaining) ISI and IUI, the error probability for the single-stage cancellation is given by $P_{err}^{(1)}(i) = Q\left(\sqrt{SINR_i^{(1)}}\right)$,

where

$$SINR_i^{(1)} = \frac{|a_i|^2 \sum_{l=0}^{L-1} |h_i[l]|^2}{P_{ISI}^{(1)}(i) + P_{IUI}^{(1)}(i) + \sigma_{N,i}^2}. \tag{5.18}$$

To calculate the residual ISI power $P_{ISI}^{(1)}(i)$ and IUI power $P_{IUI}^{(1)}(i)$ in (5.18), we first define the error correlation matrix $R_{j,w}^{(0)}$ for $\forall j, w \in \{1, 2, \ldots, N\}$ which will help simplify the notation in the following discussion:

$$\begin{aligned} R_{j,w}^{(0)} &\triangleq E\left[\left(\underline{X}_j[k] - \underline{\hat{X}}_j^{(0)}[k]\right)\left(\underline{X}_w[k] - \underline{\hat{X}}_w^{(0)}[k]\right)^T\right] \\ &= E\left[\underline{X}_j[k]\underline{X}_w^T[k]\right] - E\left[\underline{X}_j[k]\underline{\hat{X}}_w^{(0)T}[k]\right] - \left(E\left[\underline{X}_w[k]\underline{\hat{X}}_j^{(0)T}[k]\right]\right)^T + E\left[\underline{\hat{X}}_j^{(0)}[k]\underline{\hat{X}}_w^{(0)T}[k]\right] \end{aligned} \tag{5.19}$$

Consequently, the ISI power for User i after the first stage interference cancellation can be written as

$$P_{ISI}^{(1)}(i) = a_i^2 E\left[\mathbf{V}_{i,i}\left(\underline{X}_i[k] - \underline{\hat{X}}_i^{(0)}[k]\right)\left(\underline{X}_i[k] - \underline{\hat{X}}_i^{(0)}[k]\right)^T \mathbf{V}_{i,i}^T\right] = a_i^2 \mathbf{V}_{i,i} R_{i,i}^{(0)} \mathbf{V}_{i,i}^T, \tag{5.20}$$

Similarly, the remaining IUI for User i can be represented as

$$\begin{aligned} P_{IUI}^{(1)}(i) &= \sum_{\substack{j=1 \\ j\neq i}}^{N} \sum_{\substack{w=1 \\ w\neq i}}^{N} E\left[a_j a_w \mathbf{U}_{i,j}\left(\underline{X}_j[k] - \underline{\hat{X}}_j^{(0)}[k]\right)\left(\underline{X}_w[k] - \underline{\hat{X}}_w^{(0)}[k]\right)^T \mathbf{U}_{i,w}^T\right] \\ &= \sum_{\substack{j=1 \\ j\neq i}}^{N} \sum_{\substack{w=1 \\ w\neq i}}^{N} a_j a_w \mathbf{U}_{i,j} R_{j,w}^{(0)} \mathbf{U}_{i,w}^T \end{aligned} \tag{5.21}$$

With (5.20) and (5.21), the calculation of the interference power for User i reduces to calculate the error correlation matrix $R_{j,w}^{(0)}$, which will be addressed in the remaining part of this section.

5.3.2 The Error Correlation Matrix

The error correlation matrix $R_{j,w}^{(0)}$ defined in (5.19) consists of four different correlation matrices, which altogether characterize the correlation between the estimation errors of User j and User w. Exact calculation of these correlation matrices can be very difficult, we approximate them using various techniques, more detailed in the following discussion.

Since the BPSK symbols are i.i.d. Bernoulli random variables over $\{-1, +1\}$, the first term $E\left[\underline{X}_j[k]\underline{X}_w^T[k]\right]$ (the data correlation matrix) in (5.19) can be calculated very easily, i.e.,

$$E\left[\underline{X}_j[k]\underline{X}_w^T[k]\right] = \begin{cases} \mathbf{I}, & \text{if } \ j = w, \\ \underline{\mathbf{0}}, & \text{if } \ j \neq w. \end{cases} \tag{5.22}$$

where $\mathbf{I}$ and $\underline{\mathbf{0}}$ are the identity matrix and the zero matrix of size $\left(2\lfloor\frac{L-1}{D}\rfloor + 1\right)$-by-$\left(2\lfloor\frac{L-1}{D}\rfloor + 1\right)$, respectively.

5.3.2.1 The Cross Correlation Matrix

In this part, we study the cross correlation matrix $E\left[\underline{X}_j[k]\hat{\underline{X}}_w^{(0)T}[k]\right]$. Define $M_{j,w}^{(0)} \triangleq E\left[\underline{X}_j[k]\hat{\underline{X}}_w^{(0)T}[k]\right]$, for $\forall w, j \in \{1, 2, \ldots, N\}$. Note that the element at the m-th row and n-th column of the matrix $M_{j,w}^{(0)}$ has the following form[6]

$$\left(M_{j,w}^{(0)}\right)_{(m,n)} = E\left[X_j[k]\hat{X}_w^{(0)}[k+m-n]\right]. \tag{5.23}$$

[6]Note that for the value of any element $\left(M_{j,w}^{(0)}\right)_{(m,n)}$ is a function of $m-n$, independent of the specific value of k.

In (5.23), denoting $\tau = m - n$, it holds that when $\left|\tau\right| > \lfloor\frac{L-1}{D}\rfloor$, $X_j[k]$ and $\hat{X}_w^{(0)}[k+\tau] = \operatorname{sgn}\left(Y_w[k+\tau]\right)$ are independent (as can be seen in (4.7)) and therefore

$$\left(M_{j,w}^{(0)}\right)_{(m,n)} = E\left[X_j[k]\hat{X}_j^{(0)}[k+\tau]\right] = 0.$$

For any given number $\tau \in \left\{\tau \in \mathbb{Z} \;\middle|\; |\tau| \leqslant \lfloor\frac{L-1}{D}\rfloor\right\}$, we have,

$$\begin{aligned}
\left(M_{j,w}^{(0)}\right)_{(m,n)} =& E\left[X_j[k]\hat{X}_w^{(0)}[k+\tau]\right] \\
=& \frac{1}{2}\left[E\big[\hat{X}_w^{(0)}[k+\tau] \;\big|\; X_j[k]=1\big] - E\big[\hat{X}_w^{(0)}[k+\tau] \;\big|\; X_j[k]=-1\big]\right] \\
=& \frac{1}{2}\Big[\Pr\big[Y_w[k+\tau] \geqslant 0 \;\big|\; X_j[k]=1\big] - \Pr\big[Y_w[k+\tau] < 0 \;\big|\; X_j[k]=1\big]\Big] - \\
& \frac{1}{2}\Big[\Pr\big[Y_w[k+\tau] \geqslant 0 \;\big|\; X_j[k]=-1\big] - \Pr\big[Y_w[k+\tau] < 0 \;\big|\; X_j[k]=-1\big]\Big]
\end{aligned} \tag{5.24}$$

According to (4.7), for $-\lfloor\frac{L-1}{D}\rfloor \leqslant \tau \leqslant \lfloor\frac{L-1}{D}\rfloor$, the signal $Y_w[k+\tau] - a_j\left(g_w * h_j\right)[L-1+D\tau]X_j[k]$ is independent of $X_j[k]$. We define $\Psi_{j,w}[\tau] \triangleq Y_w[k+\tau] - a_j\left(g_w * h_j\right)[L-1+D\tau]X_j[k]$, which is a linear combination of a large number of independent variables. By central limit theorem, we approximate $\Psi_{j,w}[\tau]$ as a Gaussian random variable with zero mean and the variance shown as follows

$$\sigma^2_{\Psi_{j,w}[\tau]} = \sigma_N^2 + \sum_{v=1}^{N} a_v^2 \mathbf{U}_{w,v}\mathbf{U}_{w,v}^T - a_j^2\Big|\left(g_w * h_j\right)[L-1+D\tau]\Big|^2 \tag{5.25}$$

Consequently, (5.24) can be further calculated as

$$
\begin{aligned}
&E\left[X_j[k]\hat{X}_w^{(0)}[k+\tau]\right] \\
=&\frac{1}{2}\Big[\Pr\big[\Psi_{j,w}[\tau]\geqslant -a_j\left(g_w * h_j\right)[L-1+D\tau]\big]-\Pr\big[\Psi_{j,w}[\tau]<-a_j\left(g_w * h_j\right)[L-1+D\tau]\big]\Big] \\
-&\frac{1}{2}\Big[\Pr\big[\Psi_{j,w}[\tau]\geqslant a_j\left(g_w * h_j\right)[L-1+D\tau]\big]-\Pr\big[\Psi_{j,w}[\tau]<a_j\left(g_w * h_j\right)[L-1+D\tau]\big]\Big] \\
=&\mathrm{sgn}\Big(a_j\left(g_w * h_j\right)[L-1+D\tau]\Big)Pr\Big[\big|\Psi_{j,w}[\tau]\big|\leqslant\big|a_j\left(g_w * h_j\right)[L-1+D\tau]\big|\Big] \\
\approx&\mathrm{sgn}\Big(a_j\left(g_w * h_j\right)[L-1+D\tau]\Big)\left(1-2Q\left(\frac{\big|a_j\left(g_w * h_j\right)[L-1+D\tau]\big|}{\sigma_{\Psi_{j,w}[\tau]}}\right)\right)
\end{aligned}
\tag{5.26}
$$

5.3.2.2 The Estimation Correlation Matrix

In this part, we study the estimation correlation matrix $E\left[\underline{\hat{X}}_j^{(0)}[k]\underline{\hat{X}}_w^{(0)T}[k]\right]$. Define $C_{j,w}^{(0)} \triangleq E\big[\underline{\hat{X}}_j^{(0)}[k]\underline{\hat{X}}_w^{(0)T}[k]\big]$, for $\forall j,w \in 1,2,\ldots,N$. Denoting $\tau = m-n$, the element on the m-th row and n-th column of the matrix $\left(C_{j,w}^{(0)}\right)$ can be then represented as follows:

$$
\begin{aligned}
\left(C_{j,w}^{(0)}\right)_{m,n} &= E\Big[\mathrm{sgn}\big(Y_j[k]Y_w[k+\tau]\big)\Big] \\
&= Pr\Big[Y_j[k]Y_w[k+\tau]\geqslant 0\Big]-Pr\Big[Y_j[k]Y_w[k+\tau]<0\Big] \\
&= 2Pr\Big[Y_j[k]Y_w[k+\tau]\geqslant 0\Big]-1.
\end{aligned}
\tag{5.27}
$$

To approximate the probability $Pr\Big[Y_j[k]Y_w[k+\tau]\geqslant 0\Big]$, we model $(Y_j[k], Y_w[k+\tau])$ as bivariate Gaussian random variables, following the multidimensional central limit theorem [79]. It is easy to show that both $Y_j[k]$ and $Y_w[k+\tau]$ have zero mean, i.e.

$$
E\left[Y_j[k]\right] = E\left[Y_w[k+\tau]\right] = 0. \tag{5.28}
$$

The covariance matrix $\Sigma = \begin{pmatrix} \sigma_1^2 & \rho_{j,w}(\tau)\sigma_1\sigma_2 \\ \rho_{j,w}(\tau)\sigma_1\sigma_2 & \sigma_2^2 \end{pmatrix}$ can be given by the fol-

lowing:

$$\sigma_1^2 = E\left[Y_j^2[k]\right] = \sum_{d=1}^{N} a_d^2 \mathbf{U}_{j,d}\mathbf{U}_{j,d}^T + \sigma_N^2; \tag{5.29}$$

$$\sigma_2^2 = E\left[Y_w^2[k+\tau]\right] = \sum_{d=1}^{N} a_d^2 \mathbf{U}_{w,d}\mathbf{U}_{w,d}^T + \sigma_N^2; \tag{5.30}$$

and

$$\rho_{j,w}(\tau) = \frac{E\Big[Y_j[k]Y_w[k+\tau]\Big]}{\sigma_1\sigma_2}, \tag{5.31}$$

where

$$\begin{aligned}
&E\Big[Y_j[k]Y_w[k+\tau]\Big] \\
=&E\Big[\big(\sum_{d=1}^{N} a_d \mathbf{U}_{j,d}\underline{X}_d[k] + n_j[k]\big)\big(\sum_{d=1}^{N} a_v \mathbf{U}_{w,v}\underline{X}_v[k+\tau] + n_w[k+\tau]\big)\Big] \\
=&\sum_{d=1}^{N}\sum_{v=1}^{N} a_d a_v \mathbf{U}_{j,d} E\Big[\underline{X}_d[k]\underline{X}_v^T[k+\tau]\Big]\mathbf{U}_{w,v}^T + E\Big[n_j[k]n_w[k+\tau]\Big] \\
=&\sum_{d=1}^{N} a_d^2 \mathbf{U}_{j,d} E\Big[\underline{X}_d[k]\underline{X}_d^T[k+\tau]\Big]\mathbf{U}_{w,d}^T + \underline{g}_j E\Big[\underline{\tilde{n}}[Dk]\underline{\tilde{n}}^T[D(k+\tau)]\Big]\underline{g}_w^T
\end{aligned} \tag{5.32}$$

In (5.32), the expectation $\Lambda[\tau] \triangleq E\Big[\underline{X}_d[k]\underline{X}_d^T[k+\tau]\Big]$ is a $\big(2\lfloor\frac{L-1}{D}\rfloor+1\big)$-by-$\big(2\lfloor\frac{L-1}{D}\rfloor+1\big)$ square Toeplitz matrix with its elements determined by $(\Lambda[\tau])_{p,q} = \lambda_{q-p}$, where the value of λ_{q-p} is given as follows:

$$\lambda_{q-p} = \begin{cases} 1, & \text{if } \ q-p=\tau, \\ 0, & \text{if } \ q-p\neq\tau. \end{cases} \tag{5.33}$$

Thanks to the special structure of $\Lambda[\tau]$, the value of $\mathbf{U}_{j,d}\left(\Lambda[\tau]\right)\mathbf{U}_{w,d}^T$ can be

represented by a simple function $\Pi\left(\mathbf{U}_{j,d}, \mathbf{U}_{w,d}, \tau\right)$ defined as follows:

$$\mathbf{U}_{j,d}\left(\Lambda[\tau]\right)\mathbf{U}_{w,d}^{T} = \Pi\left(\mathbf{U}_{j,d}, \mathbf{U}_{w,d}, \tau\right) \triangleq \begin{cases} \mathbf{U}_{j,d}\mathbf{U}_{w,d}^{T}, & \text{if } \tau = 0, \\ \sum_{l=1}^{\dim\left(\mathbf{U}_{w,d}\right)-|\tau|} u_{j,d}(l)u_{w,d}(l+|\tau|) & \text{if } \tau > 0, \\ \sum_{l=1}^{\dim\left(\mathbf{U}_{j,d}\right)-|\tau|} u_{j,d}(l+|\tau|)u_{w,d}(l) & \text{if } \tau < 0, \end{cases} \tag{5.34}$$

where $\dim(\cdot)$ equals to the dimensionality of the operand vector.

For the second term $\underline{g}_j E\Big[\underline{\tilde{n}}[Dk]\underline{\tilde{n}}^T[D(k+\tau)]\Big]\underline{g}_w^T$ in (5.32), one could have a similar expression using the definition of the function Π in (5.34)

$$\underline{g}_j E\Big[\underline{\tilde{n}}[Dk]\underline{\tilde{n}}^T[D(k+\tau)]\Big]\underline{g}_w^T = \begin{cases} \sigma_N^2 \Pi\left(\underline{g}_j, \underline{g}_w, D\tau\right), & \text{if} \quad |\tau| \leqslant \lfloor\frac{L-1}{D}\rfloor, \\ 0 & \text{if} \quad |\tau| > \lfloor\frac{L-1}{D}\rfloor. \end{cases} \tag{5.35}$$

Combining the results of (5.34) and (5.35), the cross correlation between $Y_j[k]$ and $Y_w[k+\tau]$ is given by

$$E\Big[Y_j[k]Y_w[k+\tau]\Big] = \begin{cases} \sigma_N^2 \Pi\left(\underline{g}_j, \underline{g}_w, D\tau\right) + \sum_{d=1}^{N} a_d^2 \Pi\left(\mathbf{U}_{j,d}, \mathbf{U}_{w,d}, \tau\right), & \text{if } |\tau| \leqslant \lfloor\frac{L-1}{D}\rfloor, \\ \sum_{d=1}^{N} a_d^2 \Pi\left(\mathbf{U}_{j,d}, \mathbf{U}_{w,d}, \tau\right), & \text{if } |\tau| > \lfloor\frac{L-1}{D}\rfloor. \end{cases} \tag{5.36}$$

which can be substituted into (5.31) to obtain the value of $\rho_{j,w}(\tau)$.

Upon obtaining the probability distribution of $(Y_j[k], Y_w[k+\tau])$ by assuming a bivariate normal distribution model, the quadrant probability is readily and analytically given by [80]

$$Pr\Big[Y_j[k] \geqslant 0, Y_w[k+\tau] \geqslant 0\Big] = Pr\Big[Y_j[k] \leqslant 0, Y_w[k+\tau] \leqslant 0\Big] = \frac{1}{4} + \frac{\arcsin\left(\rho_{j,w}(\tau)\right)}{2\pi}. \tag{5.37}$$

Therefore, for any element $\left(C_{j,w}^{(0)}\right)_{m,n}$ in the matrix $\left(C_{j,w}^{(0)}\right)$, it holds that

$$\left(C_{j,w}^{(0)}\right)_{m,n} = 2Pr\Big[Y_j[k]Y_w[k+\tau] \geqslant 0\Big] - 1 = \frac{2}{\pi}\arcsin\left(\rho_{j,w}(\tau)\right). \tag{5.38}$$

To summarize, we have derived an analytical approximation for each of the four components of the error correlation matrix in (5.19). Therefore, for any given $j, w \in \{1, 2, \ldots, N\}$, it holds that

$$R_{j,w}^{(0)} \approx \begin{cases} \mathbf{I} - M_{j,j}^{(0)} - \left(M_{j,j}^{(0)}\right)^T + C_{j,j}^{(0)} & \text{if } \ j = w, \\ -M_{j,w}^{(0)} - \left(M_{w,j}^{(0)}\right)^T + C_{j,w}^{(0)} & \text{if } \ j \neq w, \end{cases} \tag{5.39}$$

so that both the residual ISI power (5.20) and IUI power (5.21) can be calculated using (5.39). Then for any given user of interest (for instance, User i), the post-cancellation SINR $SINR_i^{(0)}$ (5.18) can be obtained to compute its BER performance.

5.4 Simulation Results

In this section, we present some simulation results on the BER performance of the proposed 2D parallel interference cancellation scheme. To study the proposed scheme in a more realistic setting, we used the more practical IEEE 802.15.4a outdoor non-line-of-sight (NLOS) channel model[7] [81] to evaluate the BER performance of the proposed scheme.

Fig. 5.4 shows an example of two typical channel impulse responses under such a channel model and their convolutions with the TR signature waveforms. The channels shown in Fig. 5.4 are randomly generated according to the channel model specified in [81], with the system sampling period $T_s = 1$ ns and the channel length

[7] In such a channel model, each channel tap is a real number.

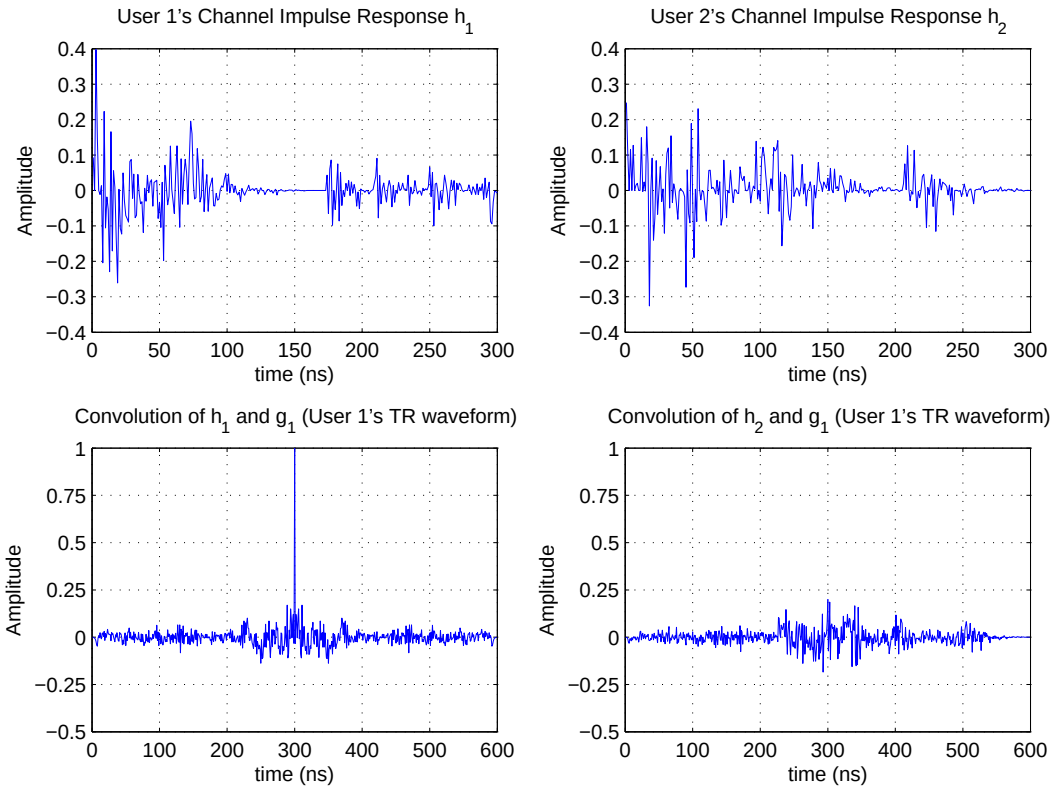

Figure 5.4: Examples of IEEE 802.15.4a outdoor NLOS channels

truncated[8] at $LT_s = 300$ ns (i.e., L=300). In Fig. 5.4, the convolution between User 1's channel response h_1 and its matched TR signature waveform g_1 exhibits a prominent central peak at $(h_1 * g_1)[L-1]$, demonstrating the temporal focusing effect of the TR technique; on the other hand, the amplitude of the convolution between the TR signature waveform g_1 and the mismatched channel response h_2 is significantly smaller than the central peak $(h_1 * g_1)[L-1]$, demonstrating the virtual spatial focusing effect in the user's signature domain.

In the following part of this section, we present our numerical evaluation on

[8]because the amplitude of the remaining paths after 300 ns is typically small enough to be neglected

the BER performance of the proposed 2D interference cancellation scheme. In our simulation, the channel responses for different users are randomly and independently generated using the IEEE 802.15.4a channel model, with $T_s = 1$ ns and $L = 300$. Without loss of generality, the channel response of each user is normalized so that $\sum_{k=0}^{L-1} \left|h_i[k]\right|^2 = 1, \quad \forall i \in \{1, 2, \ldots, N\}$, and assume that all the power control coefficients $a_i = 1, \quad \forall i \in \{1, 2, \ldots, N\}$[9]. A large number of independent trials of channel realizations were conducted and averaged to characterize the average performance of the proposed scheme under this channel model.

5.4.1 BER vs E_b/N_0

In this part, we show the BER performance versus E_b/N_0 (the energy-per-bit to noise-power-spectral-density ratio) with various combinations of rate back-off factor D and the total number of users N. The energy-per-bit E_b is normalized to 1 by the assumption that each BPSK symbol $X_i[k] \in \{-1, +1\}$ has a unit power; accordingly, the power of the received AWGN $\tilde{n}[k]$ at the BS is then given by

$$\sigma_N^2 = \frac{N_0}{2} = \left(\frac{2E_b}{N_0}\right)^{-1}.$$

Fig. 5.5 and Fig. 5.6 show the BER performances of the proposed 2D parallel interference cancellation scheme (up to 3 stages), and compare with the basic TRD-MA system without interference cancellation. Fig. 5.5 considers that case where there are $N = 5$ end-users accessing the BS at the same time with a rate back-off factor $D = 16$ (about 5.3% of the channel length $L = 300$); Fig. 5.6 then presents

[9]To implement an equal power allocation among the users.

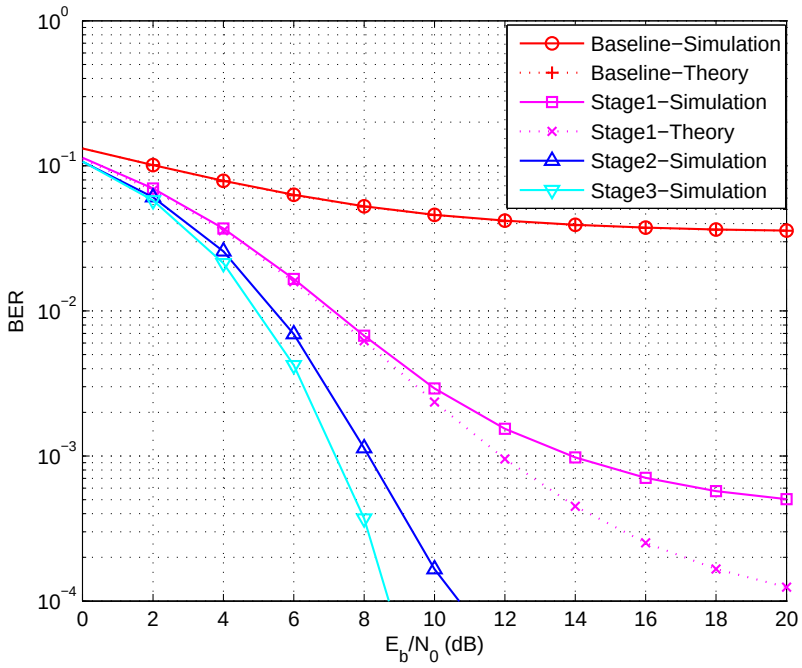

Figure 5.5: The BER performance of the D=16 N=5

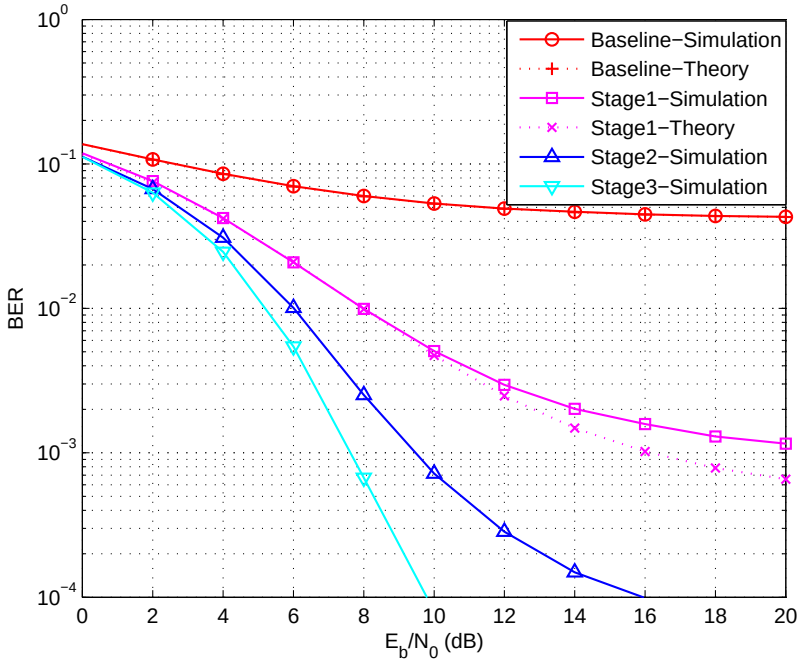

Figure 5.6: The BER performance of the D=32 N=10

the BER performance with $N = 10$ and $D = 32$ (about 10.7% of the channel length).

From both figures, significant BER performance gain is achieved by the proposed 2D parallel interference cancellation scheme, compared with the baseline TRDMA system without interference cancellation. Additional gain is achieved by cascading more stages of the proposed interference cancellation scheme, at the price of increased decoding delay which grows linearly with the total number of stages. The largest gain-per-stage is obtained by the first stage, with the marginal gain diminishes for the following stages. Therefore, there always exists such a tradeoff between the system performance and the number of stages, which should be determined by the applications. Lastly, the theoretical approximation derived in Section V matches reasonably well with the simulation results, considering its complicated correlation between tentative decisions and the Gaussian assumptions we made in the approximation. Comparing Fig. 5.5 and Fig. 5.6, one can see that the accuracy of this approximation improves as the number of users increases, which agrees with the central limit theorem.

5.4.2 Further discussion on high SNR regime

5.4.2.1 BER vs the number of users N

Fig. 5.7 shows how the BER performance changes with the number of users N with high enough SNR. As shown in the example of Fig. 5.7 with the rate back-off factor $D = 32$, the BER increases with the number of users N due to the increased IUI. Targeting at a certain BER level (e.g 10^{-3}), the proposed 2D interference

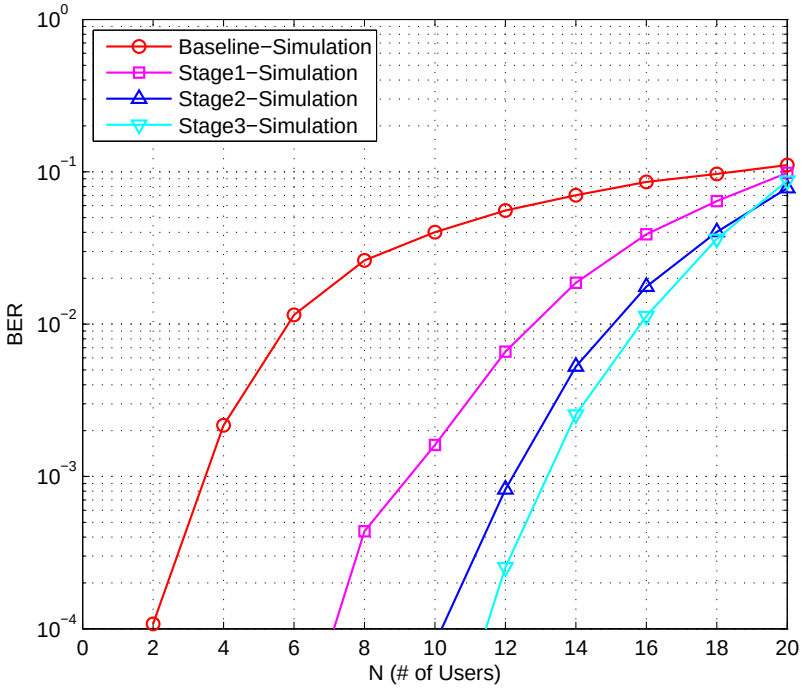

Figure 5.7: The BER performance vs number of users N

cancellation enables more users to transmit simultaneously and therefore increases the system capacity. The benefit of using the interference cancellation diminishes when the BER of the baseline system (considered as the initial stage) is above a certain threshold. This is because the fact that the interference cancellation scheme at the receiver eventually relies on the tentative decisions of the detected symbols to cancel the interference, whose effectiveness inevitably depends on the quality of those tentative decisions.

5.4.2.2 BER vs the rate back-off factor D

Fig. 5.8 shows how the BER performance is affected by the rate back-off factor D with high enough SNR, assuming that there are 5 users accessing the BS

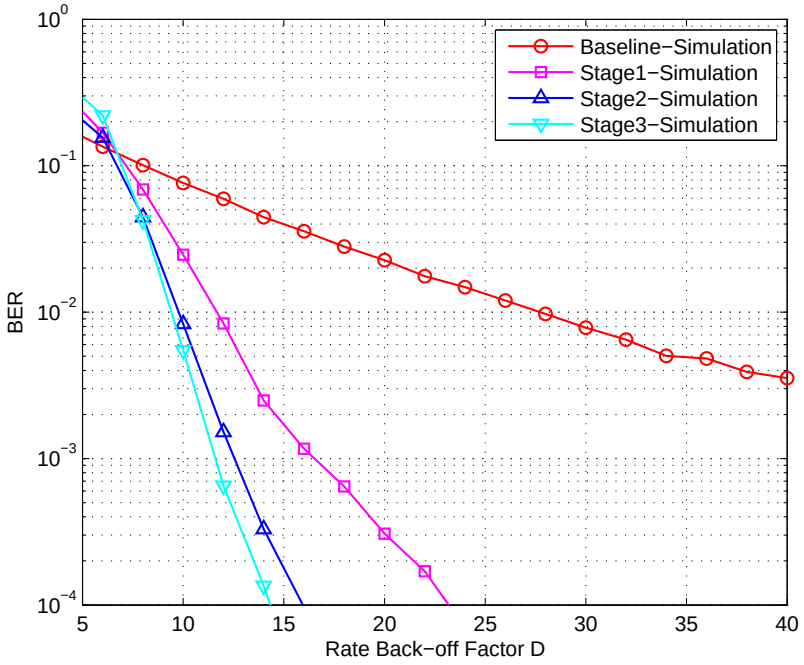

Figure 5.8: The BER performance vs rate back-off factor D

simultaneously. Since both the ISI and the IUI are reduced with a larger rate back-off factor D, the BER decreases as D increases. From Fig. 5.8, one can see that thanks to the proposed 2D parallel interference cancellation scheme, the TRDMA system could use a smaller D to achieve the same BER, which translates to higher throughput for each user. Finally, it is also worth noting that when D is very small (e.g., for $D = 6$ (only 2% of the channel length) in Fig. 5.8), there can be more erroneous tentative decisions (i.e. very high BER ($> 10^{-1}$) for the initial stage) which in turn actually enhance the interference power, rather than canceling. However, most practical TRDMA applications operate at a much lower BER level[10]

[10]A lower BER level can always be achieved by increasing the rate back-off factor D and/or reducing the number of concurrent users N.

for the proposed interference cancellation scheme to contribute.

5.5 Summary

In this chapter, we proposed a 2D parallel interference cancellation scheme to enhance the system performance. The proposed 2D parallel interference cancellation scheme utilizes the tentative decisions of detected symbols to effectively cancel the interference in both the time dimension (ISI) and the user dimension (IUI). To further improve the BER performance, we extended our discussion to a multi-stage scheme by cascading multiple stages of the proposed 2D interference cancellation, with a total delay that increases linearly with the number of stages, but independent of the number of users. Theoretical analysis was made on the BER performance of the single-stage cancellation, and the approximated theoretical result well matched the simulation results. The performance results demonstrated that the proposed 2D parallel interference cancellation scheme can significantly improve the system performance of the TRDMA system.

Chapter 6: Energy-Efficient Base-Station Cooperative Operation with Guaranteed QoS

In this chapter, we propose an energy-efficient base station (BS) switching strategy for cellular systems and use BS cooperation to effectively extend the network service to the areas of the switched-off BSs. Specifically, based on the standard hexagonal cell model [82, 83][1], we consider four progressive BS switch-off patterns and dynamically switch among them according to the traffic load to maximize energy saving. We study the quality of service (QoS) of the resulting cellular system in terms of the call-blocking probability and the channel outage probability, respectively. We derive and analyze the closed-form expressions for the QoS metrics based on the hexagonal cell model. As will be shown in this chapter, the call-blocking probabilities associated with different switch-off patterns characterize a feasible set of patterns to choose from so that the minimum requirement (on the call-blocking

[1] Although regular hexagonal cells hardly exist in real life, the practical deployment of macrocell BSs is always well planned and never random. More importantly, the regularity of such a widely used hexagon model facilitates clear and insightful analysis in the literature, as well as in this chapter. The intention of this work is not to directly solve the detailed real-life problems; rather, it strives to show that the ideas proposed in this work can lead to significant energy-saving potential to cellular networks.

probability for any user equipment (UE)[2]) is satisfied for the given offered load. We guarantee the channel outage probability by identifying the UEs situated at the worst-case locations and use BS cooperation to ensure their minimum QoS requirements. We evaluate the achievable energy saving performance of the proposed scheme and compare them with the conventional network operation.

6.1 System Model

6.1.1 Network Model

We consider a standard cellular network model consisting of hexagonal cells with radius R, and each cell is equipped with a multi-antenna BS located in the center of the cell, as shown in Fig. 6.1. In such a network, the fractional frequency reuse is assumed with the neighboring cells allocated with different bandwidths. The BSs are inter-connected with backhaul links, through which communications are assumed to be low-cost, reliable and high-speed. Each BS has M antennas, and the UEs served by this network have one single antenna.

We assume that in each cell call requests arrive following a Poisson process with an arrival rate $\lambda(t)$ at time t, and the call holding time has an expected value $1/\mu$. Consequently, each cell provides an *offered load* of $E(t) = \lambda(t)/\mu$ (Erlang) to

[2]In the Universal Mobile Telecommunications System (UMTS) and 3GPP Long Term Evolution (LTE), user equipment (UE) is any device used directly by an end-user to communicate, which can be a hand-held telephone, a laptop computer equipped with a mobile broadband adapter, or any other device.

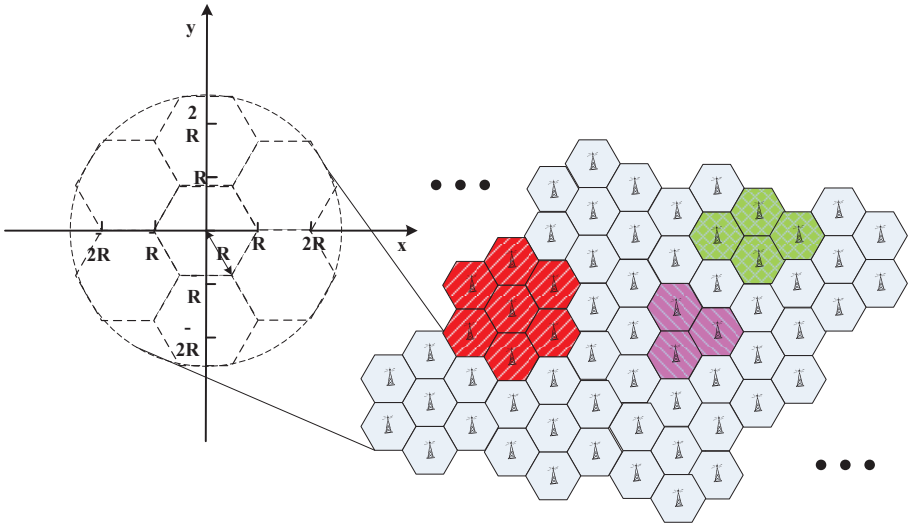

Figure 6.1: A local dense-deployment area covered by hexagonal cells

the cellular infrastructure. For simplicity, we further assume that the offered loads from different cells are independent and identically distributed (i.i.d.).

We consider that each BS has a limited capacity to serve a maximum number of active concurrent UEs due to its limited hardware and software resources [84][3]. This number is denoted by C in this chapter. Note that such a limitation is inherent at the BS and is not necessarily related to the scarcity of channel resources. It means that even when there are ample amount of available channel resources like the case of low traffic hours, an individual BS has to reject a new UE's request if the number of concurrent UEs at this BS will otherwise exceed C.

[3]When a UE is served by multiple BSs through cooperation, this UE accounts for an active UE at each of the BSs that participate this cooperation.

6.1.2 Channel model and Cooperative Coverage Extension

Let $h_k^{(m)}$ denote the fading channel coefficient between a UE and the m-th antenna of the k-th BS. $h_k^{(m)}$ is modeled as circularly symmetric complex Gaussian random variables with zero mean and variance

$$\sigma_k^2 = \frac{G}{d_k^\alpha}, \tag{6.1}$$

where d_k is the distance between the k-th BS and the UE, α is the path loss exponent [39, 85], and G is a normalizing gain factor. Assume that different $h_k^{(m)}$ are uncorrelated, and that the channel state information is available at the BS side.

To efficiently extend coverage to the service areas of the switched-off BSs and compensate the SNR loss due to increased BS-UE distances, the nearby active BSs will use cooperative communications. We limit the set of cooperating BSs to the six direct neighboring BSs of the switched-off cells.

When a BS is switched off, it releases its channel resources to its neighboring active BSs. Then the neighboring active BSs use the channel resources obtained from the switched-off BS to cooperatively serve (using cooperative beamforming) the UEs inside the switched-off cell (referred to as, the *moon cell* in the sequel). In the cells having an active BS (referred to as, the *sun cell*), the UEs are served by the single active BS the same way as in the conventional operation without BS cooperation. Since the traffic load during these off-peak-traffic hours is lower than during peak hours, we assume that during the energy-efficient operations, the available channel resources can accommodate the reduced overall traffic load by

adopting certain interference management scheme [86]. Similar to [8] [12], it is also assumed that the use of cooperative beamforming [87] will not cause a noticeably higher inter-cell interference level compared to the conventional operation. Such an assumption simplifies the analytical derivations, and at the same time can be justified as follows:

- Compared with the conventional cell-breathing scheme (i.e. by simply increasing BS's transmit power) [4], the cooperative beamforming can steer the transmitted signals towards only the intended location where the signals are summed constructively, which effectively reduces the required total transmit power; on the other hand, thanks to the spatial selectivity of cooperative beamforming, the interference signals will be summed destructively at the victim cells, whose power can be expected no much higher than the conventional operation.

- Second, when the fractional frequency reuse is used in this network, two cells that use the same frequency band are separated by a distance. Considering the propagation loss in cellular systems, the interference power is further attenuated when it arrives at the victim cell.

- Third, although it is true that some neighboring cells can be closer to the victim cell, in the BS cooperation, each of the cooperating BSs only needs to transmit just a fraction of the total transmit power, which further eases its interference power to its neighboring cells.

  For the UEs inside a moon cell, the cooperative coverage extension schemes

for both downlink and uplink are specified as follows:

6.1.2.1 Downlink

Since the channel state is known at the BS side, the optimum cooperative transmission scheme is *cooperative transmit beamforming* which maximizes the received SNR at the UE [87]. The resulting SNR at the UE (receiver) is given by:

$$SNR = \sum_{k=1,m=1}^{K,M} \frac{|h_k^{(m)}|^2 P_{\mathtt{BS}}}{N_{\mathtt{UE}}} = \frac{P_{\mathtt{BS}}}{N_{\mathtt{UE}}} \sum_{k=1,m=1}^{K,M} |h_k^{(m)}|^2, \tag{6.2}$$

where $P_{\mathtt{BS}}$ is the total transmit power of all the cooperating BSs[4], $N_{\mathtt{UE}}$ is the noise power at the UE, and K is the number of cooperating BSs. Note that in (6.2), we ignore the interference from other cells for analytical simplicity, given the assumption that the use of cooperative beamforming will not cause a noticeably higher inter-cell interference compared to the conventional operation.

6.1.2.2 Uplink

For uplink, given that the channel state information is available at the BS side, *Maximal Ratio Combining* (MRC) [85, 88] can be achieved by cooperative receive beamforming among cooperating BSs. The resulting SNR at the BS (receiver) side

[4]In order to achieve the SNR level shown in (6.2), the m-th antenna of the k-th BS transmits with a fraction of the total transmit power $\left(|h_k^{(m)}|^2\right) \Big/ \left(\sum_{k=1,m=1}^{K,M} |h_k^{(m)}|^2\right)$. Therefore, we assume that each individual power constraint (limited by the power amplifier) on each antenna and/or BS can be satisfied, and mainly focus on the total transmit power consumption.

is

$$SNR = \sum_{k=1,m=1}^{K,M} \frac{P_{\mathtt{UE}}|h_k^{(m)}|^2}{N_k^{(m)}}. \tag{6.3}$$

where $P_{\mathtt{UE}}$ is the transmit power of the UE, and $N_k^{(m)}$ is the noise power received at the m-th antenna of the k-th BS. For simplicity, we further assume that $N_k^{(m)}$ are identical for all k and m, i.e. $N_k^{(m)} = N_{\mathtt{BS}}$, then

$$SNR = \frac{P_{\mathtt{UE}}}{N_{\mathtt{BS}}} \sum_{k=1,m=1}^{K,M} |h_k^{(m)}|^2. \tag{6.4}$$

Due to the same structure of uplink and downlink shown in (6.2) and (6.4), we could use a unified expression

$$SNR = \sum_{k=1,m=1}^{K,M} \frac{P}{N}|h_k^{(m)}|^2. \tag{6.5}$$

where P and N denote the transmit power and the receiver noise variance, respectively.

6.1.3 Quality of Service Metrics

In this work, we propose an energy-efficient BS switching strategy according to the varying offered traffic load. However, the energy-saving purpose makes sense only when the QoS of a UE is guaranteed to be above a certain required level. In this chapter, we consider and derive the closed-form expressions for two QoS metrics:

- *Call-Blocking Probability*: how likely a UE's request is rejected by the infrastructure due to limited resources.

- *Channel-Outage Probability*: given that a UE's request is not rejected (therefore, a link is established between this UE and available BS(s)), for a certain

given SNR threshold γ_0, how likely the instantaneous received SNR level of the established link is lower than γ_0 due to channel fading.

During the off-peak-traffic hours, some BSs are switched off to save energy. The traffic of the service areas of the switched-off BSs is distributed to the remaining active BSs, which leads to a higher aggregated traffic load for each of the remaining active BSs. For a given offered load per cell, the more BSs are turned off, the more UEs' requests need to be addressed by each active BS. Therefore, the QoS requirement on the call-blocking probability in essence serves as a constraint for the BS switch-off pattern selection. Given that a UE's request has been accepted by the infrastructure, we can then use channel outage probability to measure the quality of the established channel link. In this chapter, we guarantee QoS by targeting at the UEs situated at the worst-case locations in the network.

6.2 BS Switching Patterns and the Call-Blocking Probabilities

In this section, we introduce four BS switching patterns that progressively turn off more BSs according to the offered traffic load. Then, we calculate the call-blocking probability associated with each pattern.

6.2.1 BS Switch-off Patterns

As the offered traffic load goes low, some of the BSs are switched off, resulting in a more energy-efficient network operation, and the corresponding traffic load is distributed among the remaining active BSs. In determining which BSs to switch

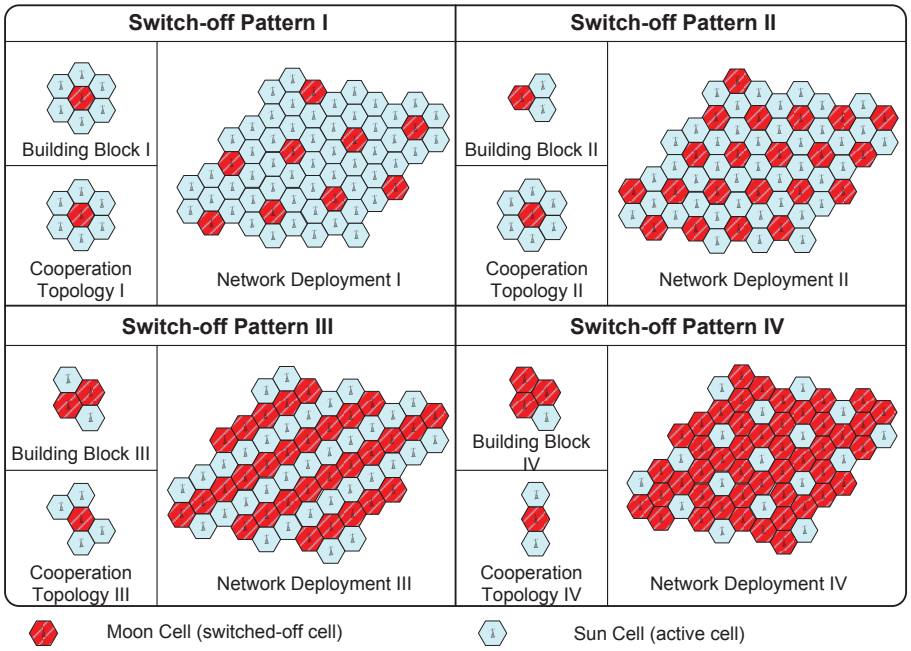

Figure 6.2: Scalable switch-off patterns

off in a large-scale network according to varying offered load, the optimal solution involves integer programming, which is proven to be NP-hard [89, 90]. Some previously proposed suboptimal algorithms [8, 10] did not consider the possibility of BS cooperation in their objective functions. Moreover, even though an optimal solution is available for any given offered load, the operational complexity of constantly switching BSs on and off according to the continuously varying offered load is not affordable for practical use. Therefore, we propose to use a set of BS switching patterns which consist of scalable building blocks to cover the cellular network. Specifically, we consider four switch-off patterns in the context of BS cooperation as shown in Fig. 6.2.

In Fig. 6.2, the diagram of the switch-off pattern I visualizes a basic switching pattern and the resulting cooperation topology when one BS is switched off in a

basic building block of seven BSs. In this pattern, each moon cell is served by up to six[5] neighboring BSs through cooperative communications. We will refer to this case as *pattern I* for short in the sequel. Similarly, three more switch-off patterns II, III, and IV are also presented in Fig. 6.2, corresponding to switching off one BS out of three BSs, switching off two BSs out of four BSs, and switching off three BSs out of four BSs, respectively.

Among a very large number of possible switching patterns, the four switch-off patterns are heuristically chosen as the formations of small regular building blocks, provided that the density of the users is roughly uniform across the cellular network. The regularity brought by these patterns offers great scalability for a large-scale deployment. Furthermore, after being deployed across the network, each of the four patterns results in the same cooperation topology for any moon cell (regardless its location) under that pattern, as shown in Fig. 6.2. Such system-wide homogeneity simplifies the analysis complexity and leads to a unified system analysis for each moon cell. As one can see from Fig. 6.2, the four switch-off patterns from I to IV turn off more BSs in a progressive manner to achieve the energy-saving goal with guaranteed QoS. Defining β to be the ratio of the number of switched-off BSs to the total number of BSs for the four switch-off patterns I, II, III, and IV, we obtain $\beta_{\texttt{I}} = 1/7 = 14.3\%$, $\beta_{\texttt{II}} = 1/3 = 33.3\%$, $\beta_{\texttt{III}} = 2/4 = 50.0\%$, and $\beta_{\texttt{IV}} = 3/4 = 75.0\%$. The conventional operation adopts an *"all-on" pattern*, in which all BSs are active with $\beta_{\texttt{all-on}} = 0$.

[5]When one or more of the six neighboring active BSs are fully occupied due to the limited capacity C, they cannot help the UE by participating the cooperation.

Since the traffic loads originating from the moon cells are distributed to active BSs, we calculate the equivalent aggregated traffic load for each active BS in different patterns. Taking switch-off pattern II shown in Fig. 6.2 for example, each active cell is surrounded by three moon cells that are to be served through cooperating with other active BSs. Unless this active BS is fully occupied, a call attempt from any of these surrounding moon cells will become one additional concurrent UE at this active BS. Therefore, for switch-off pattern II, the aggregated traffic load for each active BS is the sum of the load of its own cell and the loads of all the surrounding moon cells, i.e. $E_{\Sigma,\mathtt{II}}(t) = \frac{(3+1)\lambda(t)}{\mu} = 4E(t)$. Similarly, $E_{\Sigma,\mathtt{I}}(t) = 2E(t)$, $E_{\Sigma,\mathtt{III}}(t) = 5E(t)$, and $E_{\Sigma,\mathtt{IV}}(t) = 7E(t)$. For the conventional operation, $E_{\mathtt{all\text{-}on}}(t) = E(t)$.

Since each active BS only has limited capacity for supporting concurrent UEs, when a UE's request arrives, some BSs may be too busy to help. This gives rise to a set of *cooperating modes* in which some BSs are absent from the basic cooperation topologies shown in Fig. 6.2 due to limited resources.

The complete set of distinguishable cooperating modes (up to rotations and mirroring) is presented in Fig. 6.3. Note that different cooperating modes will appear with different relative frequencies depending on the current offered load and the switch-off pattern.

6.2.2 Call-Blocking Probability

In this part, we calculate the call-blocking probability of the UEs in the network under each proposed pattern. We first define two types of call-blocking events

for the sun cell and the moon cell, respectively.

Definition 5. (Call Blocking for the Sun Cell) *For any given combination of the single-cell offered load E and switch-off pattern $w \in \{I, II, III, IV\}$, the call-blocking event for the UE in the sun cell occurs when* all the C available resources (for concurrent UEs) of the single BS of this sun cell are fully occupied at the time when the UE's request arrives.

Definition 6. (Call Blocking for the Moon Cell) *For any given combination of the single-cell offered load E and switch-off pattern $w \in \{I, II, III, IV\}$, the call-blocking event for the UE in the moon cell occurs when* all the neighboring BSs that remain active are fully occupied at the time when the UE's request arrives.

Since it is assumed that the traffic arrival process is a Poisson process, we use the Erlang-B formula [91] to calculate the blocking probability for each individual active BS, and then investigate the two types of call blocking probabilities. According to the Erlang-B formula, for a queuing system with C servers but no buffer spaces for incoming service requests to wait, if the service arrival process is a Poisson process that offers a traffic load E, the blocking probability of such a queuing system is given by

$$B(E, C) \triangleq \frac{\frac{E^C}{C!}}{\sum_{i=0}^{C} \frac{E^i}{i!}}, \tag{6.6}$$

which corresponds to the conventional all-on pattern without BS cooperation.

Applying the Erlang-B formula to Definition 5, the call blocking probability

for the sun cell can be calculated as follows:

$$P_{\texttt{CB,sun}}\left(E,w\right)=B\left(E_{\Sigma,w}(E),C\right)=\frac{\frac{E_{\Sigma,w}^{C}}{C!}}{\sum\limits_{i=0}^{C}\frac{E_{\Sigma,w}^{i}}{i!}}, \tag{6.7}$$

where E is the single-cell offered load, $w\in\{I,II,III,IV\}$ represents the switch-off pattern, and $E_{\Sigma,w}(E)$ is the aggregated offered load for the active BS of the sun cell under switch-off pattern w.

From Definition 6, the call-blocking probability of the UE in a moon cell can be written as

$$\begin{aligned}P_{\texttt{CB,moon}}\left(E,w\right)&=Pr\big[\bigcap_{k=1}^{K}\{\text{the } k^{th} \text{ BS is fully occupied}\}\big]\\&\leqslant Pr\left[\{\text{the } k^{th} \text{ BS is fully occupied}\}\right],\forall k\\&=P_{\texttt{CB,sun}}\left(E,w\right),\end{aligned} \tag{6.8}$$

where K is the total number of the neighboring active BSs for this moon cell.

From (6.8), one can see that the call-blocking probability for the moon cell is always upper-bounded by the one for the sun cell. This is due to the multi-BS diversity brought by the cooperation among multiple neighboring active BSs for the moon cell. For this reason, in order to guarantee the QoS of UEs in both sun cells and moon cells, we need to ensure that $\max\left\{P_{\texttt{CB,moon}}\left(E,w\right),P_{\texttt{CB,sun}}\left(E,w\right)\right\}=P_{\texttt{CB,sun}}\left(E,w\right)$ is below a certain threshold, by carefully choosing the switching patterns according to the offered load.

6.3 Channel outage Probability

In this section, we focus on the channel outage probability as a physical layer QoS metric given that a channel link has been established between a UE and the BS(s). If a UE's call-attempt is accepted by the available BSs, a link will be established for this UE. Given the condition that a UE's request is not blocked, the channel outage probability measures the quality of the established link. Specifically, we are looking at a conditional probability that is defined as follows:

Definition 7. *(*channel outage probability*) Conditioned on that a UE's request is not blocked, the channel outage probability for this UE is the conditional probability that the instantaneous SNR for the link established between this UE and BS(s) is lower than a certain threshold* γ_0.

It is worth noting that the channel outage probability defined in this work is discussed based on the condition that BS(s) can accommodate the UE's request and establish a link for this UE. Therefore, a so defined channel outage probability, as a conditional probability, focus on the quality of the physical channel established between the BSs and the UE.

To guarantee the QoS for all UEs in energy-efficient operations, a spatially averaged QoS metric is not sufficient. Since a UE can be anywhere within the cell, we will focus on the channel outage probability of the UE situated at the worst transmission/reception location within the cell for each cooperating mode shown in Fig. 6.3. We start with the simple case of the sun cell and the regular cell under

the conventional operation, and then investigate the more complicated cases of the moon cell in the following part of this section.

For the sun cell (or equivalently, the regular cell under the conventional operation), the UE is served by just one BS located in the center of the cell. Therefore, the distance between its worst-case location and the BS is the radius of the cell R. The corresponding SNR expression is a special case of (6.5) with $K = 1$:

$$SNR = \frac{P}{N} \sum_{m=1}^{M} |h_0^{(m)}|^2 = \frac{P}{N} \frac{\sigma_0^2}{2} \sum_{m=1}^{M} \frac{2}{\sigma_0^2} |h_0^{(m)}|^2, \tag{6.9}$$

where N is the noise power, P is the total transmit power of BS (downlink) or UE (uplink), and $h_0^{(m)}$ is the channel gain between the UE and the m-th antenna of the BS with variance $\sigma_0^2 = \frac{G}{R^\alpha}$.

For ease of simple notation, let $V \triangleq \sum_{m=1}^{M} \frac{2}{\sigma_0^2} |h_0^{(m)}|^2$, which is a central chi-square random variable with $2M$ degrees of freedom. Thus, the channel outage probability for the UE in the sun cell (or equivalently, the UE under the conventional operation) can be obtained as

$$P_{\mathtt{out}}\,(sun) = Pr\left[V \leqslant \frac{2\gamma_0 N}{P\sigma_0^2}\right] = \frac{\gamma\left(M, \frac{\gamma_0 N R^\alpha}{PG}\right)}{(M-1)!}, \tag{6.10}$$

where $\gamma(s, x) = \int_0^x t^{s-1} e^{-t} dt$ is the lower incomplete Gamma function.

For the moon cell, we first identify the worst-case locations for each cooperating modes shown in Fig. 6.3. Based on that, the channel outage probability of the UE at the worst-case locations is derived for each mode. Finally, we combine the individual channel outage probability of every cooperating mode using the relative frequencies of these cooperating modes that we obtained from computer simulation.

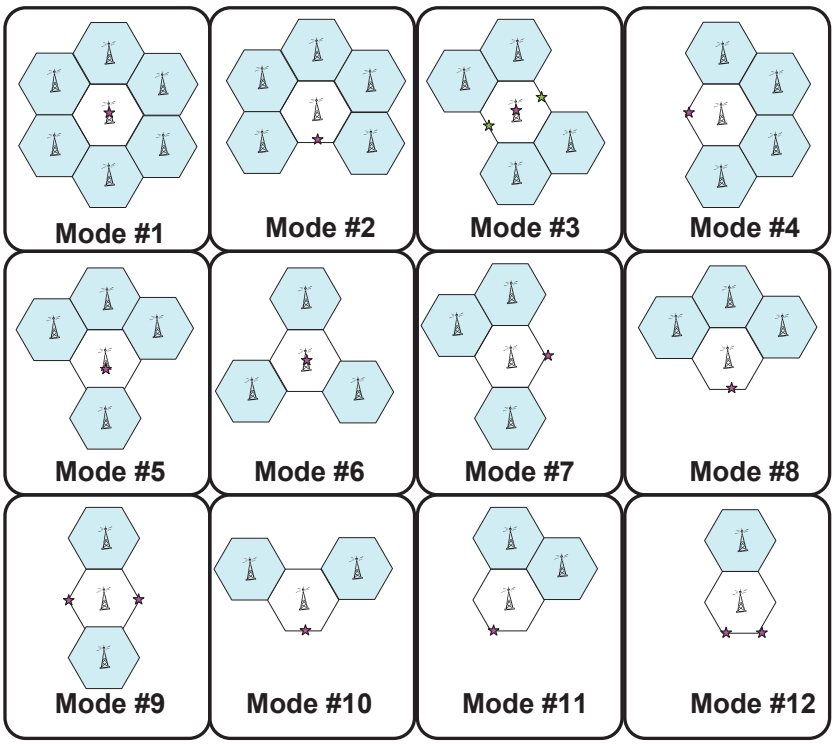

Figure 6.3: The complete set of distinguishable cooperating modes

6.3.1 Worst-Case Location

To guarantee the channel outage probability of the UEs in the moon cells, the first step is to determine the worst-case location within the moon cell, given the number and locations of the available BSs under each cooperating mode. Fitting their geological locations into a two-dimensional coordinate system as shown in Fig. 6.1, the BS and UE locations are each assigned a pair of coordinates. Specifically, we assign coordinates to the cooperating BSs and the UE according to

$$BS_1 = (x_1, y_1), \cdots, BS_K = (x_K, y_K);\ UE = (x, y).$$

Then, the distance between the UE and BS_k can be written as

$$d_k = \left[(x - x_k)^2 + (y - y_k)^2\right]^{\frac{1}{2}}. \tag{6.11}$$

Given the cooperative coverage extension scheme introduced in Section II, the resulting SNR is proportional to the sum $\sum_{k=1,m=1}^{K,M} |h_k^{(m)}|^2$. To determine the worst-case location, we will only need to take into account the effect of path loss by averaging out the fading component:

$$E\left[\sum_{k=1,m=1}^{K,M} |h_k^{(m)}|^2\right] = M\sum_{k=1}^{K}\frac{G}{d_k^{\alpha}}, \tag{6.12}$$

where K is the number of cooperating BSs and M is the number of antennas at each BS.

Consequently, determining the worst-case location within the switched-off hexagonal area is equivalent to solving the following constrained minimization problem:

$$\min_{x,y} \quad f(x,y) = \sum_{k=1}^{K}\frac{1}{[(x-x_k)^2+(y-y_k)^2]^{\frac{\alpha}{2}}} \tag{6.13}$$

$$\text{s. t.} \begin{cases} -\sqrt{3}R \leqslant \sqrt{3}x + y \leqslant \sqrt{3}R; \\ -\sqrt{3}R \leqslant \sqrt{3}x - y \leqslant \sqrt{3}R; \\ -\frac{\sqrt{3}}{2}R \leqslant y \leqslant \frac{\sqrt{3}}{2}R. \end{cases} \tag{6.14}$$

Since both the objective function and the constrains are continuously differentiable, the Karush-Kuhn-Tucker (KKT) [92] conditions specify the necessary conditions for the solution (x^*, y^*) as follows:

- **Stationarity Condition**

$$\nabla f(x^*,y^*) + (\mu_1-\mu_2)\begin{bmatrix}\sqrt{3}\\ 1\end{bmatrix} + (\mu_3-\mu_4)\begin{bmatrix}\sqrt{3}\\ -1\end{bmatrix} + (\mu_5-\mu_6)\begin{bmatrix}0\\ 1\end{bmatrix} = 0, \tag{6.15}$$

where

$$\nabla f(x,y) = \begin{bmatrix} \frac{\partial}{\partial x} f(x,y) \\ \frac{\partial}{\partial y} f(x,y) \end{bmatrix} = \begin{bmatrix} -\alpha \sum_{k=1}^{K} \frac{x-x_k}{[(x-x_k)^2+(y-y_k)^2]^{\frac{\alpha}{2}+1}} \\ -\alpha \sum_{k=1}^{K} \frac{y-y_k}{[(x-x_k)^2+(y-y_k)^2]^{\frac{\alpha}{2}+1}} \end{bmatrix}. \tag{6.16}$$

- **Dual Feasibility Condition**

$$\mu_i \geqslant 0, \quad \text{for all } i = 1, \ldots, 6; \tag{6.17}$$

- **Primal Feasibility Condition**

$$\begin{cases} -\sqrt{3}R \leqslant \sqrt{3}x^* + y^* \leqslant \sqrt{3}R \\ -\sqrt{3}R \leqslant \sqrt{3}x^* - y^* \leqslant \sqrt{3}R \\ -\frac{\sqrt{3}}{2}R \leqslant y^* \leqslant \frac{\sqrt{3}}{2}R \end{cases} \tag{6.18}$$

- **Complementary Slackness Condition**

$$\begin{cases} \mu_1 \left(\sqrt{3}x^* + y^* - \sqrt{3}R\right) = 0; \quad \mu_2 \left(\sqrt{3}x^* + y^* + \sqrt{3}R\right) = 0; \\ \mu_3 \left(\sqrt{3}x^* - y^* - \sqrt{3}R\right) = 0; \quad \mu_4 \left(\sqrt{3}x^* - y^* + \sqrt{3}R\right) = 0; \\ \mu_5 \left(y^* - \frac{\sqrt{3}}{2}R\right) = 0; \qquad \mu_6 \left(y^* + \frac{\sqrt{3}}{2}R\right) = 0; \end{cases} \tag{6.19}$$

Leveraging the geological symmetry in each cooperating mode shown in Fig. 6.3, the worst case location of a UE in the moon cell can be found without much effort from the KKT conditions. Specifically, we have the solution for the worst-case location(s) of each cooperating mode with $\alpha = 3$ (low path loss) and $\alpha = 4$ (high path loss) shown in Table 6.1.

6.3.2 Channel Outage Probability of Each Cooperating Mode

In this part, we analyze the channel outage probability of the UEs situated at the worst-case locations within the switched-off (moon) cell. According to Table 6.1,

Table 6.1: Solutions for The Worst-Case Location(s) (x^*, y^*)

	♯1	♯2	♯3	♯4	♯5	♯6
$\alpha=3$	$(0,0)$	$\left(0,-\frac{\sqrt{3}R}{2}\right)$	$\pm\left(\frac{\sqrt{3}R}{4},\frac{3R}{4}\right)$	$(-R,0)$	$(0,-0.1872R)$	$(0,0)$
$\alpha=4$	$(0,0)$	$\left(0,-\frac{\sqrt{3}R}{2}\right)$	$(0,0)$	$(-R,0)$	$(0,-0.1478R)$	$(0,0)$
	♯7	♯8	♯9	♯10	♯11	♯12
$\alpha=3$	$(R,0)$	$\left(0,-\frac{\sqrt{3}R}{2}\right)$	$(\pm R,0)$	$\left(0,-\frac{\sqrt{3}R}{2}\right)$	$\left(-\frac{R}{2},-\frac{\sqrt{3}R}{2}\right)$	$\left(\pm\frac{R}{2},-\frac{\sqrt{3}R}{2}\right)$
$\alpha=4$	$(R,0)$	$\left(0,-\frac{\sqrt{3}R}{2}\right)$	$(\pm R,0)$	$\left(0,-\frac{\sqrt{3}R}{2}\right)$	$\left(-\frac{R}{2},-\frac{\sqrt{3}R}{2}\right)$	$\left(\pm\frac{R}{2},-\frac{\sqrt{3}R}{2}\right)$

we divide all the cooperating modes into two categories: the symmetric BS arrangements and the asymmetric BS arrangements. The symmetric arrangements include the cooperating modes $\{\sharp 1, \sharp 3(\alpha=4), \sharp 6, \sharp 9, \sharp 10, \sharp 11\}$, in each of which the neighboring active BSs are equally far away from the worst UE location(s); The asymmetric arrangements include the modes $\{\sharp 2, \sharp 3(\alpha=3), \sharp 4, \sharp 5, \sharp 7, \sharp 8, \sharp 12\}$, in which the neighboring active BSs are of different distances from the worst location(s).

6.3.2.1 Symmetric BS Arrangements

For the symmetric cases in Fig. 6.3, such a symmetric geometry leads to identical channel gain variances $\sigma_k^2 = \frac{G}{d_k^\alpha} = \frac{G}{d^\alpha}$, for $k = 1, \cdots, K$. Therefore, (6.5) can be written as

$$SNR = \frac{P}{N}\frac{\sigma_k^2}{2}\sum_{k=1,m=1}^{K,M}\frac{2}{\sigma_k^2}|h_k^{(m)}|^2. \tag{6.20}$$

Since $W \triangleq \sum_{k=1,m=1}^{K,M} \frac{2}{\sigma_k^2}|h_k^{(m)}|^2$ is a central chi-square random variable with $2MK$ degrees of freedom, the probability $Pr[W \leqslant w]$ (i.e. the CDF of W) is given by

$$Pr[W \leqslant w] = \frac{\gamma(MK, \frac{w}{2})}{(MK-1)!}. \tag{6.21}$$

Accordingly, the outage probability can be written as

$$P_{\mathtt{out}} = Pr[SNR \leqslant \gamma_0] = \frac{\gamma\left(MK, \frac{\gamma_0 N d^\alpha}{PG}\right)}{(MK-1)!}. \tag{6.22}$$

Applying (6.22) to $\{\sharp 1, \sharp 3(\alpha=4), \sharp 6, \sharp 9, \sharp 10, \sharp 11\}$, we obtain their channel outage probabilities in Table 6.2.

Table 6.2: Outage Probabilities of Symmetric BS Arrangements

	K	d	σ^2	P_{out}
$\sharp 1$	6	$\sqrt{3}R$	$\frac{G}{\left(\sqrt{3}R\right)^\alpha}$	$\frac{\gamma\left(6M, \frac{\gamma_0 N(\sqrt{3}R)^\alpha}{PG}\right)}{(6M-1)!}$
$\sharp 3(\alpha=4)$	4	$\sqrt{3}R$	$\frac{G}{\left(\sqrt{3}R\right)^\alpha}$	$\frac{\gamma\left(4M, \frac{9\gamma_0 N R^\alpha}{PG}\right)}{(4M-1)!}$
$\sharp 6$	3	$\sqrt{3}R$	$\frac{G}{\left(\sqrt{3}R\right)^\alpha}$	$\frac{\gamma\left(3M, \frac{\gamma_0 N(\sqrt{3}R)^\alpha}{PG}\right)}{(3M-1)!}$
$\sharp 9$	2	$2R$	$\frac{G}{(2R)^\alpha}$	$\frac{\gamma\left(2M, \frac{\gamma_0 N(2R)^\alpha}{PG}\right)}{(2M-1)!}$
$\sharp 10$	2	$\frac{\sqrt{21}}{2}R$	$\frac{G}{\left(\frac{\sqrt{21}}{2}R\right)^\alpha}$	$\frac{\gamma\left(2M, \frac{\gamma_0 N\left(\frac{\sqrt{21}}{2}R\right)^\alpha}{PG}\right)}{(2M-1)!}$
$\sharp 11$	2	$\sqrt{7}R$	$\frac{G}{\left(\sqrt{7}R\right)^\alpha}$	$\frac{\gamma\left(2M, \frac{\gamma_0 N(\sqrt{7}R)^\alpha}{PG}\right)}{(2M-1)!}$

6.3.2.2 Asymmetric BS Arrangements

For the asymmetric cases shown in Fig. 6.3, the distances between the worst-case UE location and the cooperating BSs are different. The resulting SNR as shown in (6.5) can be considered as a linear combination of multiple chi-square random variables. Unfortunately, even for the two-variable case, the exact expression for the SNR distribution is too complicated for practical applications. Thus, we use an approximation developed in [93], whose accuracy has been proven to be very well satisfying in many practical applications [93–95].

In doing so, the distribution of the SNR is approximated by that of another random variable $Z = \delta\Psi$, where δ is a scaling factor and Ψ is a central chi-square random variable with s degrees of freedom, such that the expected value and variance of the SNR are equal to those of Z. Specifically,

$$\begin{cases} E\left[SNR\right] = \delta E\left[\Psi\right] = \delta s \\ Var\left[SNR\right] = \delta^2 Var\left[\Psi\right] = 2\delta^2 s \end{cases} \tag{6.23}$$

To show how to apply this approximation to the asymmetric BS arrangements, without loss of generality, we take the cooperating mode ♯7 for example. All the other modes of the asymmetric BS arrangements can be approximated similarly.

For the cooperating mode ♯7, the distances between the worst-case UE location and the three cooperating BSs are $d_1 = \sqrt{7}R$, $d_2 = 2R$, and $d_3 = 2R$, respectively. Then, we can rewrite (6.5) as

$$SNR = \frac{\sigma_1^2 P}{2N} \sum_{m=1}^{M} \frac{2}{\sigma_1^2} |h_1^{(m)}|^2 + \frac{\sigma_2^2 P}{2N} \sum_{k=2,m=1}^{K=3,M} \frac{2}{\sigma_k^2} |h_k^{(m)}|^2, \tag{6.24}$$

where $\sigma_1^2 = \frac{G}{\left(\sqrt{7}R\right)^\alpha}$, and $\sigma_2^2 = \sigma_3^2 = \frac{G}{(2R)^\alpha}$. Let $Z_1 \triangleq \sum_{m=1}^{M} \frac{2}{\sigma_1^2}|h_1^{(m)}|^2$ and $Z_2 \triangleq \sum_{k=2,m=1}^{K=3,M} \frac{2}{\sigma_k^2}|h_k^{(m)}|^2$, which are two central chi-square random variables with $2M$ and $4M$ degrees of freedom, respectively. Then, the expected value and the variance of the SNR shown in (6.24) can be obtained as follows:

$$E\left[SNR\right] = \frac{\sigma_1^2 P}{2N} 2M + \frac{\sigma_2^2 P}{2N} 4M = \frac{P}{N}\left(\sigma_1^2 M + 2\sigma_2^2 M\right); \tag{6.25}$$

$$Var\left[SNR\right] = 4\left(\frac{\sigma_1^2 P}{2N}\right)^2 M + 8\left(\frac{\sigma_2^2 P}{2N}\right)^2 M. \tag{6.26}$$

According to (6.23), we have the following equations to solve for s:

$$\frac{\sigma_1^4}{2} M + \sigma_2^4 M = \frac{1}{s}\left(\sigma_1^2 M + 2\sigma_2^2 M\right)^2, \tag{6.27}$$

which yields

$$s = 2M\frac{\left(\sigma_1^2 + 2\sigma_2^2\right)^2}{\sigma_1^4 + 2\sigma_2^4} = 2M\frac{\left(7^{-\alpha/2} + 2^{1-\alpha}\right)^2}{7^{-\alpha} + 2^{1-2\alpha}}, \tag{6.28}$$

and thus

$$\delta = \frac{E\left[SNR\right]}{s} = \frac{P\left(\sigma_1^4 + 2\sigma_2^4\right)}{2N\left(\sigma^2 + 2\sigma_2^2\right)} = \frac{PG\left(7^{-\alpha} + 2^{1-2\alpha}\right)}{2NR^\alpha\left(7^{-\frac{\alpha}{2}} + 2^{1-\alpha}\right)}. \tag{6.29}$$

Following [93], the SNR is approximated by $Z = \delta\Psi$, where Ψ is distributed as a chi-square random variable with s degrees of freedom, so the outage probability can be approximated as

$$\begin{aligned} P_{\mathtt{out}}\left(\sharp 7\right) &= Pr\left[SNR \leqslant \gamma_0\right] \approx Pr\left[Z \leqslant \gamma_0\right] = Pr\left[\Psi \leqslant \frac{\gamma_0}{\delta}\right] \\ &= \frac{\gamma\left(\frac{s}{2}, \frac{\gamma_0 NR^\alpha\left(7^{-\alpha/2}+2^{1-\alpha}\right)}{PG\left(7^{-\alpha}+2^{1-2\alpha}\right)}\right)}{\Gamma\left(s/2\right)}, \end{aligned} \tag{6.30}$$

where $\Gamma\left(x\right) = \int_0^\infty t^{x-1}e^{-t}dt$ is the Gamma function.

Similarly, we can obtain the worst-case probabilities of other cooperating modes with asymmetric BS arrangements and summarize in Table 6.3.

Table 6.3: Outage Probabilities of asymmetric BS Arrangements

Modes	s	P_{out}
$\sharp 2$	$2M\frac{\left[\left(\frac{3}{2}\sqrt{3}\right)^{-\alpha}+2\left(\frac{\sqrt{21}}{2}\right)^{-\alpha}+2\left(\frac{3}{2}\right)^{-\alpha}\right]^2}{\left(\frac{27}{4}\right)^{-\alpha}+2\left(\frac{21}{4}\right)^{-\alpha}+2\left(\frac{9}{4}\right)^{-\alpha}}$	$\frac{\gamma\left(\frac{s}{2},\frac{N\gamma_0 R^\alpha\left[\left(\frac{3}{2}\sqrt{3}\right)^{-\alpha}+2\left(\frac{\sqrt{21}}{2}\right)^{-\alpha}+2\left(\frac{3}{2}\right)^{-\alpha}\right]}{PG\left[\left(\frac{27}{4}\right)^{-\alpha}+2\left(\frac{21}{4}\right)^{-\alpha}+2\left(\frac{9}{4}\right)^{-\alpha}\right]}\right)}{\Gamma\left(\frac{s}{2}\right)}$
$\sharp 3(\alpha=3)$	$4M\frac{\left[\left(\frac{3}{2}\right)^{-\alpha}+\left(\frac{\sqrt{21}}{2}\right)^{-\alpha}\right]^2}{\left(\frac{9}{4}\right)^{-\alpha}+\left(\frac{21}{4}\right)^{-\alpha}}=6.0807M$	$\frac{\gamma\left(\frac{s}{2},\frac{N\gamma_0 R^\alpha\left[\left(\frac{3}{2}\right)^{-\alpha}+\left(\frac{\sqrt{21}}{2}\right)^{-\alpha}\right]}{PG\left[\left(\frac{9}{4}\right)^{-\alpha}+\left(\frac{21}{4}\right)^{-\alpha}\right]}\right)}{\Gamma\left(\frac{s}{2}\right)}=\frac{\gamma\left(3.0404M,4.0065\frac{N\gamma_0 R^3}{PG}\right)}{\Gamma(3.0404M)}$
$\sharp 4$	$4M\frac{\left[2^{-\alpha}+\left(\sqrt{7}\right)^{-\alpha}\right]^2}{\left(4^{-\alpha}+7^{-\alpha}\right)}$	$\frac{\gamma\left(\frac{s}{2},\frac{N\gamma_0 R^\alpha\left[2^{-\alpha}+\left(\sqrt{7}\right)^{-\alpha}\right]}{PG\left(4^{-\alpha}+7^{-\alpha}\right)}\right)}{\Gamma\left(\frac{s}{2}\right)}$
$\sharp 5(\alpha=3)$	$7.4343M$	$\frac{\gamma\left(3.7171M,5.0410\frac{N\gamma_0 R^3}{PG}\right)}{\Gamma(3.7171M)}$
$\sharp 5(\alpha=4)$	$7.3808M$	$\frac{\gamma\left(3.6904M,8.6892\frac{N\gamma_0 R^4}{PG}\right)}{\Gamma(3.6904M)}$
$\sharp 7$	$2M\frac{\left(\sigma_1^2+2\sigma_2^2\right)^2}{\sigma_1^4+2\sigma_2^4}=2M\frac{\left(7^{-\alpha/2}+2^{1-\alpha}\right)^2}{7^{-\alpha}+2^{1-2\alpha}}$	$\frac{\gamma\left(\frac{s}{2},\frac{\gamma_0 N R^\alpha\left(7^{-\alpha/2}+2^{1-\alpha}\right)}{PG\left(7^{-\alpha}+2^{1-2\alpha}\right)}\right)}{\Gamma(s/2)}$
$\sharp 8$	$2M\frac{\left[\left(\frac{3\sqrt{3}}{2}\right)^{-\alpha}+2\left(\frac{\sqrt{21}}{2}\right)^{-\alpha}\right]^2}{\left(\frac{27}{4}\right)^{-\alpha}+2\left(\frac{21}{4}\right)^{-\alpha}}$	$\frac{\gamma\left(\frac{s}{2},\frac{N\gamma_0 R^\alpha\left[\left(\frac{3\sqrt{3}}{2}\right)^{-\alpha}+2\left(\frac{\sqrt{21}}{2}\right)^{-\alpha}\right]}{PG\left[\left(\frac{27}{4}\right)^{-\alpha}+2\left(\frac{21}{4}\right)^{-\alpha}\right]}\right)}{\Gamma\left(\frac{s}{2}\right)}$
$\sharp 12$	$2M$	$\frac{\gamma\left(M,\frac{N\gamma_0 R^\alpha\left(\sqrt{7}\right)^\alpha}{PG}\right)}{(M-1)!}$

6.3.3 Overall Channel Outage Probability

The overall channel outage probability for the UE in the moon cell can be obtained by combining the individual channel outage probability of every cooperating mode according to their relative frequencies. Specifically, the overall channel outage probability of pattern $w \in \{I, II, III, IV\}$ is obtained as follows,

$$P_{\texttt{overall}}(w) = \sum_{i=1}^{12} f_i(w, E)\, P_{\texttt{out}}(\sharp i) \tag{6.31}$$

where $f_i(w,E) \triangleq \frac{N_i(w,E)}{\sum_{i=1}^{12} N_i(w,E)}$ is the relative frequency of the $i-$th cooperating mode under pattern w among all the 12 cooperating modes shown in Fig. 6.3, when the offered load of each cell is E; $P_{\mathtt{out}}(\sharp i)$ is the worst-case channel outage probability of cooperating mode $\sharp i$.

The relative frequency of each cooperating mode can be obtained by conducting a computer simulation of the system dynamics. For each switch-off pattern based on the system model introduced in Section II, we count the frequency of each cooperating mode over a large number of time quanta. In this simulation, each cell (either sun cell or moon cell) supplies an i.i.d. offered load of E to the infrastructure. The offered load is then aggregated at each active BS which has a limited capacity of C active concurrent UEs, according to the chosen switch-off pattern. The histograms of the relative frequencies of the cooperating modes under each pattern is shown with both low and high traffic loads in Section 6.5.

6.4 Energy Saving Analysis

In this section, we quantify the energy saving achieved by the proposed scheme. When a BS is switched off, only a negligible amount of energy is consumed[6]. When a BS is on, the total power consumption $P_{\mathtt{total}}$ of an active BS can be divided into two main parts [96, 97]:

[6]This very small amount of energy is consumed by some mechanism of a turned-off BS to turn it back on. For simplicity, we approximate such an amount close to zero, considering that such mechanism can be implemented through a network interface to the backhaul network (dedicated wired network) which consumes a negligible amount of power.

- The idle power consumption, represented by $P_{\texttt{idle}}$, which does not depend on the network traffic load. This power is consumed as long as a BS is on, even if there is little traffic load.

- The transmit power consumption, represented by $P_{\texttt{RF}}$, which depends on the network traffic load. This part mainly includes the consumption of the radio frequency (RF) output components. Specifically, we model $P_{\texttt{RF}}$ as $P_{\texttt{RF}} = E\frac{P_{\texttt{RF,Peak}}}{E_{\texttt{Peak}}}$, where $E_{\texttt{Peak}}$ denotes the offered load during peak hours, and $P_{\texttt{RF,Peak}}$ represents a BS's total transmit power consumption during peak hours under conventional operation (with all BSs remaining active).

We also assume that the additional baseband signal processing power consumed due to cooperation among active BSs is negligible compared to the aforementioned two main parts.

Define $\eta \triangleq \frac{P_{\texttt{RF,Peak}}}{P_{\texttt{idle}}}$, then the energy consumption per BS under the conventional operation can be calculated as follows:

$$D_{\texttt{conv}} = P_{\texttt{idle}} + E\frac{P_{\texttt{RF,Peak}}}{E_{\texttt{Peak}}} = P_{\texttt{idle}}\left(1 + \eta\frac{E}{E_{\texttt{Peak}}}\right), \tag{6.32}$$

where $P_{\texttt{RF,Peak}}$ is assumed to be just enough to guarantee the channel outage probability of the UE at the worst case location under conventional operation during peak hours.

During energy-efficient operations, the UEs of the sun cell are served by the single BS inside the sun cell in the same way of conventional operation. Meanwhile, depending on which pattern to use, a portion β of BSs are switched off, resulting in $\beta P_{\texttt{idle}}$ power saving and transferring the traffic load from the moon cells to the

remaining active BSs. Since the minimum requirement of channel outage probability is guaranteed for the UE at the worst-case locations through transmit power control, the calculation of the total energy consumption has to take into account the changes of $P_{\mathtt{RF}}$ for the moon cells. On the one hand, due to increased distances between the UEs of the moon cell and active BSs, the required $P_{\mathtt{RF}}$ will increase to maintain the minimum QoS requirement for the worst-case locations. On the other hand, the use of BS-cooperation helps significantly reduce such a penalty of increased $P_{\mathtt{RF}}$. We define ρ as the ratio of the total transmit power required for cooperative transmission to the transmit power required in conventional operation to maintain the same minimum channel outage probability for their corresponding worst-case locations. The *energy consumption per BS* under energy-efficient operations is defined as the ratio of the total energy consumed to serve every cell (including both moon and sun cells) to the total number of BSs (including both active and switched-off BSs), which can be written as

$$\begin{aligned} D_{\mathtt{eff}} &= (1-\beta)\left(P_{\mathtt{idle}} + P_{\mathtt{RF}}\right) + \rho\beta P_{\mathtt{RF}} \\ &= P_{\mathtt{idle}}\left[(1-\beta) + (1-\beta)\,\eta\frac{E}{E_{\mathtt{Peak}}} + \rho\beta\eta\frac{E}{E_{\mathtt{Peak}}}\right] \\ &= P_{\mathtt{idle}}\left[1-\beta+\eta\frac{E}{E_{\mathtt{Peak}}}\left(1+\beta\left(\rho-1\right)\right)\right]. \end{aligned} \tag{6.33}$$

6.5 Numerical Results

In this section, we present some numerical results showing the performance and the energy saving potential of such an energy-efficient cellular network employing the proposed BS switching patterns and cooperative coverage extension scheme.

In the numerical evaluations, unless otherwise stated, the system parameters are chosen as shown in Table 6.4.

Table 6.4: System Parameters

Switch-off Patterns	I, II, III, IV
Offered Load E	[0:2:40] (Erlang)
BS Service Capacity C	50
Cell Radius R	Normalized to 1
Number of antennas at BS M	4
Number of antennas at the UE	1
$\phi = \frac{P}{\gamma_0 N R^\alpha / G}$	[-10:5:25] dB
$\eta = \frac{P_{\mathtt{RF,Peak}}}{P_{\mathtt{idle}}}$	10%
$E_{\mathtt{Peak}}$	40 (Erlang)
Path-loss Exponent α	4
QoS Threshold: Call-blocking Probability	$\leqslant 2\%$
QoS Threshold: Channel Outage Probability	$\leqslant 10^{-3}$

6.5.1 Call-Blocking Probability

In this part, we present the call-blocking probabilities for the switch-off patterns and compare them with the conventional all-on pattern (i.e. all BSs are active

without cooperation). As shown in Section 6.2.2, the call-blocking probability for the sun cell always serves as an upper bound for that of the moon cell. In this chapter, we guarantee the QoS of UEs by targeting at the performances of a UE situated in the worst case. In doing so, we focus the call-blocking probability of the sun cell that represents the minimum QoS level to be maintained when switching off BSs.

Fig. 6.4 shows the worst-case (sun cell) call-blocking probabilities of different patterns. From Fig. 6.4, one can see that switching off more BSs would incur higher probability of call blocking, since each active BS is responsible for a larger aggregated traffic load. Thus, the correspondence between the pattern and the call-blocking probability characterizes a feasible set of candidate patterns so that the minimum QoS requirement on the call-blocking probability is satisfied for a given offered load. Specifically, for the numerical results shown in Fig. 6.4, the feasible set S is given by

$$S = \begin{cases} \{All-on, I, II, III, IV\}, & if\ E \in [0, 5.75); \\ \{All-on, I, II, III\}, & if\ E \in [5.75, 8.05); \\ \{All-on, I, II\}, & if\ E \in [8.05, 10.06); \\ \{All-on, I\}, & if\ E \in [10.06, 20.13); \\ \{All-on\}, & if\ E \in [20.13, 40.25]. \end{cases} \tag{6.34}$$

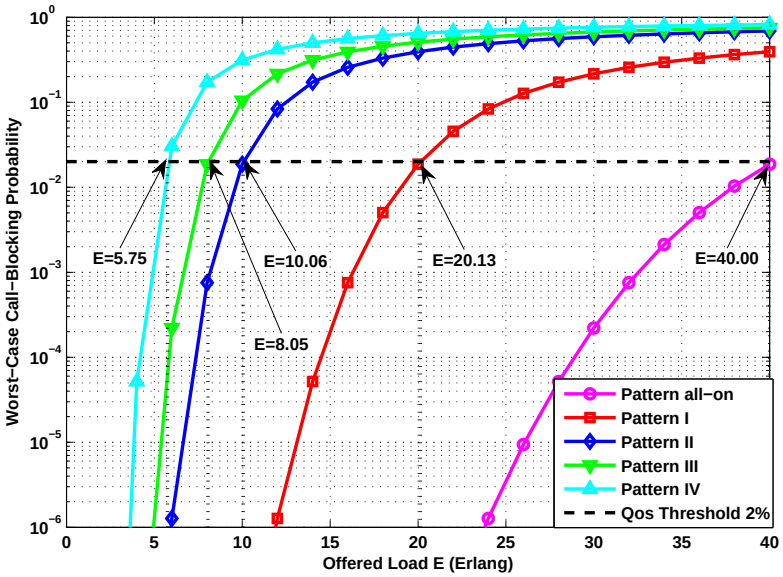

Figure 6.4: The worst-case (sun cell) call-blocking probabilities versus the offered load

6.5.2 Channel Outage Probability

In this part, we show the numerical results of the channel outage probability defined and analyzed in Section 6.3. Fig. 6.5 shows the histograms of the relative frequencies of the 12 cooperating modes with various traffic loads. In Fig. 6.5, two observations are of interest: one is that a more conservative (i.e. turning off less BSs) pattern exhibits a better chance to have more BSs cooperatively serve the UEs than the more aggressive (i.e. turning off more BSs) pattern; the other is that given a switch-off pattern, as the traffic load grows, more BSs will be out of the cooperation because they are too busy (i.e. fully occupied) to help.

To characterize the channel outage probability, we define $\phi = \frac{P}{\gamma_0 N R^\alpha / G}$, where the denominator $\gamma_0 N R^\alpha / G$ is predefined for a given network and fixed in our sim-

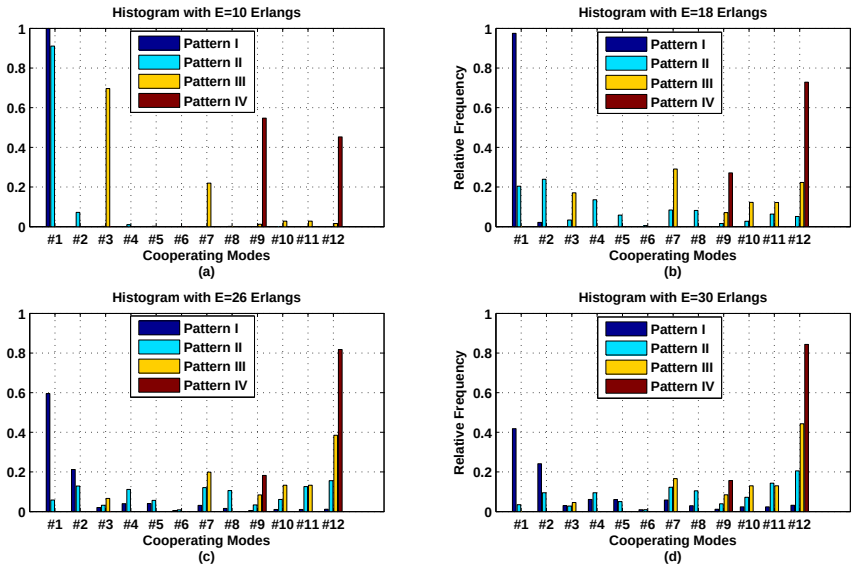

Figure 6.5: The histogram of the relative frequencies of the cooperating modes under different switch-off patterns

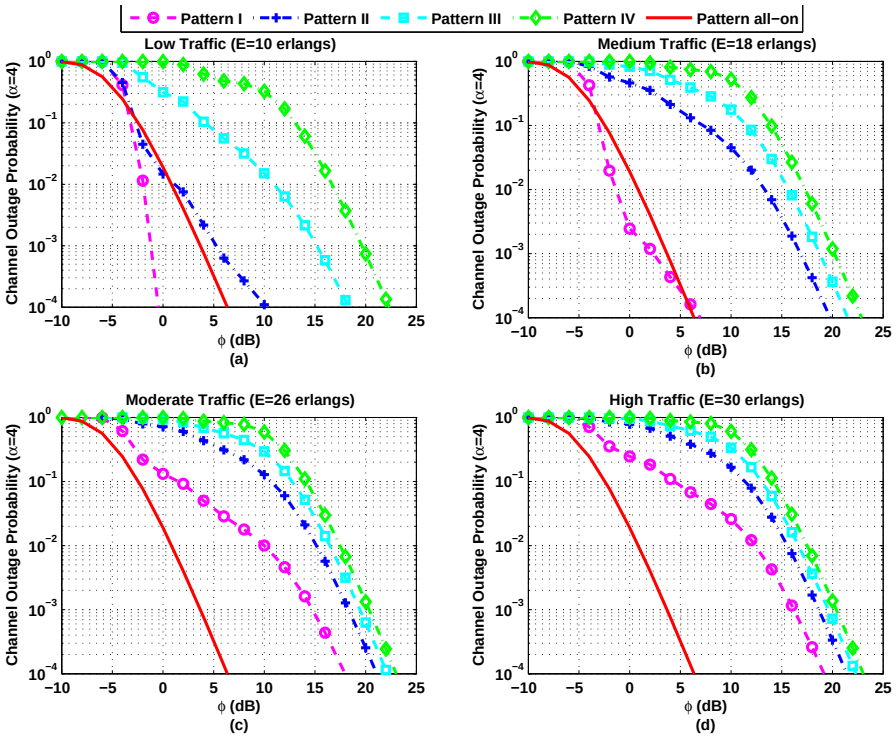

Figure 6.6: The worst-case channel outage probabilities of the established link

ulation. The quantity ϕ represents a given SNR level normalized by the network- and deployment-dependent system parameters. Thus, the ratio of two ϕ values (difference in dB) is indicative of how much extra transmit power is needed to be able to move from one SNR level to the other.

Fig. 6.6 presents the channel outage probabilities of all the patterns with low and high traffic loads. In Fig. 6.6, the solid curve represents the performance of the conventional all-on pattern (or equivalently, the channel outage probability of the UE in the sun cell), which serves as a benchmark of the additional energy-efficient patterns proposed in this chapter. From Fig. 6.6, when $E = 10$ Erlangs, to achieve a channel outage probability of 10^{-3}, Pattern I demands 4.81 dB less transmit power than the conventional pattern, resulting in $\rho(I, E = 10) = 0.3305$, thanks to the cooperation of BSs; but for the same QoS requirement, the other three switch-off patterns require more transmit power than the conventional pattern due to the increased BS-UE distances and fewer remaining active BSs, leading to $\rho(II, E = 10) = 1.1416$, $\rho(III, E = 10) = 14.23$, and $\rho(IV, E = 10) = 39.43$. As the traffic load increases, targeting at the channel outage probability of 10^{-3}, the ratios of the required transmit powers increase as shown in Table 6.5. This is because when the traffic load is higher, the remaining active BSs will be more frequently occupied, further reducing diversity order of the BS cooperation.

Table 6.5: The ratios (ρ) of the required transmit powers

	I	II	III	IV
E=10 Erlangs	$\rho = 0.3305$	$\rho = 1.142$	$\rho = 14.23$	$\rho = 39.43$
E=18 Erlangs	$\rho = 0.7300$	$\rho = 21.51$	$\rho = 33.63$	$\rho = 44.83$
E=26 Erlangs	$\rho = 13.14$	$\rho = 29.42$	$\rho = 38.51$	$\rho = 47.38$
E=30 Erlangs	$\rho = 17.91$	$\rho = 31.53$	$\rho = 39.20$	$\rho = 48.04$

6.5.3 Energy-Saving Performance

The energy saving ability under different levels of offered loads, as defined in (6.32) and (6.33), is evaluated in this part. Fig. 6.7 shows the *energy consumption per BS* for different patterns and the corresponding energy-efficient pattern-switching strategy, with $\eta = 10\%$, the target call-blocking probability requirement of 2%, and path loss exponent $\alpha = 4$. In Fig. 6.7, the four vertical dashed lines indicate how much traffic load each pattern can hold with the 2% call-blocking probability requirement; the solid curves represent the energy consumption of different patterns (as marked in the figure).

From Fig. 6.7, one can see that no single pattern can achieve the best energy-saving performance all the time with the minimum requirement of QoS guaranteed. Therefore, a switching strategy among these patterns that jointly considers both the resulting energy consumption and the QoS requirement is desirable and characterized by the dotted curves in Fig. 6.7. As shown in Fig. 6.7, the most energy-efficient

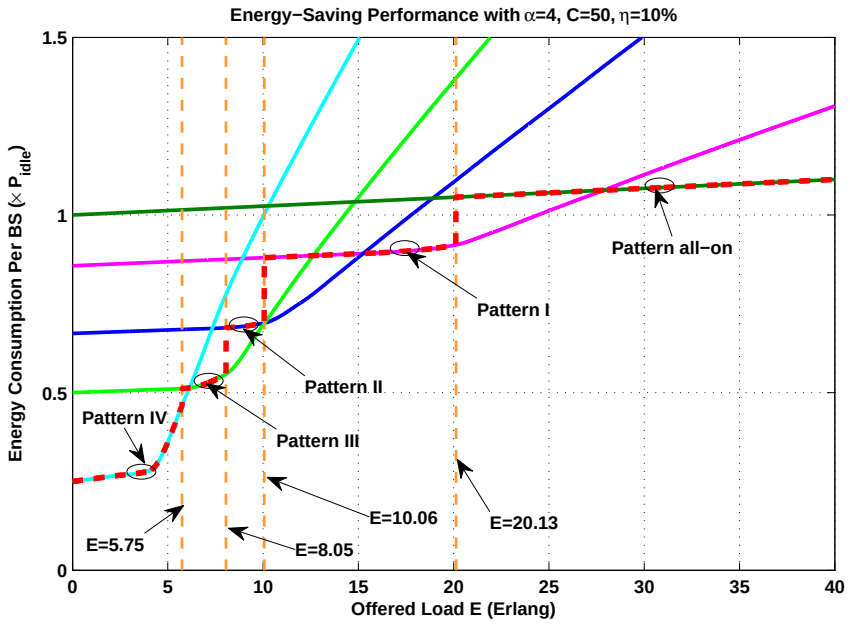

Figure 6.7: The energy consumption per BS with $\alpha = 4, C = 50, \eta = 10\%$.

pattern is chosen according to the offered load. As the offered load varies, the pattern switching occurs whenever a more energy-efficient pattern becomes feasible (6.35) or the currently chosen pattern would otherwise violate the constraint of the call-blocking probability. As shown in Fig. 6.7, during the very low traffic period ($E < 5$), the proposed operation can save more than 50% of the energy consumed by the conventional scheme with guaranteed QoS; for about half of the period of a typical day[7], the proposed energy-efficient patterns can be applied to save energy that is currently being wasted under the conventional all-on pattern.

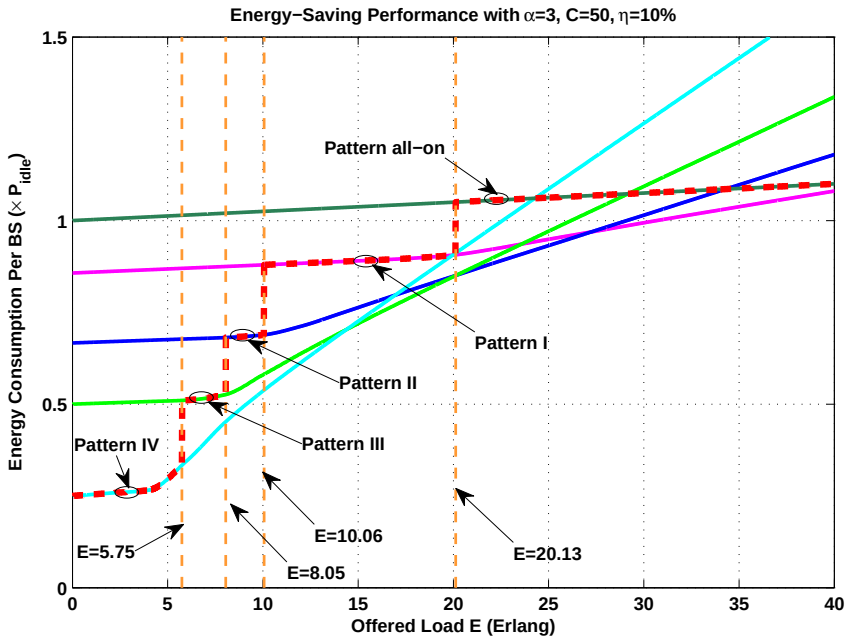

Figure 6.8: The energy consumption per BS with $\alpha = 3, C = 50, \eta = 10\%$.

6.5.3.1 Impact of the path loss exponent

Fig. 6.8 shows the energy consumption results with a lower path loss exponent $\alpha = 3$, keeping the other parameters the same with Fig. 6.7 (i.e. $C = 50$ and $\eta = 10\%$). Comparing Fig. 6.7 and Fig. 6.8, one can see that the energy consumption with lower path loss grows much slower with the increasing offered load than the one with high path loss. This is due to the fact that with a smaller path loss, the total transmit power required to extend coverage to the moon cells is reduced, resulting a smaller ρ in (6.33).

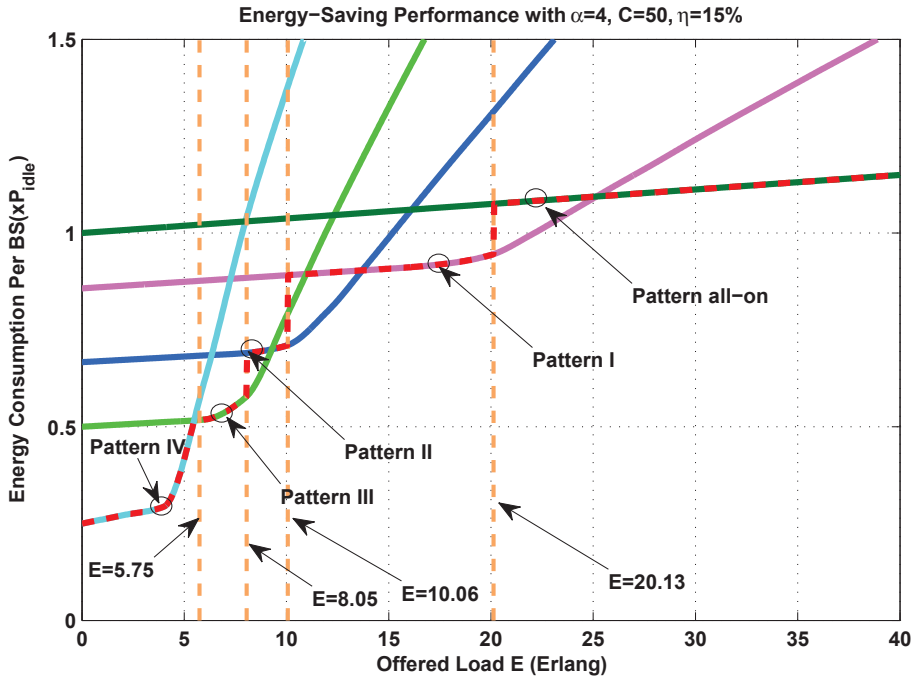

Figure 6.9: The energy consumption per BS with $\alpha = 4, C = 50, \eta = 15\%$.

6.5.3.2 Impact of η

Fig. 6.9 shows the energy consumption results with a larger $\eta = 15\%$ (with all the other parameters the same as used in Fig. 6.7). Comparing Fig. 6.9 with Fig. 6.7, one can see that as η increases, the more aggressive patterns[8] lose their advantages in energy saving to the more conservative patterns at smaller offer load. This is because a larger η gives a larger weighting factor to the transmit power consumption, in which case the benefit of having more cooperating BSs available in the more conservative patterns can be observed earlier at smaller offer load.

[7] according to the near-sinusoid daily traffic profile reported in [6]

[8] Pattern IV is considered as the most aggressive pattern, while the Pattern all-on is considered as the most conservative pattern, in terms of the number of switched-off cell.

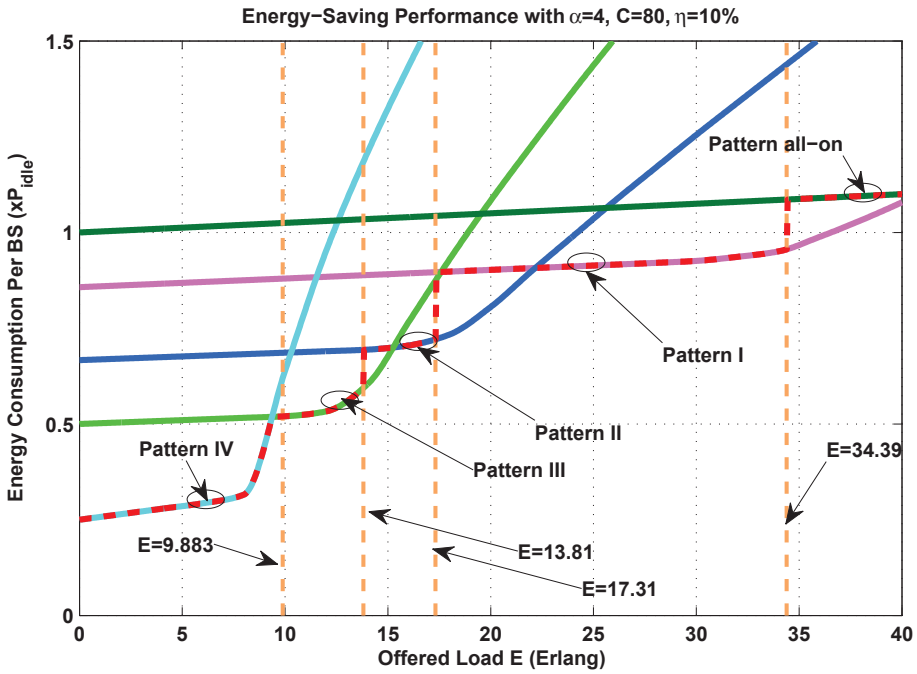

Figure 6.10: The energy consumption per BS with $\alpha = 4, C = 80, \eta = 10\%$.)

6.5.3.3 Impact of C

Unlike the parameters α and η which are determined by the characteristics of a given system, the service capacity C is a design parameter that can be expanded by upgrading hardware and software at the BS [84]. Therefore, it is worthwhile to study its impact to the energy saving performance. The impact of C is two-fold:

First, the service capacity C affects the call blocking probability. A larger service capacity of BS helps reduce the call blocking probability for a given offered load under any pattern, which loosens the constraint on pattern selection. For example, with a given call-blocking probability QoS threshold 2%, compared with the constraint with $C = 50$ as shown by (34), a larger $C = 80$ gives the following

loosened constraint:

$$S = \begin{cases} \{All-on,\ I,\ II,\ III,\ IV\}, & if\ E \in [0, 9.883); \\ \{All-on,\ I,\ II,\ III\}, & if\ E \in [9.883, 13.81); \\ \{All-on,\ I,\ II\}, & if\ E \in [13.81, 17.31); \\ \{All-on,\ I\}, & if\ E \in [17.31, 34.39); \\ \{All-on\}, & if\ E \in [34.39, 68.70]. \end{cases} \tag{6.35}$$

Second, the service capacity C affects the relative frequencies of the cooperating modes. A larger service capacity of BS reduces the likelihood that an active BS is fully occupied, so that more active BSs can still participate the BS cooperation at higher offer loads, which helps reduce the required transmit power (due to cooperative beamforming).

In Fig. 6.10, we presented the energy consumption results with a larger service capacity $C = 80$ (with all the other parameters the same as used in Fig. 6.7). Comparing Fig. 6.10 with Fig. 6.7, the larger service capacity C allows the more aggressive patterns to operate at higher offered load. For example, with $C = 50$ in Fig. 6.7, Pattern IV has to switch to Pattern III at $E = 5.75$ Erlangs to guarantee the call-blocking probability not exceeding the 2% threshold, even though at $E = 5.75$ Erlangs Pattern IV still demands less energy than Pattern III. However, with $C = 80$ in Fig. 6.10, the switch between Pattern IV and Pattern III occurs at $E = 9.37$ Erlangs, which is facilitated by the fact that with $C = 80$ Pattern IV is allowed to operate up to $E = 9.883$ Erlangs without violating the 2% QoS threshold of the call-blocking probability.

6.6 Summary

In this chapter, we propose an energy-efficient BS switching strategy in which some BSs are turned off and BS cooperation is used to effectively extend coverage with guaranteed QoS. Based on the standard hexagonal cell network model, four switch-off patterns are introduced to progressively turn more BSs off to save energy according to the offered traffic load. We consider QoS from both the network-layer and the physical-layer perspectives, and analyze the call-blocking probability and the channel outage probability. We guarantee the QoS of the UEs under the energy-efficient patterns by focusing on the worst-case transmission/reception locations instead of just looking at the spatially averaged performance. With guaranteed QoS, the energy-saving performance of the proposed scheme is evaluated. Both the analytical and numerical results exhibit significant energy-saving potential of the proposed idea of BS switching and cooperative coverage extension.

Several implications based on this work can be useful to practical cellular networks. First, switching off some BSs during low-traffic hours according to several predetermined patterns is effective in energy-saving with feasible complexity. Although the regular hexagonal cells hardly exist in reality, the well-planned macrocell BS deployment and the consistent periodicity of traffic profiles [5,6] afford the off-line computation of several progressive switching patterns for a certain area. Second, BS cooperation can be used to effectively extend coverage, especially when some BSs are off. Cooperation among BSs has been made available in recent standards such as LTE-advanced, referred to as Coordinated Multi-Point (CoMP), facilitat-

ing a basis for the proposed cooperative coverage extension scheme. Lastly, given the significant energy-saving potential predicted by the theoretical model, it can be worthwhile to investigate the potential signaling cost of pattern switching, UE handover, and BS Cooperation, which will be interesting future research.

Chapter 7: Conclusion and Future Work

7.1 Conclusion

In this dissertation research, towards the evolution of the green wireless communications, we contribute to two main aspects of the wireless communications system: air-interface and networking. After an overview of the principles of time reversal and the recent research on energy-efficient network operations as a background for this dissertation, we have addressed the following problems.

First, we proposed the concept of TRDMA as a novel wireless media access scheme for broadband wireless communications. In the context of the a multi-user downlink system, we investigated its fundamental theoretical limits in terms of the effective SINR, achievable sum rate, and the achievable rate with $\epsilon-$outage. Based on a simplified two-user case, the achievable region was presented to demonstrate the advantages of the proposed TRDMA scheme over its counterpart techniques. We also incorporated and examined quantitatively the impact of spatial correlation of users to system performance to gain a more comprehensive understanding of TRDMA.

Second, a TRDMA based uplink scheme was introduced to complement a unique asymmetric architecture of the TRDMA based multi-user network. In the

proposed asymmetric architecture, most of the complexity and processing tasks are shifted to the base station for both uplink and downlink, resulting in a minimal-cost terminal devices in the network. Additionally, a comparative study between the TRDMA system and the massive MIMO system was conducted, showing that in essence the TRDMA system treats each path in the environment as a virtual antenna, and is equivalent to a virtual massive MIMO system under certain conditions.

Third, a 2D parallel interference cancellation technique was developed to further enhance the system performance of the TRDMA uplink. The proposed 2D parallel interference cancellation scheme can utilize the tentative decisions of the detected symbols to effectively cancel both the inter-symbol interference and the inter-user interference. An advanced multi-stage processing was also introduced by cascading multiple stages of the cancellation, whose total delay increases linearly with the number of stages, but independently with the number of users. The BER performance of the single-stage scheme was analyzed, and the theoretical approximation derived in the analysis is well consistent with simulation results. Simulations for up-to 3 stages of the proposed 2D parallel interference cancellation were presented and compared with the basic TRDMA system without interference cancellation.

Lastly, the energy-saving potential of the cooperative networking was explored in the context of cellular systems. We proposed a dynamic base-station switching strategy and incorporated the cooperative base-station operation to improve the energy-efficiency of the cellular networks. Specifically, four progressive switch-off patterns were proposed and dynamically switched according to the traffic load to maximize the energy saving without sacrificing the quality of service of users. T-

wo quality of service metrics, the call-blocking probability and the channel outage probability, were considered and guaranteed by identifying the user situated at the worst-case locations. The cooperation of the base stations was used to efficiently extend the network coverage to the areas with a switched-off base station. A significant energy-saving potential was observed for the proposed networking operation, compared with the conventional network operation.

7.2 Future Work

In this dissertation, we have shown that the TRDMA system can have some unique advantages to serve as a promising candidate for the air interface of the green wireless communications. Another interesting feature of the time reversal structure that has not been discussed in this dissertation is its physical layer security.

Secret communications have been of critical interest for quite a long time. Because of the fast technology evolution, a malicious attacker may easily find some low-cost radio equipments or easily modify the existing equipments to enable a potential intrusion. Moreover, wireless networks are extremely vulnerable to malicious attacks due to the broadcasting nature of wireless transmission and often a distributed network structure. As a result, traditional security measures may become insufficient to protect wireless networks. As the future work, we believe that the TR-based communications can be further exploited to enhance system security based on the unique energy-focusing effect.

In a rich scattering wireless environment, multiple paths are formed by numer-

ous surrounding reflectors. For receivers at different locations, the received waveforms undergo different reflecting paths and delays, and hence the multi-path profile can be viewed as a unique location-specific signature. As this information is only available to the transmitter and the intended receiver, it is very difficult for other unauthorized users to infer or forge such a signature. It has been shown in that even when the eavesdroppers are close to the target receiver, the received signal strength is much lower at the eavesdroppers than at the target receiver in an indoor application, because the received signals are added incoherently at the eavesdroppers.

Our future research plan is two-fold: first, we would like to understand the secrecy capacity of the time-reversal communications; second, we will be interested in developing a time-reversal based secure communications protocol to leverage the location-specific multi-path signatures to protect the secret information from malicious users.

Bibliography

[1] G. Fettweis and E. Zimmermann. Ict energy consumption-trends and challenges. In *Proc. of the 11th International Symposium on Wireless Personal Multimedia Communications (WPMC 2008)*, 2008.

[2] B. Wang, Y. Wu, F. Han, Y.-H. Yang, and K. J. R. Liu. Green wireless communications: A time-reversal paradigm. *IEEE Journal of Selected Areas in Communications, special issue on Energy-Efficient Wireless Communications*, 29(8):1698–1710, Sep 2011.

[3] S. M. Emami, J. Hansen, Student Member, A. D. Kim, G. Papanicolaou, A. J. Paulraj, D. Cheung, and C. Prettie. Predicted time reversal performance in wireless communications using channel measurements. *IEEE Communications Letters*, 2004.

[4] M.A. Marsan, L. Chiaraviglio, D. Ciullo, and M. Meo. Optimal energy savings in cellular access networks. In *IEEE International Conference on Communications Workshops*, pages 1–5, 2009.

[5] Eunsung Oh, B. Krishnamachari, Xin Liu, and Zhisheng Niu. Toward dynamic energy-efficient operation of cellular network infrastructure. *IEEE Communications Magazine*, 49(6):56–61, 2011.

[6] Eunsung Oh and B. Krishnamachari. Energy savings through dynamic base station switching in cellular wireless access networks. In *IEEE Global Telecommunications Conference (GLOBECOM 2010)*, pages 1–5, 2010.

[7] L. Chiaraviglio, D. Ciullo, M. Meo, and M.A. Marsan. Energy-aware umts access networks. In *Proc. of the 11th International Symposium on Wireless Personal Multimedia Communications (WPMC 2008)*, 2008.

[8] Sheng Zhou, Jie Gong, Zexi Yang, Zhisheng Niu, and Peng Yang. Green mobile access network with dynamic base station energy saving. In *ACM International Conference on Mobile Computing and Networking (MobiCom)*, 2009.

[9] A. J. Fehske, F. Richter, and G. P. Fettweis. Energy efficiency improvements through micro sites in cellular mobile radio networks. In *IEEE GLOBECOM Workshops*, pages 1–5, 2009.

[10] Kyuho Son, Eunsung Oh, and B. Krishnamachari. Energy-aware hierarchical cell configuration: From deployment to operation. In *IEEE Conference on Computer Communications Workshops (INFOCOM WKSHPS 2011)*, pages 289–294, 2011.

[11] Marco Ajmone Marsan and Michela Meo. Energy efficient management of two cellular access networks. *ACM SIGMETRICS Perform. Eval. Rev.*, 37(4):69–73, March 2010.

[12] Dongxu Cao, Sheng Zhou, Chao Zhang, and Zhisheng Niu. Energy saving performance comparison of coordinated multi-point transmission and wireless relaying. In *IEEE Global Telecommunications Conference (GLOBECOM 2010)*, pages 1–5, 2010.

[13] B. Ya. Zeldovich, N. F. Pilipetsky, and V. V. Shkunov. *Principles of Phase Conjugation*. Berlin: Springer-Verlag, 1985.

[14] A. P. Brysev, L. M. Krutyanskii, and V. L. Preobrazhenskii. Wave phase conjugation of ultrasonic beams. *Physics-Uspekhi*, 41(8):793–805, 1998.

[15] M. Fink, C. Prada, F. Wu, and D. Cassereau. Self focusing in inhomogeneous media with time reversal acoustic mirrors. In *Proceedings of IEEE Ultrasonics Symposium*, volume 2, pages 681–686, 1989.

[16] C. Prada, F. Wu, and M. Fink. The iterative time reversal mirror: A solution to self-focusing in the pulse echo mode. *The Journal of the Acoustical Society of America*, 90(2):1119–1129, 1991.

[17] M. Fink. Time reversal of ultrasonic fields. i. basic principles. *IEEE Transactions on Ultrasonics, Ferroelectrics and Frequency Control*, 39(5):555–566, 1992.

[18] Christian Dorme and Mathias Fink. Focusing in transmit–receive mode through inhomogeneous media: The time reversal matched filter approach. *The Journal of the Acoustical Society of America*, 98(2):1155–1162, 1995.

[19] Arnaud Derode, Philippe Roux, and Mathias Fink. Robust acoustic time reversal with high-order multiple scattering. *Phys. Rev. Lett.*, 75:4206–4209, Dec 1995.

[20] W. A. Kuperman, William S. Hodgkiss, Hee Chun Song, T. Akal, C. Ferla, and Darrell R. Jackson. Phase conjugation in the ocean: Experimental demonstration of an acoustic time-reversal mirror. *The Journal of the Acoustical Society of America*, 103(1):25–40, 1998.

[21] H. C. Song, W. A. Kuperman, W. S. Hodgkiss, T. Akal, and C. Ferla. Iterative time reversal in the ocean. *The Journal of the Acoustical Society of America*, 105(6):3176–3184, 1999.

[22] D. Rouseff, D.R. Jackson, W. L J Fox, C.D. Jones, J.A. Ritcey, and D.R. Dowling. Underwater acoustic communication by passive-phase conjugation: theory and experimental results. *IEEE Journal of Oceanic Engineering*, 26(4):821–831, 2001.

[23] A. Derode, A. Tourin, J.de Rosny, M. Tanter, S. Yon, and M. Fink. Taking advantage of multiple scattering to communicate with time-reversal antennas. *Phys. Rev. Lett.*, 90:014301, Jan 2003.

[24] D. Rouseff, D.R. Jackson, W. L J Fox, C.D. Jones, J.A. Ritcey, and D.R. Dowling. Underwater acoustic communication by passive-phase conjugation: theory and experimental results. *IEEE Journal of Oceanic Engineering*, 26(4):821–831, 2001.

[25] G.F. Edelmann, T. Akal, W.S. Hodgkiss, Seongil Kim, W.A. Kuperman, and Hee Chun Song. An initial demonstration of underwater acoustic communication using time reversal. *IEEE Journal of Oceanic Engineering*, 27(3):602–609, 2002.

[26] M. Emami, Mai Vu, J. Hansen, A. J. Paulraj, and G. Papanicolaou. Matched filtering with rate back-off for low complexity communications in very large delay spread channels. In *Conference Record of the Thirty-Eighth Asilomar Conference on Signals, Systems and Computers*, volume 1, pages 218–222, 2004.

[27] K. F. Sander and G. A. L. Reed. *Transmission and propagation of electromagnetic waves*. New York: Cambridge University Press, second edition, 1986.

[28] Benjamin E. Henty and Daniel D. Stancil. Multipath-enabled super-resolution for rf and microwave communication using phase-conjugate arrays. *Phys. Rev. Lett.*, 93:243904, Dec 2004.

[29] G. Lerosey, J. de Rosny, A. Tourin, A. Derode, G. Montaldo, and M. Fink. Time reversal of electromagnetic waves. *Phys. Rev. Lett.*, 92:193904, May 2004.

[30] J. M F Moura and Yuanwei Jin. Time reversal imaging by adaptive interference canceling. *IEEE Transactions on Signal Processing*, 56(1):233–247, 2008.

[31] J. M. F. Moura and Yuanwei Jin. Detection by time reversal: Single antenna. *IEEE Transactions on Signal Processing*, 55(1):187–201, 2007.

[32] Yuanwei Jin and J. M F Moura. Time-reversal detection using antenna arrays. *IEEE Transactions on Signal Processing*, 57(4):1396–1414, 2009.

[33] Simon Fletcher. Core 5 - Green radio: programme objectives and overview. `http://www.mobilevce.com/dloads-publ/mtg284Item_1503.ppt/`, 2008.

[34] K. J. R. Liu, A. K. Sadek, W. Su, and A. Kwasinski. *Cooperative Communications and Networking*. Cambridge University Press, 2009.

[35] A. K. Sadek, Zhu Han, and K. J. R. Liu. Distributed relay-assignment protocols for coverage expansion in cooperative wireless networks. *IEEE Transactions on Mobile Computing*, 9(4):505–515, 2010.

[36] Jeongho Kwak, Kyuho Son, Yung Yi, and Song Chong. Greening effect of spatio-temporal power sharing policies in cellular networks with energy constraints. *IEEE Transactions on Wireless Communications*, 11(12):4405–4415, 2012.

[37] Theodore Rappaport. *Wireless Communications: Principles and Practice*. Prentice Hall PTR, New Jersey, USA, 2nd edition, 2001.

[38] J. S. Seybold. *Introduction to RF propagation*. Wiley-Interscience, 2005.

[39] Z. Han and K. J. R. Liu. *Resource Allocation for Wireless Networks*. Cambridge University Press, 2008.

[40] Hieu Nguyen, Zhao Zhao, Feng Zheng, and T. Kaiser. Preequalizer design for spatial multiplexing simo-uwb tr systems. *Vehicular Technology, IEEE Transactions on*, 59(8):3798–3805, 2010.

[41] Trung Kien Nguyen, Hieu Nguyen, Feng Zheng, and T. Kaiser. Spatial correlation in sm-mimo-uwb systems using a pre-equalizer and pre-rake filter. In *Ultra-Wideband (ICUWB), 2010 IEEE International Conference on*, volume 2, pages 1–4, 2010.

[42] Hung Tuan Nguyen, I.Z. Kovacs, and P. C F Eggers. A time reversal transmission approach for multiuser uwb communications. *IEEE Transactions on Antennas and Propagation*, 54(11):3216–3224, 2006.

[43] I.H. Naqvi, A. Khaleghi, and G. Elzein. Performance enhancement of multiuser time reversal uwb communication system. In *Wireless Communication Systems, 2007. ISWCS 2007. 4th International Symposium on*, pages 567–571, 2007.

[44] Hung Tuan Nguyen. Partial one bit time reversal for uwb impulse radio multiuser communications. In *Communications and Electronics, 2008. ICCE 2008. Second International Conference on*, pages 246–251, 2008.

[45] Trung Kien Nguyen, Hieu Nguyen, Feng Zheng, and T. Kaiser. Spatial correlation in the broadcast mu-mimo uwb system using a pre-equalizer and time reversal pre-filter. In *Signal Processing and Communication Systems (ICSPCS), 2010 4th International Conference on*, pages 1–6, 2010.

[46] A. J. Goldsmith. *Wireless Communications*. New York: Cambridge University Press, 2005.

[47] A. Derode, A. Tourin, and M. Fink. Ultrasonic pulse compression with one-bit time reversal through multiple scattering. *Journal of Applied Physics*, 85(9):6343–6352, 1999.

[48] Paul H. Moose. A technique for orthogonal frequency division multiplexing frequency offset correction. *IEEE Transactions on Communications*, 42(10):2908–2914, 1994.

[49] Jungwon Lee, Hui-Ling Lou, D. Toumpakaris, and J.M. Cioffi. Snr analysis of ofdm systems in the presence of carrier frequency offset for fading channels. *Wireless Communications, IEEE Transactions on*, 5(12):3360–3364, 2006.

[50] A. Papoulis and U. Pillai. *Probability, Random Variables and Stochastic Processes*. New York: McGraw-Hill, 4^{th} edition, 2002.

[51] D. Tse and P. Viswanath. *Fundamental of Wireless Communication*. New York: Cambridge University Press, 2005.

[52] T. M. Cover and J. A. Thomas. *Elements of Information Theory*. John Wiley & Sons, second edition, 2006.

[53] JamesL. Massey. Towards an information theory of spread-spectrum systems. In SavoG. Glisic and PenttiA. Leppanen, editors, *Code Division Multiple Access Communications*, pages 29–46. Springer US, 1995.

[54] T. Cover. Broadcast channels. *IEEE Transactions on Information Theory*, 18(1):2–14, 1972.

[55] P. Bergmans. Random coding theorem for broadcast channels with degraded components. *IEEE Transactions on Information Theory*, 19(2):197–207, 1973.

[56] P. Bergmans. A simple converse for broadcast channels with additive white gaussian noise (corresp.). *IEEE Transactions on Information Theory*, 20(2):279–280, 1974.

[57] P. Bergmans and T.M. Cover. Cooperative broadcasting. *IEEE Transactions on Information Theory*, 20(3):317–324, 1974.

[58] R.B. Ertel and J.H. Reed. Generation of two equal power correlated rayleigh fading envelopes. *IEEE Communications Letters*, 2(10):276–278, 1998.

[59] B. Natarajan, C.R. Nassar, and V. Chandrasekhar. Generation of correlated rayleigh fading envelopes for spread spectrum applications. *Communications Letters, IEEE*, 4(1):9–11, 2000.

[60] Feng Han, Yu-Han Yang, Beibei Wang, Yongle Wu, and K. J. R. Liu. Time-reversal division multiple access over multi-path channels. *IEEE Transactions on Communications*, 60(7):1953–1965, 2012.

[61] Erik G. Larsson, Fredrik Tufvesson, Ove Edfors, and Thomas L. Marzetta. Massive mimo for next generation wireless systems. *arXiv: 1304.6690 [cs.IT]*, 2013.

[62] F. Rusek, D. Persson, Buon Kiong Lau, E. G. Larsson, T. L. Marzetta, O. Edfors, and F. Tufvesson. Scaling up mimo: Opportunities and challenges with very large arrays. *IEEE Signal Processing Magazine*, 30(1):40–60, 2013.

[63] T. L. Marzetta. Noncooperative cellular wireless with unlimited numbers of base station antennas. *IEEE Transactions on Wireless Communications*, 9(11):3590–3600, 2010.

[64] Hien Quoc Ngo, Erik G. Larsson, and Thomas L. Marzetta. Energy and spectral efficiency of very large multiuser mimo systems. *IEEE Transactions on Communications*, 61(4):1436–1449, 2013.

[65] J. Hoydis, S. ten Brink, and M. Debbah. Massive mimo in the ul/dl of cellular networks: How many antennas do we need? *IEEE Journal on Selected Areas in Communications*, 31(2):160–171, 2013.

[66] Hong Yang and T.L. Marzetta. Performance of conjugate and zero-forcing beamforming in large-scale antenna systems. *IEEE Journal on Selected Areas in Communications*, 31(2):172–179, 2013.

[67] A. Ozgur, O. Leveque, and D. Tse. Spatial degrees of freedom of large distributed mimo systems and wireless ad hoc networks. *IEEE Journal on Selected Areas in Communications*, 31(2):202–214, 2013.

[68] R. Aggarwal, C.E. Koksal, and P. Schniter. On the design of large scale wireless systems. *IEEE Journal on Selected Areas in Communications*, 31(2):215–225, 2013.

[69] I.H. Naqvi, P. Besnier, and G. El-Zein. Effects of time variant channel on a time reversal uwb system. In *Global Telecommunications Conference, 2009. GLOBECOM 2009. IEEE*, pages 1–6, 2009.

[70] Yu-Han Yang, Beibei Wang, W. S. Lin, and K. J. R. Liu. Near-optimal waveform design for sum rate optimization in time-reversal multiuser downlink systems. *IEEE Transactions on Wireless Communications*, 12(1):346–357, 2013.

[71] S. Verdú. Minimum probability of error for asynchronous gaussian multiple-access channels. *IEEE Transactions on Information Theory*, 32(1):85–96, 1986.

[72] S. Verdú. Optimum multiuser asymptotic efficiency. *IEEE Transactions on Communications*, 34(9):890–897, 1986.

[73] M. K. Varanasi and B. Aazhang. Multistage detection in asynchronous code-division multiple-access communications. *IEEE Transactions on Communications*, 38(4):509–519, 1990.

[74] A. J. Viterbi. Very low rate convolution codes for maximum theoretical performance of spread-spectrum multiple-access channels. *IEEE Journal on Selected Areas in Communications*, 8(4):641–649, 1990.

[75] D. Divsalar and Marvin K. Simon. Improved cdma performance using parallel interference cancellation. In *IEEE Military Communications Conference (MILCOM'94)*, volume 3, pages 911–917, 1994.

[76] A. Duel-Hallen, J. Holtzman, and Z. Zvonar. Multiuser detection for cdma systems. *IEEE Personal Communications*, 2(2):46–58, 1995.

[77] S. Moshavi. Multi-user detection for ds-cdma communications. *IEEE Communications Magazine*, 34(10):124–136, 1996.

[78] D. Divsalar, Marvin K. Simon, and Dan Raphaeli. Improved parallel interference cancellation for cdma. *IEEE Transactions on Communications*, 46(2):258–268, 1998.

[79] A. W. van der Vaart. *Asymptotic Statistics*. New York: Cambridge University Press, 2000.

[80] C. Rose and M. D. Smith. The multivariate normal distribution. *The Mathematica Journal*, 6(1):32–37, 1996.

[81] Andreas F. Molisch, Kannan Balakrishnan, Chia chin Chong, Shahriar Emami, Andrew Fort, Johan Karedal, Juergen Kunisch, Hans Schantz, Ulrich Schuster, and Kai Siwiak. Ieee 802.15.4a channel model - final report. In *Tech. Rep. Document IEEE 802.15-04-0662-02-004a*, 2005.

[82] T. Rappaport. *Wireless Communications: Principles and Practice*. Prentice Hall, 1996.

[83] G. Stuber. *Principles of Mobile Communication*. Kluwer Academic Publishers, 2nd edition, 2001.

[84] J. Lerzer Z. Zhang, F. Heiser and H. Leuschner. Advanced baseband technology in third-generation radio base stations. *Ericsson Review*, (1):32–41, 2003.

[85] A. J. Goldsmith. *Wireless Communications*. Cambridge University, New York, USA, 1st edition, 2005.

[86] M. Bublin, I. Kambourov, P. Slanina, D. Bosanska, O. Hlinka, O. Hrdlicka, and P. Svac. Inter-cell interference management by dynamic channel allocation, scheduling and smart antennas. In *Mobile and Wireless Communications Summit, 2007. 16th IST*, pages 1–5, 2007.

[87] H. Ochiai, P. Mitran, H.V. Poor, and Vahid Tarokh. Collaborative beamforming for distributed wireless ad hoc sensor networks. *IEEE Transactions on Signal Processing*, 53(11):4110–4124, 2005.

[88] D. G. Brennan. On the maximum signal-to-noise ratio realizable from several noisy signals. In *Proc. Institute of Radio Engineers*, page 1530, Oct 1955.

[89] R. M. Karp. Reducibility Among Combinatorial Problems. In *Complexity of Computer Computations*, pages 85–103. Plenum Press, 1972.

[90] Michael R. Garey and David S. Johnson. *Computers and Intractability; A Guide to the Theory of NP-Completeness*. W. H. Freeman & Co., New York, USA, 1990.

[91] D. Gross, J. F. Shortle, J. M. Thompson, and C. M. Harris. *Fundamentals of Queueing Theory*. John Wiley & Sons, New Jersey, USA, 4th edition, 2008.

[92] S. Boyd and L. Vandenberghe. *Convex Optimiaztion*. Cambridge University, New York, USA, 2004.

[93] F. E. Satterthwaite. Synthesis of variance. *Psychometrika*, 6(5):309–316, 1941.

[94] C. Alexopoulos. Statistical analysis of simulation output: State of the art. In *Simulation Conference, 2007 Winter*, pages 150–161, 2007.

[95] Raymond H Y Louie, M. R. McKay, and I. B. Collings. New performance results for multiuser optimum combining in the presence of rician fading. *IEEE Transactions on Communications*, 57(8):2348–2358, 2009.

[96] O. Arnold, F. Richter, G. Fettweis, and O. Blume. Power consumption modeling of different base station types in heterogeneous cellular networks. In *Future Network and Mobile Summit, 2010*, pages 1–8, 2010.

[97] Oliver Blume, Harald Eckhardt, Siegfried Klein, Edgar Kuehn, and Wieslawa M. Wajda. Energy savings in mobile networks based on adaptation to traffic statistics. *Bell Lab. Tech. J.*, 15(2):77–94, September 2010.